MODELING OF INTERFACIAL INSTABILITY, CONDUCTIVITY AND PARTICLE MIGRATION IN CONFINED FLOWS

by

Daihui Lu

A Dissertation

Submitted to the Faculty of Purdue University

In Partial Fulfillment of the Requirements for the degree of

Doctor of Philosophy

School of Mechanical Engineering

West Lafayette, Indiana

December 2021

THE PURDUE UNIVERSITY GRADUATE SCHOOL
STATEMENT OF COMMITTEE APPROVAL

Dr. Ivan C. Christov, Chair

School of Mechanical Engineering

Dr. Arezoo M. Ardekani

School of Mechanical Engineering

Dr. Guang Lin

Department of Mathematics

Dr. Carl R. Wassgren

School of Mechanical Engineering

Approved by:

Dr. Nicole L. Key

To my grandma, Rongxiang Zhu

ACKNOWLEDGMENTS

I would like to express my deepest appreciation to my advisor, Dr. Ivan C. Christov, who made this thesis possible and made my Ph.D. journey very enjoyable. Before starting the Ph.D. program, I had heard of many sad stories on miserable Ph.D. life and prepared myself to quit if it happened. Now I am approaching the end of my Ph.D. journey, and I feel very fortunate that none of the miseries happened to me. On the contrary, Dr. Christov always supports and truly cares about his students. I am very grateful for all the opportunities he has provided to me. He helps me grow, both as a researcher and as an individual, through his example, which will certainly have a long-term impact on the way I treat others and my career values.

To my thesis committee members, Dr. Arezoo M. Ardekani, Dr. Guang Lin and Dr. Carl R. Wassgren, thank you for always being supportive and approachable. I appreciate every advice you provided to me on this thesis.

I would also like to acknowledge the donors of the American Chemical Society Petroleum Research Fund for support of this thesis under ACS PRF award # 57371-DNI9 (PI: Ivan C. Christov).

To my colleagues at the TMNT lab: Dr. Federico Municchi, Dr. Kimberly A. Stevens Boster, Dr. Vishal Anand, Xiaojia Wang, Zongxin Yu, Mengying Wang, Tanmay C. Shidhore, Pranay P. Nagrani, Jielin Yang, thank you for your valuable discussions on research and/or life. The pleasure, help and encouragement you bring to the team have become one of my best memories at Purdue.

To my boyfriend, Dr. Chen Wei, thank you for your love, compliments and applause over the past four years. You are my best friend and a great teammate. You always make me laugh and cheer me up when I feel down, which has made the challenges in the Ph.D. journey much easier to get through.

Lastly, I would like to express my deepest love and gratitude to my family. To my grandma, the weekends I spent in your yard with chickens I fed, rabbits who bite me vines that grow super sour grapes, a walnut tree that ruined my favorite dress, and many many flowers that I can't name, made up a wonderful childhood for me. The summer nights with

breeze, stars in the sky and your fairy tales about Chang'e over the moon are still the best scenes in my dream. To my parents, thank you for loving and supporting me whatever I want to pursue. I would not have made it this far without your love, support and encouragement. I know I can always rely on you to have my back. To my brother, you are an angel to me. You bring me so much joy, love and happiness. For that, I am always grateful to this world.

TABLE OF CONTENTS

LIST OF TABLES

LIST OF FIGURES

ABSTRACT

This thesis analyzed three fundamental fluid dynamics problems arising from multiphase flows that may be encountered in hydraulically fractured flow passages. During hydraulic fracturing ("fracking"), complex fluids laden with proppants are pumped into tight rock formations. Flow passages in these formation are naturally heterogeneous with geometric variations, which become even more pronounced due to fracking. Upon increasing the flow area (and, thus, the conductivity of the rock), crude oil, shale gas or other hydrocarbons can then flow out of the formation more easily. In this context, we encounter the following three fluid mechanical phenomena: fluid–fluid interfacial instabilities, flow-wise variation of the hydraulic conductivity, and particle migration in the pumped fluids.

First, we studied the (in)stability of the interface between two immiscible liquids in angled (tapered) Hele-Shaw cells, as model of a non-uniform flow passage. We derived an expression for the growth rate of perturbations to the flat interface and for the critical capillary number, as functions of the small gap gradient (taper). On this basis, we formulated a three-regime theory to describe the interface's stability. Specifically, we found a new regime in which the growth rate changes from negative to positive (converging cells), or from positive to negative (diverging cells), thus the interface's stability can change type at some location in the cell. We conducted three-dimensional OpenFOAM® simulations of the Navier–Stokes equations, using the continuous surface force method, to validate the theory.

Next, we investigated the flow-wise variation of the hydraulic conductivity inside a non-uniformly shaped fracture with permeable walls. Using lubrication theory for viscous flow, in conjunction with the Beavers–Joseph–Saffman boundary condition at the permeable walls, we obtained an analytical expression for the velocity profile, conductivity, and wall permeation velocity. The new expression highlights the effects of geometric variation, the permeability of the walls, and the effect of flow inertia. The theory was validated against OpenFOAM® simulations of the Navier–Stokes equations subject to a tensorial slip boundary condition.

Finally, we extended the utility of phenomenological models for particle migration in shear flow using the physics-informed neural networks (PINNs) approach. We first verified

the approach for solving the inverse problem of radial particle migration in a non-Brownian suspension in an annular Couette flow. Then, we applied this approach to both non-Brownian and Brownian suspensions in Poiseuille slot flow, for which a definitive calibration of the phenomenological migration model has been lacking. Using PINNs, we identified the unknown/empirical parameters in the physical model, showing that (unlike assumptions made in the literature) they depend on the bulk volume fraction and shear Péclet number.

1. INTRODUCTION

1.1 Background

Crude oil and natural gas exist as fluids in large underground reservoirs in sedimentary basins around the world. They occupy the connected porous media within strata of sedimentary rocks, typically sandstones or carbonates [1]. Over the last decade, hydraulic fracturing ("fracking") of shales has paved the way towards increasing the recoverable reserves of oil and gas in the United States [2]. During fracking, complex fluids (primarily water-based suspensions with dispersed particulates termed "proppants") [3], [4] are pumped into tight formations [5], [6]. Figure 1.1 shows a 'candidate' rock formation for hydraulic fracturing; these formations are naturally heterogeneous with geometric variations in the flow passages that become even more significant during fracking. Upon increasing the 'conductivity' of the rock (i.e., by enlarging the flow passages through high-pressure facturing), crude oil, shale gas or other hydrocarbons can then flow out of the formation more easily.

Although the effectiveness of fracking was demonstrated in 1947 [8], it remains a challenging approach to energy production, in particular, due to the complex thermo-hydro-mechanical-chemical coupled processes involved across multiple space and time scales [9]. One such process is the stability of the interface between the fracking (displacing) fluid and the hydrocarbons (displaced fluid) [7]. In the fracturing process, the displacing fluid, primarily water with proppants [10], is injected into a well bore at high pressure to create cracks in the subsurface rock formation. A stable interface can produce a "clean" sweep of the fracture, whereas an unstable interface leaves oil or gas films and layers behind. Thus, there is an impetus to study fluid–fluid interface instabilities in complex geometries.

Fracking is inherently a multiscale problem [9]: as the injected high-pressure fluid enters a rock formation from the well bore, a complex array of cracks of various shapes, sizes, and with flow-wise variations, are created [3], [11]. This network of fractures increases the conductivity of the rock formation by increasing the available flow area [12], [13]. Similarly, in enhanced geothermal systems [14], heat is extracted from hot rocks by flooding the dry fracture network [15], [16]. Thus, it is of practical importance, as well as of fundamental

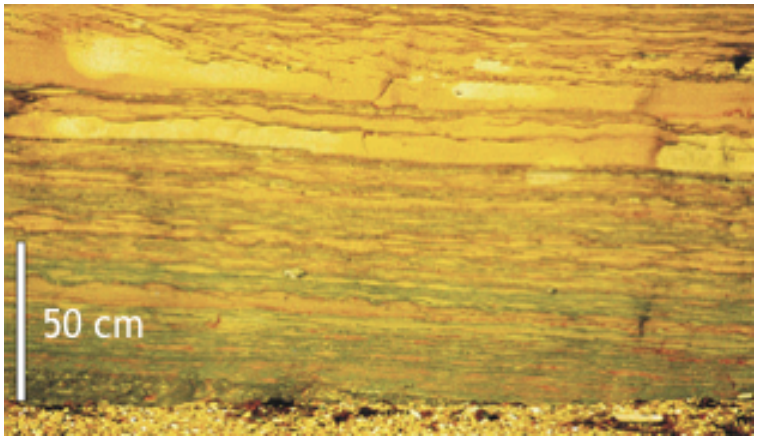

Figure 1.1. A "heterolithic facies" has permeability variations on the length scale of 1 cm vertically and on the length scale of 10 cm horizontally. Oil and gas are trapped in the nonuniform spaces between the layers. Reproduced from Muggeridge, Cockin, Webb, *et al.* [7] under CC BY 3.0.

scientific interest, to understand the conductivity variations in complex and non-uniform fractures.

Another complex subsurface flow process is particle migration in flows, a phenomenon common to many areas of the engineering sciences. From the collective motion of cells in the circulatory system [17] to the generation of stable emulsions for food and household products [18] to the deposition of proppants into hydraulic fractures [19], understanding how, why and when objects migrate and interact in flows is a fundamental fluid mechanics problem [20]. Although much has been accomplished since the pioneering work in the 19th and 20th centuries, there still remain aspects to particle migration in flows that are not fully understood, are unexpected [21] and are difficult to disentangle [22]. Fracking involves the use of not just clear fluids but also fluids bearing "proppants," which are particulate materials meant to settle into cracks to prop them open [19], [23], [24] (see the schematic in Fig. 1.2), prevent crack localization instabilities [25] and increase fracture conductivity. Even formulating this transport problem is difficult due to various hydrodynamics effects involved [26], nonuniformities in the proppant particle shapes [19], [23], [24] (see Fig. 1.2) and the flow conduits [11], the proppants' nontrivial surface chemistry [27] and the variable

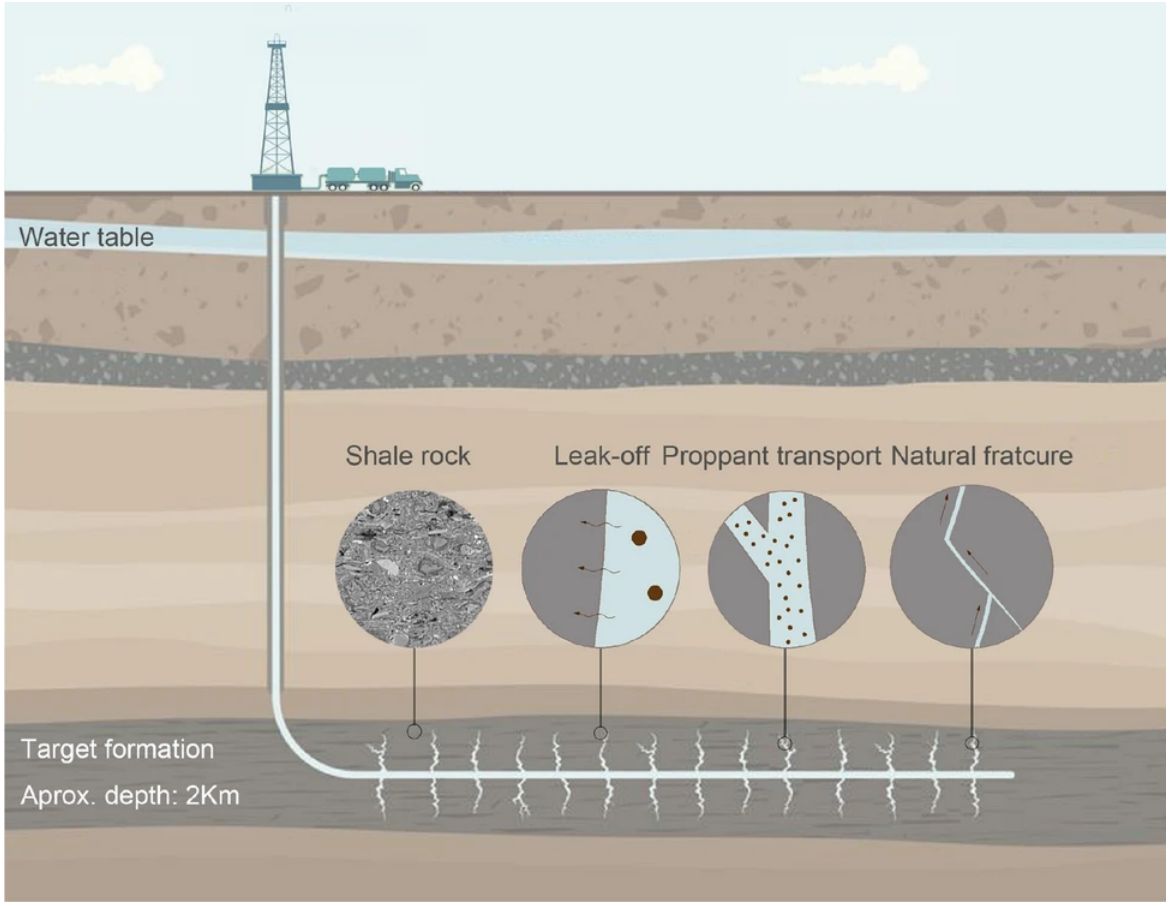

Figure 1.2. A typical schematic of the hydraulic fracturing process. Proppant-bearing fluid is pumped into a primary (large) crack, with many secondary (smaller) cracks branching from it. Proppants are used in hydraulic fracturing to attempt to keep fractures open upon the cessation of fluid injection. The fracture walls are permeable shale rock and may exhibit "leak off." Reproduced from Chen, Barboza, Sun, *et al.* [30] under CC BY 4.0.

flow conditions present during fracking [28]. In fact, advanced experimental techniques that can interrogate proppant transport in the subsurface are only just now coming online [29].

1.2 Literature survey

1.2.1 Interfacial instability

In the 1950s, Hill [31], Saffman and Taylor [32], [33], and Chouke et al. [34] laid the foundations for the study of viscous fingering through both theoretical analysis and experiments.

Figure 1.3. Example interfacial instability: fern-like snowflake is a "multi-branched stellar dendrite crystal." Republished with permission of IOP Publishing Ltd, from "The Physics of snow crystals" by Libbrecht [38], *Reports on Progress in Physics*, vol. 68, pp. 855–895, © 2005 IOP Publishing Ltd; permission conveyed through Copyright Clearance Center, Inc.

Specifically, Hill [31] performed a one-dimensional (1D) stability analysis and conducted quantitative experiments for both stable and unstable interface between sugar liquors and water. Saffman and Taylor [32] considered a less viscous fluid (air) displacing a more viscous one (glycerine) in a Hele-Shaw cell [35], i.e., the thin gap between two closely spaced flat plates, and predicted the finger's growth rate via linear instability. Saffman and Taylor [32] additionally predicted and verified that when a single finger forms in a Hele-Shaw cell, it occupies nearly exactly half the horizontal width of the cell, for most experiments. Through the exact analogy of flow in a Hele-Shaw cell and flow in a two-dimensional (2D) porous medium under Darcy's law [36], [37], Saffman and Taylor [32] enabled a significant amount of theoretical and experimental research on interfacial instabilities.

Interfacial instabilities are quite common in nature and industry: the formation of snow flakes (see Fig. 1.3) [39], crystal growth [39], [40], the mixing in stratified flows [41], the ribbing instability in coating flows (see Fig. 1.4) [42]–[44], the formation of droplet clouds or sprays in combustion problems [45], the gravity-driven infiltration phenomena into initially dry homogeneous soil [46], drop and bubble dynamics in microfluidic devices [44], [47], to list a few. In most (but not) all cases, the instabilities are caused by a viscosity contrast

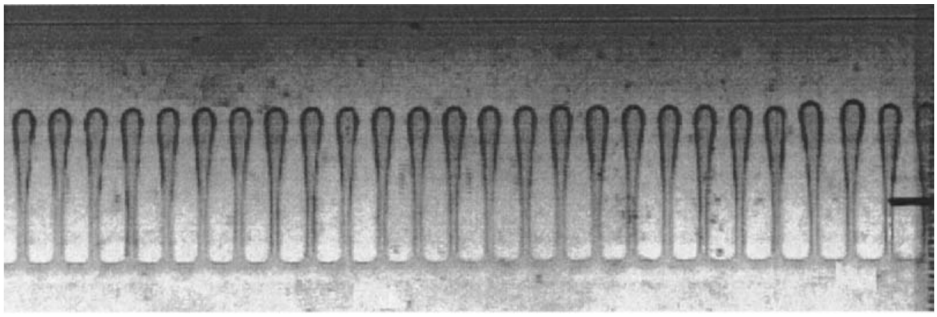

Figure 1.4. Example interfacial instability: ribbing. Reprinted from *Journal of Non-Newtonian Fluid Mechanics*, vol. 103, pp. 123–139, by Varela López, Pauchard, Rosen, and Rabaud, "Non-Newtonian effects on ribbing instability threshold" [48] © 2002 Elsevier, with permission.

at the fluid–fluid interface [36]. Finger-like patterns form as the unstable interface grows, which has led to this phenomenon being called *viscous fingering*.

Due to the importance of interfacial instabilities in narrow channels (or otherwise confined geometries) in many applications, attempts to control the viscous fingering have been made. For example, one can consider either natural of flow-driven geometric variations of the flow passage [49]–[59], one can control the injection flow rate [60]–[62], one can change the permeability by adjusting the structure of porous media [55], [63], [64], one can apply an external force via rotation of the geometry or through a magnetic field [65]–[69], one can change the fluid phase by using Non-Newtonian fluids [70]–[72] or adding particles [73]–[75], and so on. There are three ways to alter the physical geometry of an experimental Hele-Shaw apparatus: (i) creating a gradient along or perpendicular to the flow direction by relaxing the requirement that the plates be parallel [49]–[51], [53], [54], [59]; (ii) using an elastic membrane (that deforms due to flow underneath it) instead of a solid plate [58], [76]–[80]; and (iii) lifting one of the plates in a time dependent manner [60], [81]. Among these possibilities, the case of a geometric gradient in the flow direction has attracted special attention because it naturally imitates the non-uniform, fractured subsurface flow passages [7]. The gradient could be (a) a positive gradient for an increasing gap width in the flow direction (termed a *diverging* Hele-Shaw cell), or (b) a negative gradient for a decreasing gap width (termed a *converging* cell).

Currently, despite extensive research on the topic, the predictions of mathematical analysis have not taken the local capillary number into account. In tapered geometries, the local capillary number is not constant due to the changing mean velocity (under imposed flow rate), thus the interfacial stability characteristics change locally accordingly. Furthermore, the mathematical analysis have not been verified through three-dimensional (3D) direct numerical simulation (DNS) of flow and interfacial instability. In fact, a study by Dong, Yan, and Li [82] concluded that a "3D [numerical] model is preferred to obtain a better comparison with experimental results." Indeed, in 3D DNS, unlike physical experiments or the numerous previous simulations of the depth-averaged Hele-Shaw equations, we have control over the entire problem setup, which allows us to capture the full physics of the problem. The goal of this study is to fill this knowledge gap for rectangular Hele-Shaw cells with nonuniform gap thickness.

1.2.2 Fracture conductivity

To provide a sense of the scale on which the half-aperture h of a fracture may vary with the flow-wise direction x, consider the standard Perkins–Kern–Nordgren (PKN) [83] and the Khristianovitch–Zheltov–Geertsma–de Klerk (KGD) models, which idealize fractures as long and narrow elliptical cracks [84]. Garagash and Detournay [85] showed that the fracture tip has a shape with $h(x) \sim (x_{\text{tip}} - x)^{1/2}$ as $x \to x_{\text{tip}} > L$. (The typical fracture geometry we consider has total length L_{total}, appreciable variations in the shape occur over some typical scale $L \ll L_{\text{total}}$, with the tip falling outside the domain in Fig. 1.5.) Thus, the shape gradient away from the crack tip goes as $\alpha = dh/dx \sim -(x_{\text{tip}} - x)^{-1/2}$. Clearly, as $x \to -\infty$ (away from the crack tip), $|\alpha| \to 0^-$, justifying the small slope assumption $|\alpha| \ll 1$. Typical fracture geometry parameter values are summarized in Table 1.1, further justifying that, away from the crack tip, $dh/dx \sim |\alpha| \ll \epsilon = h_0/L$; that is, the fracture's typical slope is much smaller than its aspect ratio.

The simplest model of fracture conductivity (the parallel-plate model [86]) assumes that fracture walls are smooth, impermeable walls with a *constant* aperture of $2h_0$ (distance between the walls) and span w (length in the transverse direction); see Fig. 1.5. By analogy

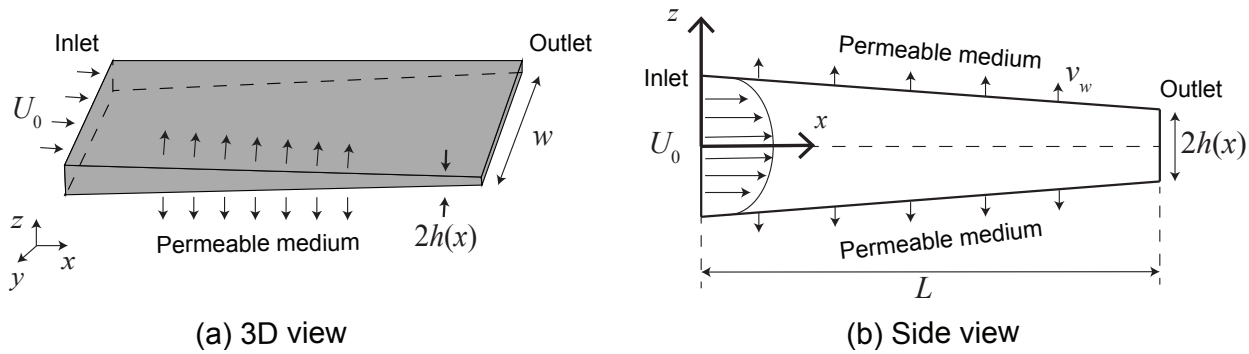

Figure 1.5. Schematic of a typical fracture flow geometry idealized as a Hele-Shaw cell. The fracture's shape varies appreciably over a "typical" length L, and it has a constant gradient $dh/dx \sim \alpha$, so that the half-aperture is $h(x) = h_0 + \alpha x$ (to a linear approximation). The fracture is long and thin meaning $\epsilon = h_0/L \ll 1$ and $\alpha = dh/dx = [h(L) - h_0]/L = \Delta h/L \ll 1$, where $h_0 = h(0)$. Gravity is neglected but, in these schematics, it would act in the transversely in the negative y-direction. The flow is symmetric about the centerline $z = 0$, and primarily in the x-direction, along the fracture. The top and bottom walls $z = \pm h(x)$ are permeable (permeability k_w) and allow a non-zero vertical velocity component v_w at the wall, which is to be determined.

to lubricating viscous flow between two plates (the so-called Hele-Shaw model [87]), one can calculate the hydraulic conductivity to be $\mathcal{K} = h_0^2/3$. Then, the transmissivity of the fracture ($\propto h_0 w \mathcal{K}$) follows the well-known "cubic law" [88]. However, the flow passages in both naturally [1] and hydraulically fractured [3] formations have a *variable* aperture $2h(x)$. Generally, the walls of fractures are not parallel [89], in part due to the flow-wise deformation of the fracture due to large injection pressures [90], requiring corrections to Darcy's laws arise via a modified conductivity and transmissivity models [91]–[93]. However, these models are for *impermeable walls*.

The bounding surfaces of a fracture are the porous rock formations themselves, therefore they should not be idealized as impermeable plates [94]. Permeation of gas into the matrix, and its subsequent diffusion, affects the late-years productivity of fractured wells [95], [96]. Berman [97] and Sellars [98] investigated the effects of a permeable wall in a constant-height channel using the idealized boundary condition of equal prescribed wall-normal velocities. Since then, a large literature has addressed many variations on this problem, including asymmetric wall normal velocities [99], flow development effects [100], unsteadiness [101],

Table 1.1. Typical dimensions of a hydraulic fracture and typical values of the dimensionless parameters of the hydraulic conductivity model derived in this study.

Quantity	Notation	Value	Remarks
Fracture total length	L_{total}	$100 \sim 1000$ m	[4]
Fracture width	w	$10 \sim 100$ m	[4]
Fracture gap/aperture	h_0	$2 \sim 10$ mm	[4]
Typical velocity	U_0	$\lesssim 10^{-3}$ m s^{-1}	[3]
Permeability of the wall	k_w	$\lesssim 5 \times 10^{-13}$ m^2	[4]
Hele-Shaw shape variation	$\delta = \alpha/\epsilon$	$\lesssim 10^{-1}$	Slow variation
Hele-Shaw aspect ratio	$\epsilon = h_0/L$	$10^{-4} \sim 10^{-2}$	Using $L = L_{\text{total}}/100$
Hele-Shaw slope	$\alpha = dh/dx$	$\lesssim 10^{-3}$	Using $\lvert\alpha\rvert \sim \epsilon\delta$
Wall slip coeff.	$\phi = \sqrt{k_w}/(bh_0)$	$\lesssim 10^{-3}$	$b = 0.1$
Reduced Reynolds number	$\tilde{Re} = \rho U_0 h_0^2/(\mu L)$	$\lesssim 0.1$	ρ, μ for water

and so on. These works rely on reducing the problem to a nonlinear ordinary differential equation, owing to the existence of a similarity transformation in two dimensions (2D). Unfortunately, this technique does *not* work in the case of a aperture gradient, such as the present geometry with $h = h(x)$; instead a perturbation solution must be sought [92], [102]. Kumar, Datta, and Kalyanasundaram [103] showed that a similar situation arises if the geometry is uniform but the slip length varies in the flow-wise direction, i.e., $\ell_{\text{slip}} = \ell_{\text{slip}}(x)$. Importantly, imposing the wall-normal velocity *a priori* is a significant limitation of the previous studies because, as Conlisk notes, "[t]he suction velocity at the wall ... must be calculated from the properties of the porous medium" [104, p. 162].

Beavers and Joseph [105] experimentally characterized pressure-driven (Poiseuille) flow over a naturally permeable surface (i.e., channel flow with porous walls) and proposed a boundary condition to account for the wall permeation. Specifically, they showed that the shear stress balance at the fluid–solid interface can be represented by a first-order (partial) slip boundary condition with slip length $\ell_{\text{slip}} = \sqrt{k_w}/b$, where k_w is the permeability of the porous wall, and b is a dimensionless constant determined by the structure of the material, ranging from 0.1 to 4.0 [105]. Taylor [106] observed that b is not a universal value, but rather it depends on the flow geometry. Saffman [107] substantiated this observation and generalized the slip condition to arbitrary surfaces. However, this correction only affects the

already empirically-determined slip length, thus the form of the boundary condition remains unchanged, while $b \approx 0.1$ is in good agreement with most experiments [108]. Zhang and Prosperetti [109] provided further evidence for the slip boundary condition via pore-scale direct numerical simulations of a two-dimensional channel flow. A more detailed discussion of the history and mathematical foundations of the partial slip boundary condition can be found in [110], [111]. Now, define the dimensionless quantity $\phi = \ell_{\text{slip}}/h_0$ as the slip coefficient. For the typical dimensions of a hydraulically-driven fracture, we estimate the dimensionless parameters values in Table 1.1.

To address the issue that fracture walls in the subsurface are themselves porous media, Mohais, Xu, Dowd, *et al.* [14] and Mohais, Xu, and Dowd [112] employed the Beavers–Joseph boundary condition to solve for the flow in, and obtain a correction for the conductivity $\mathcal{K}$ of, uniform-aperture fractures with permeable walls. So far, however, a theory for the conductivity of variable-aperture fractures with porous walls (the most common case in the subsurface) is lacking. This study aims to fill this knowledge gap.

1.2.3 Particle migration

Suspensions of particles in narrow channels are ubiquitously encountered both in nature and applications [113]. The particle's shape, surface properties, interactions between particles, and the carrier (suspending) fluid's viscoelasticity all contribute to the migration dynamics. Particle concentration changes in suspensions have been investigated by many researchers [114]–[122]. Karnis and Mason [115] conducted a pioneering experiment by measuring the particle accumulation along a fluid meniscus in a tube, specifically they found the inward displacement of particles near the meniscus. Gadala-Maria and Acrivos [123] observed a decrease in suspension viscosity after shearing, whereas the viscosity of the pure suspending fluid remain constant under the same circumstances. Later, Leighton and Acrivos [124] attributed this phenomenon to the shear-induced migration of particles, which reduces the particle concentration and thereby the viscosity. Tehrani [119] measured the particle concentration in fracking fluids, in which the elastic properties of the fluid and the shear-rate gradient both contribute to the migration of particles. It was found that, in

shear-thinning dominant fluids, particles migrate to regions of lower shear rate; in contrast, highly elastic fluids produce little or no migration. Semwogerere, Morris, and Weeks [122] observed that the distance required for the concentration profile to develop to steady state increases significantly with increasing Péclet number for $Pe \ll 100$ in Brownian suspensions, in marked contrast to non-Brownian suspensions. Here, the shear Péclet number is defined as $Pe = 6\pi\eta_0\dot{\gamma}a_p^3/(k_BT)$, where η_0 is the viscosity of the solvent, k_B is the Boltzmann constant, T is the temperature, a_p is the radius of an isolated Brownian particle, and $\dot{\gamma}$ is a characteristic shear rate (reciprocal of the characteristic time scale in the shear flow).

Theoretical analyses have also been performed to compute the particle concentration and velocity fields by shear-induced effect [116], [118], [121], or by the collaboration of shear-induced migration and buoyancy [120], Brownian motion [122] or gravity [125]. Some of the mathematical models used include the suspension balance model [126], [127], the diffusive flux model [118], [121], [125], [128], or other newly formulated

Meanwhile, numerical approaches have also been developed to simulate the particle migration effect [129]. Shiozawa and McClure [130] followed the numerical methods of Dontsov and Peirce [131], [132], which are based on a continuum model using the constitutive model from [133], and simulated the particle transport in a fully three-dimensional (3D) hydraulic fracture, capturing the transition from Poiseuille flow to Darcy flow as the particle laden fluids transitions from a dilute mixture to packed bed. Yeo and Maxey [134] used fully 3D numerical simulations on suspensions of non-colloidal monodisperse particles in a narrow channel (plane Poiseuille flow). They resolved the interparticle forces through the force-coupling method [135] based on singularity expansions of Stokes flow. The simulations results divide the channel into three regions: near-wall, intermediate and core region, with different particle velocity functions. Besides, complex geometries also attracted researchers' attention. Vigolo, Radl and Stone [21] predicted the location of particle accumulation in steady and pulsatile flows through T-junctions, via 3D numerical simulations and a model of the two-phase flow, and found agreement with theoretical trapping mechanism for low-density particles. More recently, Manoorkar, Krishnan, Sedes, *et al.* [136] simulated the suspension through a T-junction using discrete-particle simulations employing immersed boundary techniques and the lattice Boltzmann method.

Phillips, Armstrong, Brown, *et al.* [118] proposed an insightful phenomenological model for the shear-induced migration of particles in a low Reynolds number flow [124], including *a priori* unknown constants of order unity, which are found from experimental data (by fitting/calibration). The fluid mechanics of particulate suspensions remains a frontier problem [137], and the diffusive-flux model of Phillips, Armstrong, Brown, *et al.* [118] is not without its criticisms [138]. Nevertheless, although much more sophisticated models of suspensions exist [20], [139], including the suspension balance model [126], [127], [140]–[142], the two-fluid model [143], even direct numerical simulation [129], the phenomenological model of Phillips, Armstrong, Brown, *et al.* [118] remains a popular in the study of shear-induced particle migration in suspensions [144]–[146].

1.3 Knowledge gaps and organization of the thesis

The knowledge gaps identified by the literature survey in Sect. 1.2 will be addressed in different chapters of this thesis, organized as follows:

- While there has been extensive research on the interfacial stability in tapered geometries, the predictions of mathematical analysis have not taken the local capillary number into account. In tapered geometries, the local capillary number is not constant due to the changing mean velocity (under imposed flow rate), thus the interfacial stability characteristics change locally accordingly. Further, Dong, Yan, and Li [82] concluded that a "3D [numerical] model is preferred to obtain a better comparison with experimental results," which motivates the comparison of stability theory with direct numerical simulations (DNSs). Thus, clear gaps exist regarding the interfacial stability in tapered geometries: *What are the stability characteristics of a fluid–fluid interface in the presence of geometric variations, when the local capillary number might not be constant? Can these characteristics be predicted by theory? Can we validate the theory via 3D DNS?* These questions will be answered in Chapter 2 of this thesis.

- Currently, the theory of fracture conductivity is based on many assumptions: smooth, impermeable walls with a constant aperture and span. However, flow passages in both natural and fractured formations violate the assumptions. A knowledge gap in the lit-

erature on hydraulic conductivity of fractures exists regarding: *What is the conductivity of a variable-aperture fracture? What is the combined effect of geometric variation and permeation at the fracture's porous walls?* To answer these questions, in Chapter 3 of this thesis, we investigate the flow-wise variation of the hydraulic conductivity inside a non-uniformly shaped fracture with permeable walls, using lubrication theory for viscous flow in conjunction with the Beavers–Joseph–Saffman boundary condition at the porous wall.

- "Disentagling" the individual effects in phenomenological models of shear-induced migration of particles in a low Reynolds number flow has been of particular interest in the suspensions literature [118], [144], [147], yet a complete understanding of when and how to use these phenomenological models has not been achieved. The *a priori* unknown model parameters were only properly calibrated against experiments on flow in a concentric Couette cell. Subsequent studies on Poiseuille flows showed that the model is only in qualitative agreement with experiments. Therefore, a gap in the shear-induced migration literature pertains to: *What should be the values of the phenomenological model's parameters for shear-induce migrations in suspensions in Poiseuille flows? How can these parameters be obtained from previous experiments, for both Brownian and non-Brownian suspensions?* To answer these questions, in Chapter 4 we apply the novel physics-informed neural network (PINN) approach of Raissi, Perdikaris, and Karniadakis [148] towards understanding particle migration in shear flow.

2. INTERFACIAL DYNAMICS IN ANGLED HELE-SHAW CELLS: INSTABILITY REGIMES

SUMMARY

We present a theoretical and numerical study on the (in)stability of the interface between two immiscible liquids, i.e., viscous fingering, in angled Hele-Shaw cells across a range of capillary numbers (Ca). We consider two types of angled Hele-Shaw cells: diverging cells with a positive depth gradient and converging cells with a negative depth gradient, and compare those against parallel cells without a depth gradient. A modified linear stability analysis is employed to derive an expression for the growth rate of perturbations on the interface and for the critical capillary number (Ca_c) for such tapered Hele-Shaw cells with small gap gradients. Based on this new expression for Ca_c, a three-regime theory is formulated to describe the interface (in)stability: (i) in Regime I, the growth rate is always negative, thus the interface is stable; (ii) in Regime II, the growth rate remains zero (parallel cells), changes from negative to positive (converging cells), or from positive to negative (diverging cells), thus the interface (in)stability possibly changes type at some location in the cell; (iii) in Regime III, the growth rate is always positive, thus the interface is unstable. We conduct three-dimensional direct numerical simulations of the full Navier–Stokes equations, using a phase field method to enforce surface tension at the interface, to verify the theory and explore the effect of depth gradient on the interface (in)stability. We demonstrate that the depth gradient has only a slight influence in Regime I, and its effect is most pronounced in Regime III. Finally, we provide a critical discussion of the stability diagram derived from theoretical considerations versus the one obtained from direct numerical simulations.

The material in this chapter was published in [D. Lu, F. Municchi, and I. C. Christov, "Computational Analysis of Interfacial Dynamics in Angled Hele-Shaw Cells: Instability Regimes," *Transp. Porous Med.*, vol. 131, pp. 907–934, 2020] [149]

2.1 Problem statement

Currently, despite extensive research on the interface (in)stability analysis, the predictions of mathematical analysis have not taken the local capillary number into account. In tapered geometries, the local capillary number is not constant due to the changing mean velocity (under imposed flow rate), thus the interfacial stability characteristics change locally accordingly. Further, Dong, Yan, and Li [82] concluded that a "3D [numerical] model is preferred to obtain a better comparison with experimental results," which motivates the comparison of stability theory with direct numerical simulations (DNSs). The goal of this chapter is to fill this knowledge gap for rectangular Hele-Shaw cells with nonuniform gap thickness by: (i) extending the linear stability theory of interfacial instability in Hele-Shaw cell with clear fluids by taking into account the local streamwise variation of parameters (e.g., capillary number, depth of the cell, and so on); (ii) supplementing and verifying the theoretical analysis with "full" 3D DNS.

To this end, this chapter is organized as follows. In Sect. 2.2, we derive the (growth) decay rate of a (un)stable fluid–fluid interface between two immiscible phases in a Hele-Shaw with variable gap thickness (but constant gap gradient) via linear stability theory. Specifically, starting with Darcy's equation (i.e., the depth-averaged momentum equation) and the continuity equation, we obtain a Laplace equation for pressure. By solving the latter, we find the pressure jump at the fluid–fluid interface, and we match this pressure jump to the one found from the Young–Laplace equation. Thus, we arrive at the growth rate of the interface. On the basis of this mathematical result, we then classify the interface stability into three flow regimes depending on the difference between a critical capillary number and inlet or outlet capillary numbers, generalizing previous work on this problem by [53]. Next, in Sect. 2.4.1, we perform a series of DNSs (the methodology for which is described in Sect. 2.3) in a specific set of Hele-Shaw geometries. We use the simulations to verify our mathematical model (i.e., the theory developed in Sect. 2.2) for the growth rate of the interface. Then, in Sect. 2.4.2, we discuss the effect of the gap gradient on the stability based on the theoretical solution and further numerical experiments. In Sect. 2.4.3, we compare and discuss the flow regimes maps (in the 2D parameter space defined by the

capillary number and the gap gradient) determined by theoretical and numerical analyses. Finally, conclusions stated and avenues for future work are discussed in Sect. 2.5.

2.2 Linear stability analysis

Consider two immiscible and incompressible viscous fluids flowing in a narrow gap between two rigid plates (see Fig. 2.1) with a constant depth gradient α. The depth of the cell $h(x) = h_{in} + \alpha x$ satisfies $\max_x h(x) \ll W$ and $\max_x h(x) \ll L$. Although we neglect gravity, in Fig. 2.1 it would act in the negative z-direction. The flow is in the x-direction, and the Hele-Shaw cell's gap thickness, $h(x)$, only varies in this direction. The densities and viscosities of the displacing and defending fluids are denoted respectively as ρ_1, μ_1 and ρ_2, μ_2. A fully developed flow of fluid 1 (the displacing fluid), with an average (in the y-z cross-section) velocity U_{in}, pushes into a quiescent fluid 2 (the defending fluid). Between the two fluids there exists an interface that, due to immiscibility, is endowed with surface tension γ. The interface is not necessarily flat, and its shape is given by $x = \zeta(y, t)$. The horizontal direction perpendicular to the flow, i.e., the y-direction in Fig. 2.1, is assumed to be large compared to the typical gap size. Therefore, consistent with the linear stability analysis to be carried out below (and also previous work of [53], [150]), we consider the interface to be periodic in y. Specifically, we shall apply a full-period initial perturbation to an initially flat interface to respect the periodic boundary conditions (PBCs) at $y = 0$ and $y = W$. Experiments have shown that PBCs have a similar effect to physical sidewalls in a cylindrical Hele-Shaw cell [151], i.e., two coaxial cylinders separated by a small gap.

2.2.1 Linear growth rate

Following [54], we start our linear stability analysis with the 2D (i.e., depth- or z-averaged) governing equations for the viscous fluid flow in the thin gap between two closely spaced plates [37]:

$$\boldsymbol{u}_j = -\frac{h^2}{12\mu_j}\boldsymbol{\nabla} p_j, \tag{2.1}$$

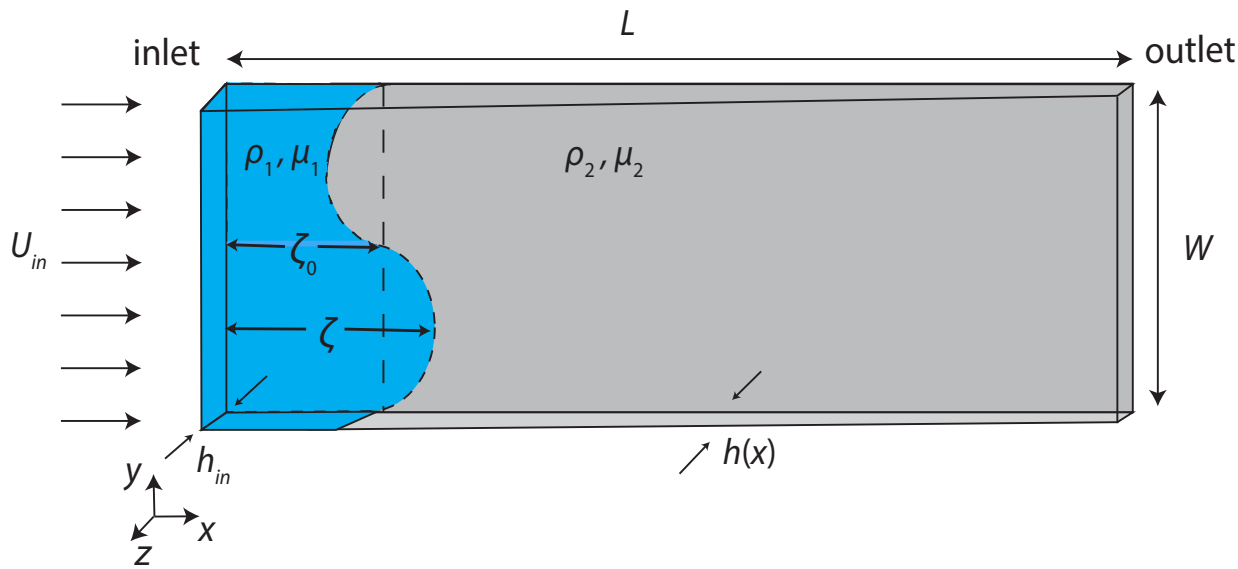

Figure 2.1. Top view schematic configuration of the flow in a rectilinear Hele-Shaw cell with a constant depth gradient α. The depth of the cell, $h(x) = h_{in} + \alpha x$, satisfies $\max_x h(x) \ll W$ and $\max_x h(x) \ll L$ and h_{in} is the depth at the inlet. Although we neglect gravity, in this view it would act in the negative z-direction. The flow is in the x-direction, and the Hele-Shaw cell's gap thickness, $h(x)$, only varies in this direction.

where the subscript $j = 1, 2$ represents the displacing and defending fluid, respectively; $\boldsymbol{u}_j$ is the depth-averaged velocity field of fluid j in the (x, y) plane, p_j is the pressure field of fluid j, while h and μ_j were defined above (see also Fig. 2.1). Equation (2.1) is supplemented by the continuity (conservation of mass) equation for each incompressible fluid phase:

$$\boldsymbol{\nabla} \cdot (h\boldsymbol{u}_j) = 0. \tag{2.2}$$

The flow has been assumed to be fully developed and steady.

Substituting Eq. (2.1) into Eq. (2.2), we obtain the governing equation for the pressure in each fluid

$$\boldsymbol{\nabla}^2 p_j + \frac{3\alpha}{h(x)} \frac{\partial p_j}{\partial x} = 0. \tag{2.3}$$

In an angled Hele-Shaw cell, the depth is $h(x) = h_{in} + \alpha x$, so

$$\frac{1}{h(x)} = \frac{1}{h_{in} + \alpha x} = \frac{1}{h_{in}} - \frac{\alpha x}{h_{in}^2} + \mathcal{O}(\alpha^2). \tag{2.4}$$

Substituting Eq. (2.4) back into Eq. (2.3), and neglecting the $\mathcal{O}(\alpha^2)$ terms (consistent with the lubrication approximation under which Eq. (2.1) is derived [see, e.g., 37]), the pressure equation now has constant coefficients:

$$\frac{\partial^2 p_j}{\partial x^2} + \frac{\partial^2 p_j}{\partial y^2} + \frac{3\alpha}{h_{in}} \frac{\partial p_j}{\partial x} = 0 \qquad (\alpha \ll 1). \tag{2.5}$$

Next, assume a flat base state for the (unperturbed) interface shape, denoted $\zeta(y,t) = \zeta_0(t)$. Then, we express the perturbed interface as a Fourier series:

$$\zeta(y,t) = \zeta_0(t) + \sum_{n \neq 0} \epsilon_n a_n e^{ik_n y + \lambda_n(t)}, \tag{2.6}$$

which satisfies the condition of periodic boundary conditions (PBCs) in y. In Eq. (2.6), the time derivative of $\lambda_n(t)$, denoted henceforth as $\dot{\lambda}_n$ and not necessarily constant, represents the growth rate of mode n, and $k_n = 2\pi n/W$ is its spatial wave number. We take $k_n > 0$ without loss of generality. The magnitude of each perturbation mode is quantified by a dimensionless number ϵ_n, and $\epsilon_{n'} \neq \epsilon_n$ for any two modes n' and n in a mode-coupling analysis [150]. In the present work, we restrict ourselves to a single mode analysis, thus the sum may be dropped:

$$\zeta(y,t) = \zeta_0(t) + \epsilon a e^{iky + \lambda(t)}. \tag{2.7}$$

This approximation is justified since all mode coupling terms would be at least second order, or more specifically, coupling of modes n' and n would be of order $\epsilon_{n'}\epsilon_n$, which would be dropped eventually in our linear stability analysis below.

Next, we expand each phase's pressure p_j in perturbation series. Consistent with the interfacial perturbation in Eq. (2.7), only terms up to $\mathcal{O}(\epsilon)$ are kept:

$$p_j(x,y,t) = p_{0j}(x;t) + \epsilon p_{1j}(x,y;t), \tag{2.8}$$

where $p_{0j}(x;t)$ represents the base state, i.e., the pressure drop across the channel under uniform displacement. Meanwhile, $p_{1j}(x,y;t)$ is the pressure perturbation due to the interfacial disturbance. Note that the perturbative pressure expansion from Eq. (2.8) satisfies the steady PDE, i.e., Eq. (2.5), but may depend on time as a parameter due to the fluid–fluid interface's motion. Consistent with these definitions, the pressure gradient of the base state $p_{0j}(x;t)$ satisfies Darcy's equation and $p_{1j}(x,y;t)$ must vanish away from the interface, i.e., $\lim_{x\to-\infty} p_{11}(x,y;t) = \lim_{x\to+\infty} p_{12}(x,y;t) = 0$.

We proceed by expressing the pressure perturbation as a Fourier series:

$$p_{1j}(x,y;t) = \sum_n g_{jn}(x) e^{ik_n y + \lambda_n(t)}, \qquad j = 1, 2, \tag{2.9}$$

where each $g_{jn} = \mathcal{O}(1)$. Again, Eq. (2.9) can be reduced to a single-mode representation due to higher-order terms being dropped in our linear stability analysis:

$$p_{1j}(x,y;t) = g_j(x) e^{iky + \lambda(t)}. \tag{2.10}$$

Solving the pressure equation by substituting Eqs. (2.8) and (2.10) into Eq. (2.5) (see Appendix for details), we obtain the pressure jump across the fluid–fluid interface:

$$\begin{aligned}\Big(p_1 - p_2\Big)\Big|_{x=\zeta(y,t)} &= \frac{4U\Big(\zeta_0(t)\Big)h_{in}}{\alpha[h(\zeta_0(t))]^2}(\mu_1 - \mu_2) \\ &+ \epsilon e^{iky+\lambda(t)} \frac{a\gamma Ca}{[h\Big(\zeta_0(t)\Big)]^2} \left\{ (1-M) - \left[\frac{\dot{\lambda}}{U\Big(\zeta_0(t)\Big)} + \alpha \left(\frac{3}{h_{in}} - \frac{2}{h\Big(\zeta_0(t)\Big)} \right) \right] \frac{1+M}{k} \right\} \\ &\qquad + \mathcal{O}(\epsilon^2) \qquad (\alpha \ll 1),\end{aligned} \tag{2.11}$$

where $Ca := 12U\mu_2/\gamma$ is the definition of the capillary number, γ is the interfacial surface tension as before, $M := \mu_1/\mu_2$ is defined as the ratio of the fluids' viscosities, and $U = U\Big(\zeta_0(t)\Big)$ and $h = h\Big(\zeta_0(t)\Big)$ are the local (non-constant) velocity and depth at the unperturbed interface, respectively. It follows that Ca also depends on t, implicitly, through $U\Big(\zeta_0(t)\Big)$ and $h\Big(\zeta_0(t)\Big)$; however, we have left this dependency implicit to simplify the notation.

On the other hand, the capillary pressure jump at the interface $x = \zeta(y,t)$ also satisfies the Young–Laplace equation. If the defending fluid wets the wall, i.e., the contact angle between the defending fluid and the wall is $\theta_c = 0$, then Park and Homsy's analysis [152] yields

$$\left(p_1 - p_2\right)\Big|_{x=\zeta(y,t)} = \frac{2\gamma}{h[\zeta(y,t)]}\left(1 + 3.8Ca^{2/3} + \cdots\right) + \frac{\gamma}{R}\left[\frac{\pi}{4} + \mathcal{O}(Ca^{2/3})\right], \tag{2.12}$$

where R is the radius of curvature of the interface, and we have taken into account the variable gap depth, $h[\zeta(y,t)] \neq const.$, as suggested by [153]. Neglecting higher-order terms (in this linear, $Ca \ll 1$ analysis), Eq. (2.12) simplifies to

$$\left(p_1 - p_2\right)\Big|_{x=\zeta(y,t)} = \frac{2\gamma}{h[\zeta(y,t)]} + \frac{\pi}{4}\frac{\gamma}{R}. \tag{2.13}$$

If the wetting is not perfect, considering the contact angle θ_c, the pressure jump is written as

$$\left(p_1 - p_2\right)\Big|_{z=\zeta(y,t)} = \gamma\left\{\frac{2\cos\theta_c}{h[\zeta(y,t)]} + f(\theta_c)\kappa\right\}, \tag{2.14}$$

where $\kappa = 1/R$ is the curvature of the interface, defined as

$$\begin{aligned}\kappa &:= -\frac{\partial^2\zeta/\partial y^2}{[1 + (\partial\zeta/\partial y)^2]^{3/2}} \\ &= -\frac{\partial^2\zeta}{\partial y^2}\left[1 - \frac{3}{2}\left(\frac{\partial\zeta}{\partial y}\right)^2 + \mathcal{O}\left(\left(\frac{\partial\zeta}{\partial y}\right)^4\right)\right] \\ &= k^2\epsilon a e^{iky+\lambda(t)} + \mathcal{O}(\epsilon^2),\end{aligned} \tag{2.15}$$

and $f(\theta_c)$ is a function of the contact angle to account for the interface curvature within the gap [36], [152]. Specifically, based on the analysis of [154],

$$f(\theta_c) = \left(\frac{\pi}{4} - \frac{\theta_c}{2}\right)\frac{1 + \sin\theta_c}{\cos\theta_c}. \tag{2.16}$$

Of course, this general expression yields the two standard cases: $f(0) = \pi/4$ and $f(\pi/2) = 1$ (interpreted as a limit).

Now, using the expansion in Eqs. (2.4) and (2.15), Eq. (2.14) becomes

$$\Big(p_1 - p_2\Big)\Big|_{x=\zeta(y,t)} = \frac{2\gamma\cos\theta_c}{h\Big(\zeta_0(t)\Big)} + \epsilon a\gamma e^{iky+\lambda(t)}\left\{f(\theta_c)k^2 - \frac{2\cos\theta_c\alpha}{[h\Big(\zeta_0(t)\Big)]^2}\right\} + \mathcal{O}(\epsilon^2). \tag{2.17}$$

Matching the $\mathcal{O}(\epsilon)$ terms in Eqs. (2.11) and (2.17), we obtain

$$e^{iky+\lambda(t)}\frac{Ca\gamma a}{[h\Big(\zeta_0(t)\Big)]^2}\left\{(1-M) - \left[\frac{\dot{\lambda}}{U\Big(\zeta_0(t)\Big)} + \alpha\left(\frac{3}{h_{in}} - \frac{2}{h\Big(\zeta_0(t)\Big)}\right)\right]\frac{1+M}{k}\right\}$$
$$= \left\{f(\theta_c)k^2 - \frac{2\alpha\cos\theta_c}{[h\Big(\zeta_0(t)\Big)]^2}\right\}\gamma a e^{iky+\lambda(t)}. \tag{2.18}$$

Rearranging the last equation, yields the *final form* of our theoretical prediction for the growth rate $\dot{\lambda}(t)$ of an interface between immiscible fluids in a rectilinear Hele-Shaw cell with a constant depth gradient α:

$$(1+M)\left[\frac{\dot{\lambda}}{U\Big(\zeta_0(t)\Big)} + \alpha\left(\frac{3}{h_{in}} - \frac{2}{h\Big(\zeta_0(t)\Big)}\right)\right]$$
$$= \left(1 - M + \frac{2\alpha\cos\theta_c}{Ca}\right)k - \frac{f(\theta_c)k^3[h\Big(\zeta_0(t)\Big)]^2}{Ca} \qquad (\alpha \ll 1). \tag{2.19}$$

Equation (2.19) differs from the solution discussed by [54] in that it does not assume an instantaneous development of the instability; rather the dynamics occurs over a finite time span during which the interface "sees" the cell's depth variation. Thus, Eq. (2.19) captures the dynamic interplay between the growth/decay of a perturbation and the flow-wise geometric variations it encounters, as exemplified by $h\Big(\zeta_0(t)\Big)$. Specifically, we have defined a non-constant $Ca = 12U\mu_2/\gamma$, where $U = U\Big(\zeta_0(t)\Big)$ is *not* the fixed inlet value but, rather, it is the average velocity at some downstream cross-section $x = \zeta_0(t)$. $U = U\Big(\zeta_0(t)\Big)$ can be easily determined by conservation of mass; see, e.g., the discussion of Eq. (2.24) below. Consequently, $\lambda(t)$ is governed by an *ordinary differential equation* (not an algebraic equation), and it may grow (or decay, or both) during its time evolution, despite the sign of $\dot{\lambda}$ obtained from a "frozen-time" linear stability analysis [155].

In the absence of a depth gradient, i.e., $\alpha = 0$ (thus, U and $Ca = const.$), Eq. (2.19) reduces to

$$\dot{\lambda} = \left(\frac{1-M}{1+M}\right) Uk - \frac{f(\theta_c)h_{in}^2 U}{Ca(1+M)}k^3, \tag{2.20}$$

which agrees exactly with the growth rate for the fingering instability given by Homsy [36] for $\theta_c = \pi/2$, and if gravity and the Rayleigh–Darcy convection terms are neglected therein.

2.2.2 Classification of instability regimes

The threshold of instability is determined by setting $\dot{\lambda} = 0$. Then, from Eq. (2.19), we obtain

$$3\alpha(1+M) = \left(1 - M + \frac{2\alpha\cos\theta_c}{Ca}\right) h_{in}k - \frac{f(\theta_c)[h\big(\zeta_0(t)\big)]^2 h_{in}}{Ca}k^3 \qquad (\alpha \ll 1). \tag{2.21}$$

Solving for the *critical* capillary number, Ca_c, for fixed k in Eq. (2.21), we obtain

$$Ca_c = \frac{2\alpha\cos\theta_c - f(\theta_c)k^2[h\big(\zeta_0(t)\big)]^2}{(1+M)\left(\frac{3}{h_{in}} - \frac{2}{h\big(\zeta_0(t)\big)}\right)\frac{\alpha}{k} + (M-1)}. \tag{2.22}$$

This critical capillary number determines the threshold of instability for the fluid–fluid interface. The interface is stable if $Ca < Ca_c$; it is unstable if $Ca > Ca_c$. To the best of our knowledge, Eq. (2.22) is a new result because Ca_c implicitly depends on the interface location $x = \zeta_0(t)$ through $h\big(\zeta_0(t)\big)$. Now, let us consider the possible flow and instability regimes in Hele-Shaw cells with a gap gradient by analyzing Eq. (2.22) in detail. Importantly, these flow regimes could not be determined (i.e., they do not exists) in previously analyses based on a fixed Ca_c.

Parallel cell.

In this case, there is no depth gradient, i.e., $\alpha = 0$, and Eq. (2.22) becomes

$$Ca_c = -\frac{f(\theta_c)k^2 h_{in}^2}{(M-1)}. \tag{2.23}$$

The capillary number is constant along the cell, i.e., $Ca(x) \equiv Ca_{in} = Ca_{out}$. So, the critical capillary number delineates three regimes when compared with the inlet capillary number:

- **Regime I**: $Ca_{in} < Ca_c$. In this regime, the growth rate is negative, $\dot{\lambda} < 0$. The finger's growth is suppressed, and the interface becomes flat asymptotically.
- **Regime II**: $Ca_{in} = Ca_c$. In this regime, the growth rate is zero, $\dot{\lambda} = 0$. The finger's growth is neither inhibited nor triggered (i.e., this represents a marginally stable case). The finger's length remains constant, and linear stability cannot determine whether an initial perturbation will grow or decay.
- **Regime III**: $Ca_{in} > Ca_c$. In this regime, the growth rate is positive, $\dot{\lambda} > 0$. The interface is unstable and the finger's growth is triggered.

Diverging cell.

In this case, $\alpha > 0$. The depth-averaged velocity of a stable flat interface is intrinsically a function of the channel's depth along the flow direction due to conservation of mass. This leads us to specifically decompose the capillary number into an inlet (constant) and local (variable) contribution:

$$Ca = \frac{12\mu_2 U}{\gamma} = Ca_{in}\frac{h_{in}}{h(\zeta_0)}, \tag{2.24}$$

where $Ca_{in} = 12\mu_2 U_{in}/\gamma$ and h_{in} are the constant capillary number and depth at the inlet of the cell. Ca as defined in Eq. (2.24) is implicitly a function of t through ζ_0. This local Ca decreases with x because the velocity is decreasing for a diverging cell (expanding cross-sectional area). Although Ca_c decreases as well, according to Eq. (2.22), as $h(\zeta_0)$ increases, the change of the local Ca is faster than Ca_c. Therefore, we can still introduce three regimes by comparing the local Ca with Ca_c:

- **Regime I**: $Ca_{in} < Ca_c$. In this regime, the growth rate is always negative, $\dot{\lambda} < 0$, and the finger's growth is inhibited.
- **Regime II**: $Ca_{in} > Ca_c$ and $Ca_{out} < Ca_c$. In this regime, the growth rate is positive, $\dot{\lambda} > 0$, at the inlet, *but* changes sign becoming negative, $\dot{\lambda} < 0$, at some point down-

stream in the cell. Thus, the finger's length initially increases but then saturates and would be expected to decrease at longer times.

- **Regime III**: $Ca_{out} > Ca_c$. In this regime, the growth rate is always positive, $\dot{\lambda} > 0$, and the initial finger perturbation grows in time.

Converging cell.

In this case, $\alpha < 0$. Now, local capillary number from Eq. (2.24) increases along the flow direction. Again, three instability regimes can be defined by comparing the local Ca with Ca_c:

- **Regime I**: $Ca_{out} < Ca_c$. In this regime, the growth rate is always negative, $\dot{\lambda} < 0$, and the finger's growth is inhibited.

- **Regime II**: $Ca_{in} < Ca_c < Ca_{out}$. In this regime, the growth rate is negative, $\dot{\lambda} < 0$, at the inlet, *but* changes sign becoming positive, $\dot{\lambda} > 0$, at some point downstream in the cell. The finger's length decreases initially but grows at longer times.

- **Regime III**: $Ca_{in} > Ca_c$. In this regime, the growth rate is always positive, $\dot{\lambda} > 0$, and the initial finger perturbation continues to grow in time.

It is important to note that this analysis predicts that, in diverging and converging cells, Regime II exists for a *finite* range of Ca_{in} values. This observation is in stark contrast to the parallel cells for which Regime II is simply the marginally stable case $Ca_{in} = Ca_c$. Thus, in diverging and converging Hele-Shaw cells, the stability of a perturbation may change during its evolution. Previous studies of elastic-walled Hele-Shaw cells also commented on this effect [156, §4.2.1].

Now, to illustrate these three regimes for parallel, diverging and converging Hele-Shaw cells, in Fig. 2.2, we plot the growth rate $\dot{\lambda}$ as a function of the inlet capillary number Ca_{in} and the dimensionless flow-wise position $x^* = x/L$. The contact angle is assumed to be $\pi/2$, so we take $f(\theta_c) = 1$. In these plots, $x^* = 0$ and $x^* = 1$ represent the inlet and outlet, respectively. The intersection between a given $\dot{\lambda}$ surface and the horizontal plane

$\dot{\lambda} = 0$ indicates a transition in (in)stability. Thus, our classification of instability into three regimes becomes clear. Regime I is to the left of the line of intersection, Regime III is to the right of this line, and Regime II refers to cases in which the line of intersection is crossed only for some range of Ca_{in} values. For example, in a parallel cell (Fig. 2.2a), the line of intersection is parallel to the x^* axis, thus Regime II corresponds to one specific value of Ca_{in}. For that value of Ca_{in}, the interface is neutrally stable. In a diverging cell (Fig. 2.2b) or a converging cell (Fig. 2.2c), on the other hand, the line of intersection is crossed for a *range* for Ca_{in} values, as one goes from the inlet to the outlet, i.e., from $x^* = 0$ to $x^* = 1$.

Furthermore, by comparing the growth rates in Figs. 2.2b and 2.2c, we observe that, for larger Ca_{in}, the growth rate in a converging cell could be greater than that in a diverging cell. This observation could explain the recent counterintuitive simulation results reported by [55], in which while the perturbation in a converging Hele-Shaw cell has a larger growth rate than in a parallel cell, the perturbation's growth rate in a diverging cell can be smaller, for large Ca_{in}, than a in parallel cell.

2.3 Direct numerical simulations

Numerical simulations are carried out using the interFoam solver [157], [158] implemented in OpenFOAM® ver. 6.0 [159], an open-source library based on the *finite volume method* (FVM) [160]. In this analysis, the fluids are considered as incompressible, immiscible and unsteady. As depicted in Fig. 2.1, the fluids flow through a Hele-Shaw cell with a depth that varies with x. The contact angle between the displacing fluid and the wall is taken to be $\theta_c = \pi/2$ (the interface is flat across the depth). Three types of cells are considered: converging (negative depth gradient, $\alpha < 0$), parallel (zero gradient, $\alpha = 0$), and diverging (positive depth gradient, $\alpha > 0$).

Below, we present numerical "experiments" (studies) based on water (fluid 1) injected into mineral oil (fluid 2). The corresponding fluid properties, geometric parameters and flow quantities used for these simulations are summarized in Table 2.1. In simulations, the U_{in} values used are back-calculated from Ca_{in}.

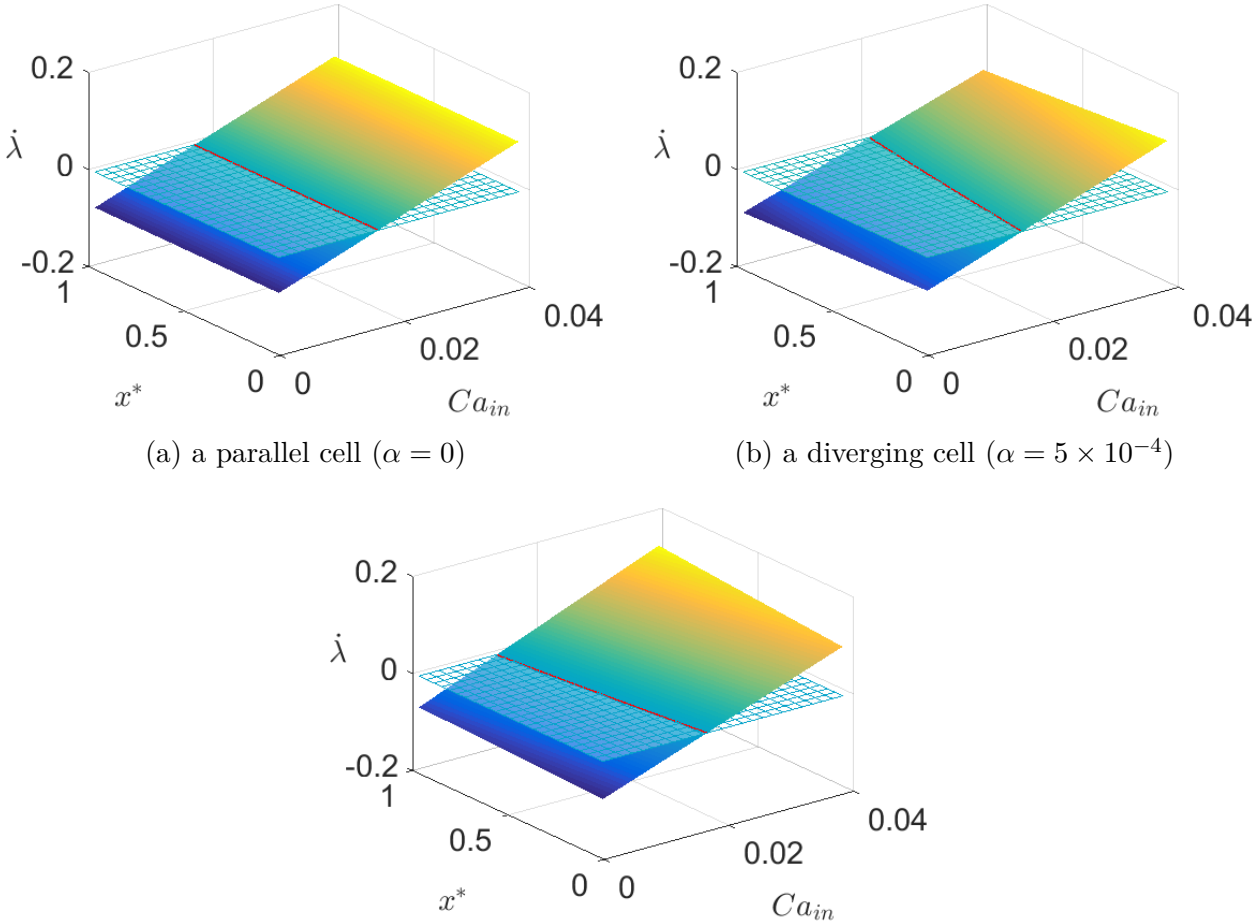

(a) a parallel cell ($\alpha = 0$)

(b) a diverging cell ($\alpha = 5 \times 10^{-4}$)

(c) a converging cell ($\alpha = -5 \times 10^{-4}$)

Figure 2.2. The growth rate $\dot{\lambda}$ as a function of inlet capillary number Ca_{in} and the flow-wise dimensionless position $x^* = x/L$ in different cells: (a) a parallel cell, (b) a diverging cell, and (c) a converging cell, with $M = 0.0154$ and other geometric/material properties as in Table 2.1. The intersection of the growth rate surface (shaded) and the $\dot{\lambda} = 0$ surface (meshed) is marked by red lines, indicating the change of sign of $\dot{\lambda}$ and an exchange of stability.

2.3.1 Governing equations

In our DNS study, we solved the "full" 3D Navier–Stokes equation directly in each fluid, instead of the simplified and depth-averaged equations commonly solved in previous numerical studies. Specifically, the governing equations solved by the interFoam implementation

Table 2.1. Fluid properties, geometric parameters and flow quantities used for the numerical simulations.

Property	Value (SI units)
μ_1	1.0×10^{-3}
ρ_1	1.0×10^{3}
μ_2	6.50×10^{-2}
ρ_2	8.30×10^{2}
γ	2.95×10^{-2}
θ_c	$\pi/2$

Quantity	Value (SI units or –)
h_{in}	1×10^{-3}
W	5×10^{-2}
L	2×10^{-1}
α	$0, \pm 5 \times 10^{-4}, \pm 10 \times 10^{-4}$
Ca_{in}	0.0067 to 0.0200

[158] in OpenFOAM® are the conservation of mass and momentum for a *two-fluid mixture*, written as:

$$\boldsymbol{\nabla} \cdot \boldsymbol{v} = 0, \tag{2.25}$$

$$\frac{\partial(\varrho \boldsymbol{v})}{\partial t} + \boldsymbol{\nabla} \cdot (\varrho \boldsymbol{v} \otimes \boldsymbol{v}) = -\boldsymbol{\nabla} p + \boldsymbol{\nabla} \cdot [\eta(\boldsymbol{\nabla} \boldsymbol{v} + \boldsymbol{\nabla} \boldsymbol{v}^{\top})] + \boldsymbol{F}, \tag{2.26}$$

where $\varrho = \varrho(x, y, z, t)$ is the mixture density, $\boldsymbol{v} = \boldsymbol{v}(x, y, z, t)$ is the mixture velocity, $p = p(x, y, z, t)$ is the pressure, $\eta = \eta(x, y, z, t)$ is the mixture viscosity, and $\boldsymbol{F}$ is a fictitious body force used to enforce surface tension at the fluid–fluid interface. Physically, this body force due to surface tension results in a pressure jump at the interface, and it is evaluated (per unit volume) by the continuum surface force (CSF) model [161], [162]:

$$\boldsymbol{F} = \gamma \kappa \boldsymbol{\nabla} \phi, \tag{2.27}$$

where γ is the surface tension, and $\kappa = -\boldsymbol{\nabla} \cdot (\boldsymbol{\nabla}\phi / \|\boldsymbol{\nabla}\phi\|)$ is the mean curvature of the fluid–fluid interface computed directly from its surface normals. Here, $\phi = \phi(x, y, z, t)$ is the phase fraction in a given cell of the computational grid, defined as

$$\phi \begin{cases} \in (0,1) & \Rightarrow \text{Interface;} \\ = 1 & \Rightarrow \text{Fluid 1;} \\ = 0 & \Rightarrow \text{Fluid 2.} \end{cases} \tag{2.28}$$

The phase fraction keeps track of where each fluid ("1" and "2") goes in the computational domain. We stress that this "mixture" model does not consider "different" physics than the mathematical model in Sect. 2.2; this is simply a numerical approach to handling dissimilar fluids separated by an immiscible interface.

In the interFoam solver, the phase fraction ϕ is solved using a modified volume-of-fluid (VOF) method [163]:

$$\frac{\partial \phi}{\partial t} + \boldsymbol{\nabla} \cdot (\phi \boldsymbol{v}) + \boldsymbol{\nabla} \cdot (\phi(1-\phi)\boldsymbol{v}_r) = 0, \tag{2.29}$$

where $\boldsymbol{v}_r = \boldsymbol{v}_1 - \boldsymbol{v}_2$ is the relative velocity between the two fluids. The fluid properties of the mixture, as well as the mixture velocity, to be used in Eqs. (2.25) and (2.26), can thus be expressed as

$$\varrho = \phi\rho_1 + (1-\phi)\rho_2, \tag{2.30a}$$

$$\eta = \phi\mu_1 + (1-\phi)\mu_2, \tag{2.30b}$$

$$\boldsymbol{v} = \phi\boldsymbol{v}_1 + (1-\phi)\boldsymbol{v}_2, \tag{2.30c}$$

where the subscripts "1" and "2" refer to *fluid 1* (displacing) and *fluid 2* (displaced/defending), respectively. Eqs. (2.25), (2.26) and (2.29) are discretized spatially using the FVM and integrated in time via an Euler implicit scheme. Convection terms are discretized using a linear upwind scheme, while diffusion terms are discretized using a linear scheme. Gauss integration is employed for both terms, and gradients are corrected to account for non-

orthogonal fluxes, which occur in angled cells. The Navier–Stokes solution algorithm used in interFoam is "PIMPLE," which is a combination of the *pressure-implicit with splitting of operators* (PISO) method [164], [165] and the *semi-implicit method for pressure-linked equations* (SIMPLE) [165], [166]. In PIMPLE, PISO is used as the inner loop corrector to update pressure and velocity, and SIMPLE is used as the outer loop corrector to ensure convergence. Thus, PIMPLE achieves a more robust pressure-velocity coupling.

2.3.2 Mesh generation

When performing numerical simulations, on one hand, it is important to have a mesh that is fine enough to capture the physical properties accurately; on the other hand, a mesh with fewer cells saves computational resources. To balance accuracy and efficiency, we only refine the mesh in the region of interest, which in the present problem is the fluid–fluid interface. We use a relatively coarse mesh for the remainder of the Hele-Shaw cell. Since the interface is moving, adaptive mesh refinement is employed. At every time step the mesh is dynamically refined in the spatial region where $0.001 < \phi(x, y, z, t) < 0.999$, i.e., close to the interface to ensure it is well resolved. The initial mesh resolution is given in Table 2.2.

Table 2.2. Mesh generation for grid and time independence test(s) parameters for a parallel cell. For converging and diverging cells, only Δz changes.

Case ID	1	2	3
Grid elements	750	6,000	48,000
Grid resolution, Δx [m]	8×10^{-3}	4×10^{-3}	2×10^{-3}
Grid resolution, Δy [m]	5×10^{-3}	2.5×10^{-3}	1.25×10^{-3}
Grid resolution, Δz [m]	3.33×10^{-4}	1.67×10^{-4}	8.33×10^{-5}
Time step [s]	10^{-3}	10^{-4}	10^{-5}

2.3.3 Initial and boundary conditions

At the inlet ($x = 0$), we employ a horizontal velocity profile that satisfies no-slip at $z = 0, h_{in}$, i.e., $u_x(z) = -6U_{in}(z/h_{in} - 1/2)^2 + (3/2)U_{in}$, as the boundary condition for

the mixture velocity. A zero-gradient boundary condition is employed for the flow at the outlet ($x = L$), except the pressure, which is fixed to zero to set the gauge. Initially, fluid 1 and fluid 2 are separated by a flat interface $x = \zeta_0 = 20$ mm. An initial perturbation is applied at the interface, i.e., $\zeta(y, 0) = \zeta_0[1 + \epsilon \sin(ky)]$ (see Fig. 2.3a). The initial magnitude of the perturbation is set by $\epsilon = 0.2$, and its wavenumber is $k = 2\pi/W$. Along the top ($z = h(x)$) and bottom ($z = 0$) plates of the cell, a no-slip boundary condition is prescribed. All variables are assumed to be periodic at the side (lateral) ends, $y = 0$ and $y = W$, of the cell. An example simulation under these initial and boundary conditions is shown in Fig. 2.3, highlighting how the initial perturbation can grow or decay, and how the interface remains sharp due to adaptive mesh refinement.

2.3.4 Grid and time step independence test

Three sets of simulations on different meshes, as listed in Table 2.2, were conducted to show grid and time step independence. We compute the deviation of the finger's length, defined as $\xi(t) := \max_y[\zeta(y, t)] - \zeta_0(t)$, and found from linear stability analysis to be $\xi_{\text{la}}(t)$, to the simulation prediction $\xi_{\text{ns}}(t)$, as:

$$\varepsilon(t) = \left| \frac{\xi_{\text{ns}}(t) - \xi_{\text{la}}(t)}{\xi_{\text{la}}(t)} \right|. \tag{2.31}$$

The results in Fig. 2.4 show that the difference in the values of $\varepsilon(t)$ between case 2 and case 3 (less than 1%) is insignificant for the purposes of this study. Therefore, for the remainder of the present work, we will employ case 2 as the simulation grid of choice. This grid is less demanding in terms of computational resources than the grid from case 3.

2.4 Results: Comparing theory to simulations and stability regimes

2.4.1 Verification of the linear stability analysis

Hu, Wang, and Sun [167] already performed extensive verification of the interFoam solver's use for simulating viscous fingering in a Hele-Shaw cell of constant depth. Importantly, they showed that simulations can capture quite accurately experimental and the-

Table 2.3. Classification of cases for simulations used for verification of the linear theory.

	$Ca_{in} = 0.0067$	$Ca_{in} = 0.0147$	$Ca_{in} = 0.0200$
Converging cell ($\alpha = -5 \times 10^{-4}$)	Case 4	Case 5	Case 6
Parallel cell ($\alpha = 0$)	Case 7	Case 8	Case 9
Diverging cell ($\alpha = 5 \times 10^{-4}$)	Case 10	Case 11	Case 12

oretical predictions about the length and width of a *single* finger, as in the classical [32] experiments and analysis.

In this subsection, we explore flows in angled Hele-Shaw cells with different capillary numbers for converging ($\alpha < 0$), parallel ($\alpha = 0$) and diverging ($\alpha > 0$) cell geometries as cataloged by the 'cases' in Table 2.3. We wish to verify the linear stability theory from Sect. 2.2 through numerical simulations. Before we discuss the numerical results in detail, it is instructive to make a few remarks. First, the linear analysis holds, strictly speaking, only at the moment of initiation (onset) of instability. Nevertheless, the linear analysis is generally used in the literature to describe the unstable interface's evolution. Additionally, here for simplicity and for consistency with some previous analyses, only one Fourier mode was used to represent the perturbation. At later times in the displacement process, the simulations capture the full nonlinear unstable interface evolution, which is expected to be qualitatively similar (but quantitatively different) than the prediction of the linear analysis. This specific point is of interest to us in the present work. Even when linear theory does not provide precise quantitative prediction about the interface's evolution (and, instead, direct numerical simulations must be used), linear theory correctly delineates the stability regimes and their transitions in the capillary number–depth gradient, i.e., (Ca, α), space.

The first verification results are presented in Fig. 2.5 for each of the three types of Hele-Shaw cells in panels (a), (b) and (c). Solid and dotted lines refer to numerical and theoretical results, respectively. Lines with different symbols represent different cases from Table 2.3 with different inlet capillary numbers Ca_{in}. The finger's length ξ (left panels) and growth rate $\dot{\lambda}(t)$ (right panels) are plotted as functions of time. The theoretical predictions are computed from Eqs. (2.6) and (2.19) with $\xi(t) = \max_y[\zeta(y,t)] - \zeta_0(t)$. Numerical results

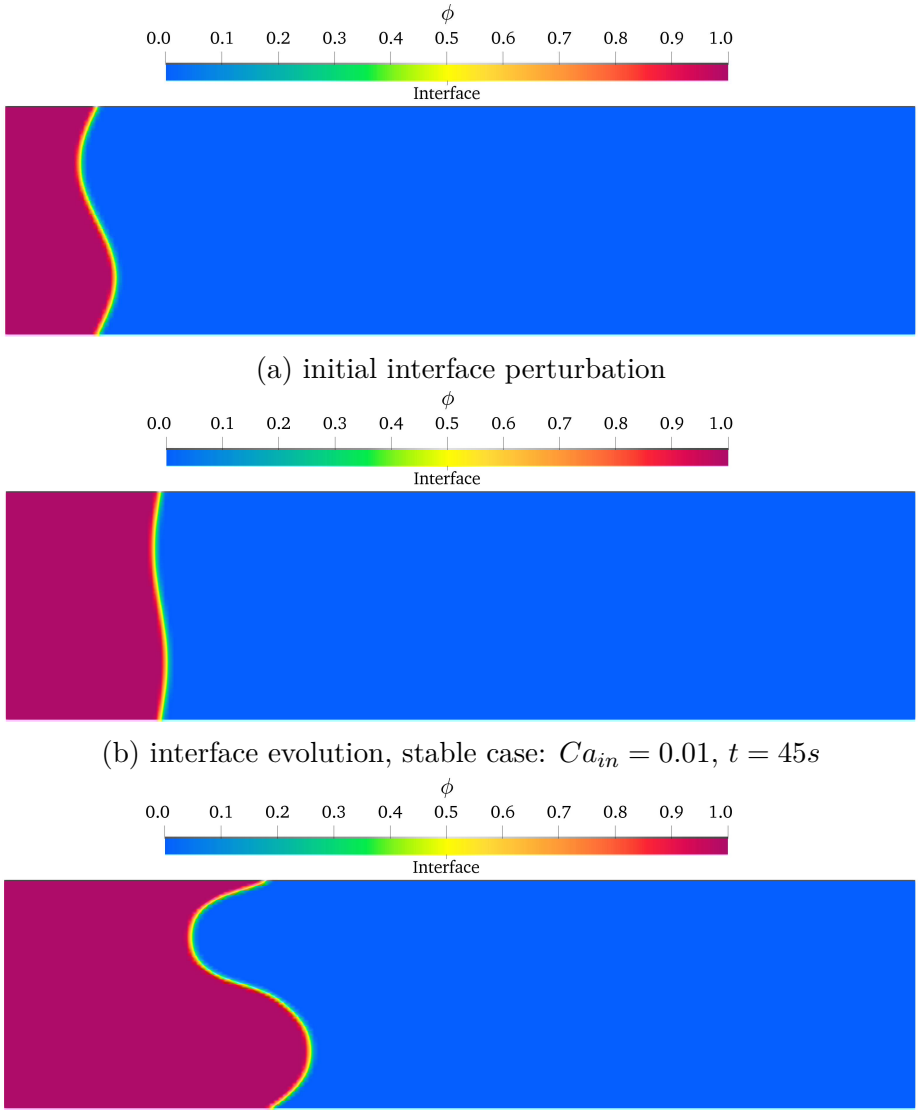

(a) initial interface perturbation

(b) interface evolution, stable case: $Ca_{in} = 0.01$, $t = 45s$

(c) interface evolution, unstable case: $Ca_{in} = 0.03$, $t = 45s$

Figure 2.3. Top view of example simulation of interface evolution in a converging cell ($\alpha = -5 \times 10^{-4}$).

are post-processed from the simulation data; the finger's length is calculated as $\xi(t) = \{\max_y[\zeta(y,t)] + \min_y[\zeta(y,t)\}/2$, and the growth rate is calculated as $\dot{\lambda}(t) = [1/\xi(t)]d\xi/dt$ using the cubic-spline interpolation with smoothing available in SciPy [168].

Numerical results and linear stability analysis agree very well at $Ca_{in} = 0.0200$ in each cell: Case 6 in Fig. 2.5a; Case 9 in Fig. 2.5b; and Case 12 in Fig. 2.5c. In these cases, the finger's length $\xi(t)$ increases over time and the growth rate $\dot{\lambda}(t)$ remains positive, meaning

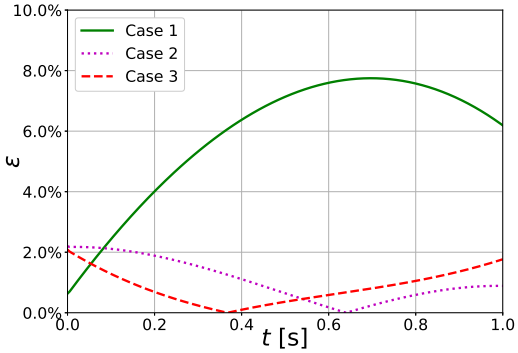

(a) parallel cell ($\alpha = 0$)

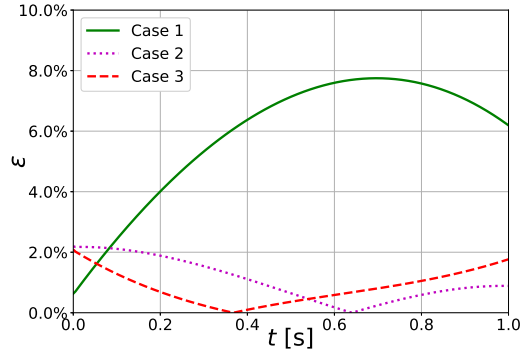

(b) diverging cell ($\alpha = 5 \times 10^{-4}$)

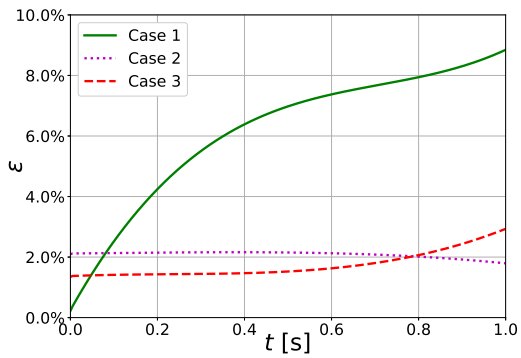

(c) converging cell ($\alpha = -5 \times 10^{-4}$)

Figure 2.4. Grid and time step independence tests show the % difference in the fingers length (between linear stability and numerical simulation) as a function of time. Clearly, the simulation parameters in case 2 and case 3 lead to very similar results, so case 2 shall be employed for all simulations herein.

that the interface is unstable, which corresponds to Regime III in classification introduced in Sect. 2.2. At $Ca_{in} = 0.00147$, numerical simulations show a roughly constant finger's length. The growth rate is almost zero (Case 8 in Fig. 2.5b), or suffers a change of sign (Case 5 in Fig. 2.5a and Case 11 in Fig. 2.5c). At this value of Ca_{in} we are reminded of Regime II from the linear stability analysis. As Ca_{in} is decreased to 0.0067, simulations show that $\xi(t)$ continues to decay, and $\dot{\lambda}(t)$ is always negative: Case 4 in Fig. 2.5a; Case 7 in Fig. 2.5b; and Case 10 in Fig. 2.5c.

Therefore, the prediction from linear stability theory regarding three instability regimes has been verified through numerical simulations. However, the quantitative prediction of the growth rate from linear analysis is most accurate in Regime III, which corresponds to

the classical Saffman–Taylor instability. In Regime I and II, our results quantify the difference between the linear model and 3D DNS. Indeed, as the interface becomes flattened, it is increasingly less meaningful to try to define the finger's length as the difference between maximum and minimum extent. In this case, integrated metrics such as the isoperimetric ratio have been preferred by other authors [169]. Moreover, we have verified that the evolution of the perturbations according to linear stability theory and DNS match more closely (quantitatively) for smaller perturbation magnitudes, e.g., taking $\epsilon = 0.05$ or even 0.02. However, to better resolve these very small (and slower growing perturbations), a finer mesh should be used. The effect of the perturbation magnitude ϵ is not an emphasis of the present study, hence these details are omitted for brevity. As mentioned earlier, we use the small but not infinitesimal value of $\epsilon = 0.2$ in all of our DNS results.

2.4.2 The effect of the flow-wise depth gradient

In this subsection, we investigate the effect of the depth gradient α on the growth/decay of perturbations on the fluid–fluid interface. The various cases with different values of α are cataloged in Table 2.4. The theoretical predictions and numerical results for the growth rate $\dot{\lambda}(t)$, as defined in Sect. 2.2, in these different (in)stability regimes are shown in Figs. 2.6a, 2.6c and 2.6e, respectively, for different values of α. The results show that as α increases, $\dot{\lambda}$ decreases. In other words, following the terminology most recently used in [170], the diverging cells have a relatively stabilizing effect in all three regimes, while converging cells relatively destabilize the interface, compared to the interface evolution in a parallel cell for the same value of Ca_{in}. Specifically, the growth rate from 3D simulations is not constant, but varies with time, which qualitatively verifies our novel extension of previous linear stability analysis (Sect. 2.2).

To further compare the effect of the depth gradient in each regime, in Fig. 2.6b, 2.6d and 2.6f, we present the integral of growth rate over time, i.e., $\lambda(t) = \int_0^t \dot{\lambda}(t')\,dt' = \int_{\xi(0)}^{\xi(t)} d\xi'/\xi' = \ln|\xi(t)| - \ln|\xi(0)|$, which is computed over the first 20 s of simulation time. In Regime I (see Fig. 2.6 top row), the simulation results show that the depth gradient has a slight effect on the interface: the integral of the growth rate λ decreases slightly with α. The present linear

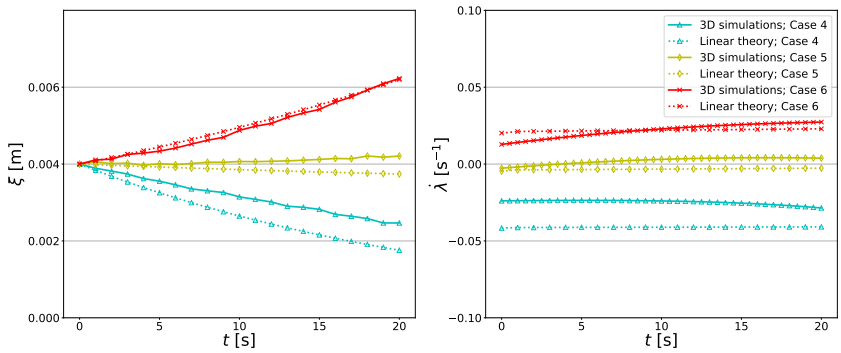

(a) a converging cell with $\alpha = -5 \times 10^{-4}$

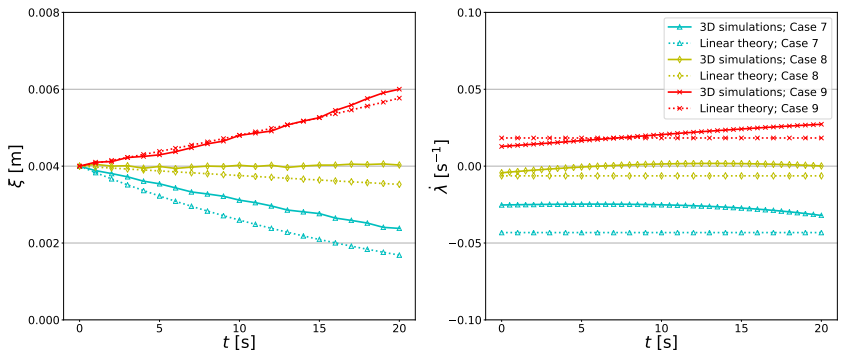

(b) a parallel cell with $\alpha = 0$

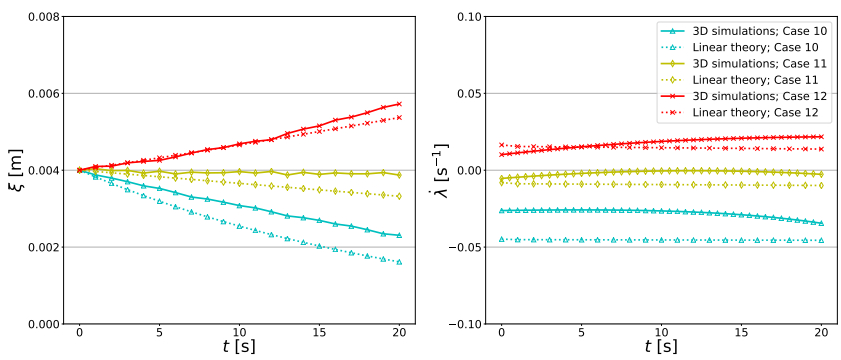

(c) a diverging cell with $\alpha = 5 \times 10^{-4}$

Figure 2.5. Linear stability analysis verification for the finger's length $\xi(t)$ and the growth rate $\dot{\lambda}(t)$ in (a) a converging cell (Cases 4, 5, 6), (b) a parallel cell (Cases 7, 8, 9), (c) a diverging cell (Cases 10, 11, 12). Colors represent different inlet Ca, as labelled. Simulations results (solid curves) verify the three regimes theory: blue solid curves (decreasing ξ and $\dot{\lambda} < 0$) are in Regime I, yellow solid curves (roughly constant ξ and $\dot{\lambda} \approx 0$) are in Regime II, and red solid curves (increasing ξ and $\dot{\lambda} > 0$) are in Regime III.

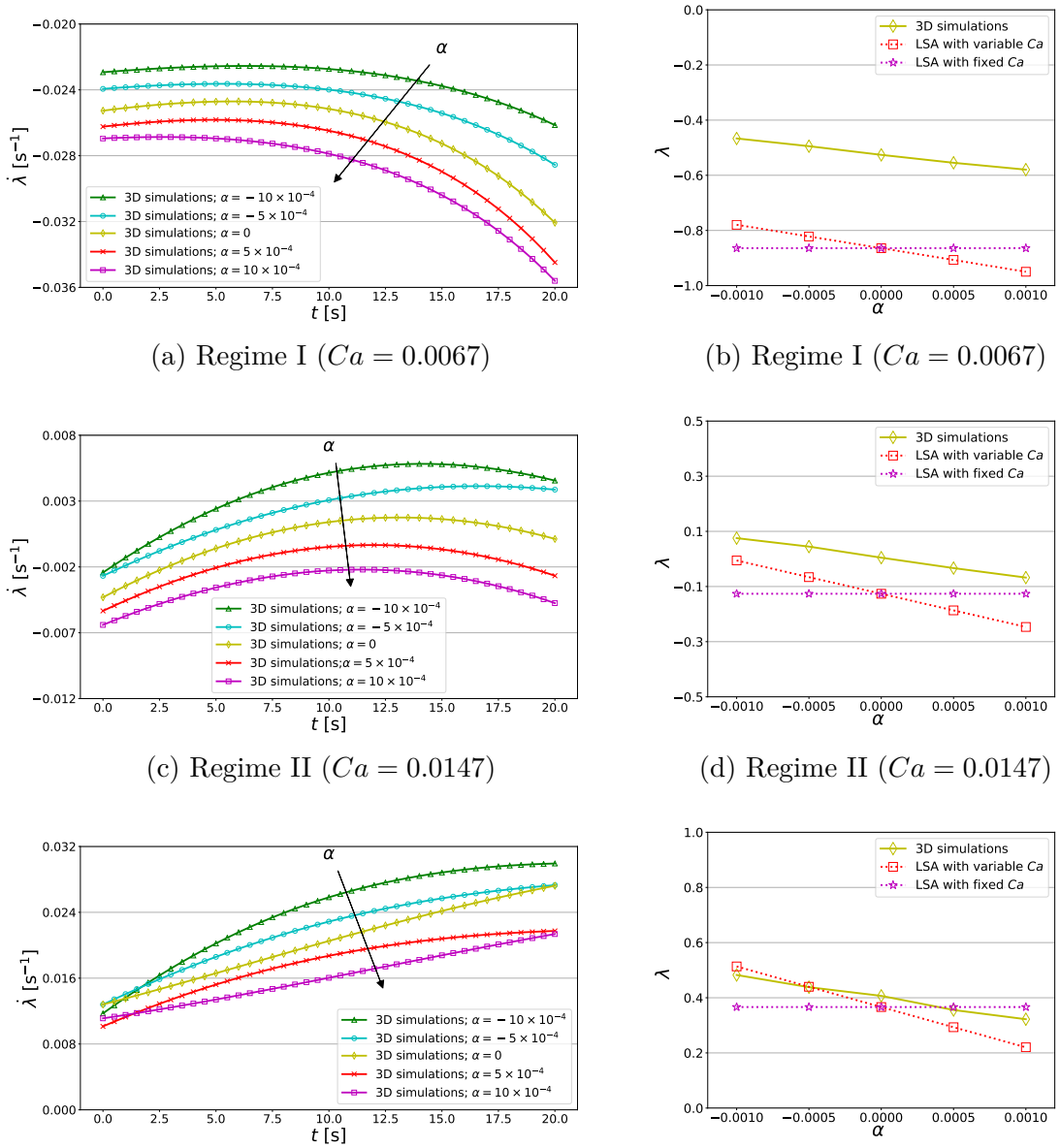

(a) Regime I ($Ca = 0.0067$)

(b) Regime I ($Ca = 0.0067$)

(c) Regime II ($Ca = 0.0147$)

(d) Regime II ($Ca = 0.0147$)

(e) Regime III ($Ca = 0.0200$)

(f) Regime III ($Ca = 0.0200$)

Figure 2.6. The effect of depth gradient α on the growth rate $\dot{\lambda}(t)$ (a,c,e) and the integral of the growth rate λ (b,d,f), in the three regimes. As α increases, $\dot{\lambda}$ decreases. The growth rate from 3D simulations is not constant but varies with time, which qualitatively verifies our linear stability analysis from Sect. 2.2, denoted as "LSA with variable Ca." "LSA with fixed Ca" stands for the quasi-steady analysis of [53]. LSA with fixed Ca does not capture the decreasing trend of λ with α obtained by the present LSA with variable Ca and 3D DNS. In turn, the latter exaggerates the gradient's effect compared to DNS.

Table 2.4. Classification of the simulations conducted to ascertain the effect of the depth gradient.

	Regime I $Ca_{in} = 0.0067$	Regime II $Ca_{in} = 0.0147$	Regime III $Ca_{in} = 0.0200$
$\alpha = -10 \times 10^{-4}$	Case 13	Case 14	Case 15
$\alpha = -5 \times 10^{-4}$	Case 4	Case 5	Case 6
$\alpha = 0$	Case 7	Case 8	Case 9
$\alpha = 5 \times 10^{-4}$	Case 10	Case 11	Case 12
$\alpha = 10 \times 10^{-4}$	Case 16	Case 17	Case 18

stability analysis exaggerates the gradient's effect: the predicted slope of λ, as a function of α, is larger than the one from DNS. We conjecture that a weakly-nonlinear stability analysis (e.g., extending the work of [150] to the case of an angled Hele-Shaw cell), which keeps higher-order terms in the perturbation expansion, could correct this exaggeration. Moreover, since λ is decreasing and negative, then the suppression of viscous fingering that exists in Regime I is most effective in *diverging* cells, and the larger α, the better. This result is somewhat counterintuitive compared to discussion in [53] wherein converging cells are described as the most stabilizing; however, in [53] the three regime diagram proposed herein was obviously not considered.

In Regime II (see Fig. 2.6 middle row), the effect of the gradient is stronger than in Regime I: as α increases, λ decreases more rapidly. The gap gradient has the most significant effect in Regime III (see Fig. 2.6 bottom row), indicating that the triggering of fingering in Regime III is most clearly observed in converging cells, and the larger $|\alpha|$, the better. Returning to the comparison with the previous linear stability analysis from [53] (dotted lines with stars in Fig. 2.6b, 2.6d and 2.6f), we observe that it does not capture the decreasing trend of λ with α, specifically because in our simulations we have taken a contact angle of $\theta_c = \pi/2$.

In general, the linear stability analysis provides a theoretical explanation for the DNS results, specifically in the prediction of the dependence of the growth rate on the depth gradient α in an angled Hele-Shaw cell (Fig. 2.6b, 2.6d and 2.6f). As the capillary number decreases, the discrepancy between theory and simulation increases, as is to be expected for this $Ca \ll 1$ linear theory. In particular, one way to understand this observation is to

note that as Ca_{in} decreases, the interface becomes more and more flattened, and the finger's length is no longer a sensitive metric.

2.4.3 Stability diagram

In Sect. 2.4.1, the linear analysis was verified through numerical simulations of flows throughout the three regimes of the proposed stability classification. However, for marginal cases near the dividing curves between two regimes, we observed that the predictions of the linear theory do not quantitatively agree with DNS. To better understand this discrepancy, we conducted further numerical experiments to explore the numerical regime map for various depth gradient values α. In this subsection, we compare the numerical regime diagram to the theoretically predicted one. The result is shown in Fig. 2.7. Other stability diagrams from previous research [59], [64], [74] have shown the (in)stability by linear stability analysis, experiments, or both. Here, we supplement the diagram with 3D direct numerical simulation results, and make a comparison with the linear stability analysis.

The theoretical division of (in)stability regimes in a Hele-Shaw cell is based on the local capillary number at the inlet, Ca_{in}. The critical capillary number Ca_c for a particular angled Hele-Shaw cell is obtained from Eq. (2.22). By setting $Ca_{in} = Ca_c$ or $Ca_{out} = Ca_c$, we obtain the Ca_{in} and Ca_{out} values at the onset of the stability transition, respectively. Then, we refer both critical cases back to Ca_{in}, by computing the corresponding value of Ca_{in} for $Ca_{out} = Ca_c$. Thus, we obtain two sets of Ca_{in} values, computed from setting $Ca_{in} = Ca_c$ and from $Ca_{out} = Ca_c$, respectively, which divide the flow into three regimes in the (α, Ca_{in}) plane.Note that the stability diagram depends on the Hele-Shaw cell's geometry because the Ca_{in} that we compute from $Ca_{out} = Ca_c$ is related to the length of the channel. However, in our simulation the interface never reaches the end of the Hele-Shaw cell. Therefore, the horizontal length scale to be used in the nondimensionalization should be reconsidered to determine whether the interface will change its stability during its transit of the initial length of the Hele-Shaw cell. To make a reasonable comparison with the simulation results, we evaluate Ca_{out} at $x = 40$ mm, the maximum distance reached by the interfaces in the simulations.

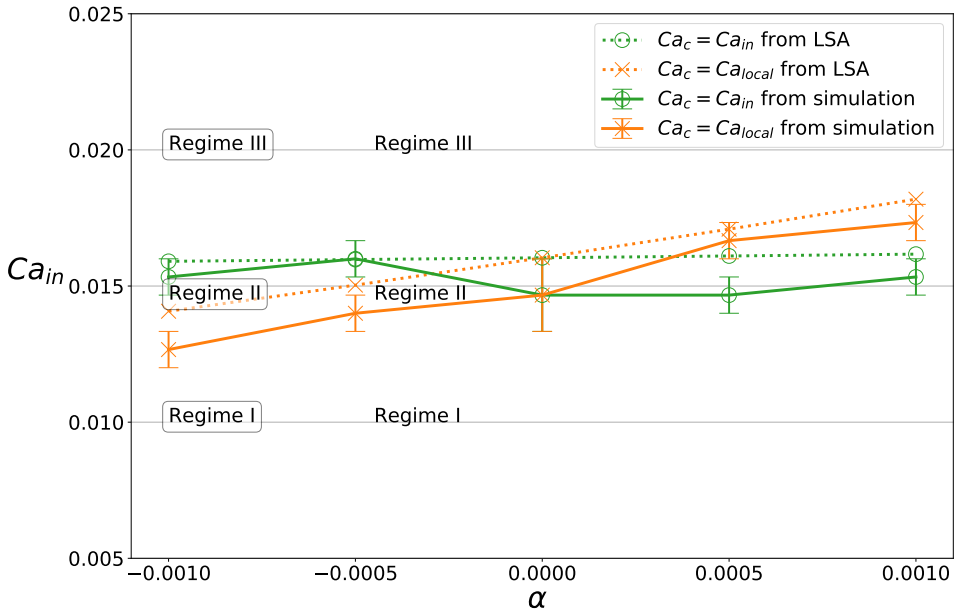

Figure 2.7. Stability Diagram: theoretical and numerical results are plotted as dashed and solid curves, respectively. Green and orange curves represent the critical situations such that $Ca_c = Ca_{in}$ and $Ca_c = Ca_{local}$, respectively. The error bars represent the difference in Ca_{in} between two simulations. The boxed regimes are those defined by the linear theory and the others are those defined via direct numerical simulations.

The theoretically predicted regime divisions are shown in Fig. 2.7 as dashed curves. The Ca_{in} values calculated from $Ca_{in} = Ca_c$ are plotted with circles, while the ones obtained from $Ca_{local} = Ca_c$ are plotted with crosses. Note that there is an intersection between the two curves at $\alpha = 0$ because in this case there is no sense in which to distinguish Ca_{in} from Ca_{local}. For $\alpha \neq 0$, the local capillary number at the inlet Ca_{in} is the minimum capillary number in converging cells ($\alpha < 0$), while it is the maximum capillary number in diverging cells ($\alpha > 0$). Therefore, the critical Ca_{in} from $Ca_{in} = Ca_c$ separates Regime II from Regime III in converging cells, while it separates Regime I from Regime II in diverging cells. The intersection could also be interpreted as follows: as $|\alpha|$ decreases, the range of Regime II narrows, finally collapsing to a point for $\alpha = 0$ (parallel cell, i.e., the "classical" Saffman–Taylor case).

Solid curves are the results of direct numerical simulations, representing the division of the parameter space into three regimes as predicted by the 3D evolution of the interface. Numerical experiments were carried out for $\alpha = 0,\ \pm 5\times 10^{-4}$ and $\pm 10\times 10^{-4}$, across multiple Ca_{in} values ranging from 0.0067 to 0.02 with a step of 0.0013. The numerical results show a general agreement with the theoretically predicted regime map, except for Regime II. This is not surprising because the marginally stable regime is hard to capture in simulations.

The stability diagram in Fig. 2.7 also captures the effect of depth gradient on the regimes: as α increase, the regimes boundaries move up to larger Ca_{in} values. In particular, we observe that simulations predict a much weaker dependence on α than the linear stability analysis.

2.5 Conclusions

In this chapter, we analyzed the instability of the interface between immiscible viscous fluids in angled Hele-Shaw cells with small constant depth gradient in the flow-wise direction. We performed a linear stability analysis, and we derived an analytical solution for the time-dependent (not constant) growth rate $\dot{\lambda}(t)$ of perturbations to a flat interface. Our theoretical result takes into account the geometric variations and the local capillary number Ca due to the changing cross-sectional area of the flow conduit. Specifically, we have analyzed the case, not previously considered, of the interface instability developing on a time scale on which the flow-wise geometric variations matter. Consequently, dynamic changes in stability were shown to be possible during the interface's propagation. Then, we obtained a critical capillary number Ca_c by letting $\dot{\lambda} = 0$. By comparing the local capillary number with Ca_c, we put forward a division of the stability diagram into three regimes. In Regime I, the interface is always stable; in Regime II, the interface remains neutrally stable (in a parallel cell), while in angled cells, an exchange of stability occurs at a specific position in the cell: from stable to unstable (in a converging cell), or from unstable to stable (in a diverging cell). This regime classification implies, in particular, that whether or not a depth gradients is stabilizing (or destabilizing) for a given inlet flow rate (thus, given capillary number) depends on which regime the flow falls into. Therefore, a negative depth gradient (converging geometry) is not generically a stabilizing mechanism.

Next, we performed 3D direct numerical simulations of the same physical system, using the interFoam solver built onto the OpenFOAM® platform, in order to verify the proposed three regimes theory. In Regime III, the finger's length and growth rate computed from simulations agree well with theoretical predictions, verifying the linear stability analysis for the classical Saffman–Taylor instability. Meanwhile, in Regimes I and II, the simulation results support the regimes' existence, but do not match the $\dot{\lambda}$ values predicted by linear stability, due to the former's limitations discussed above.

More importantly, however, the proposed linear theory, when compared to the simulation results, correctly captures the general dependence of the interface growth rate on the depth gradient. Specifically, in Regime I, simulation results show that the integral of the growth rate λ decreases slightly with the gap gradient; meanwhile, linear stability analysis exaggerates the effect, which is expected to be corrected by employing a weakly-nonlinear stability analysis. Simulations also suggest that the suppression of fingering in Regime I is most robust in diverging angled Hele-Shaw cells. Furthermore, in Regime II, the effect of the gradient is stronger than that in Regime I. The gap gradient's effect is significant in Regime III, in which case it acts to trigger the fingering instability, especially in converging cells. In all three regimes, the diverging (converging) cells have a relatively stabilizing (destabilizing) effect, with respect to the interface evolution in parallel cells for the same Ca value, which is contrary to the intuition developed in recent experimental studies.

Finally, we compared the regime stability diagram in the (α, Ca_{in}) plane as predicted by theory and as computed from simulations. Although there are some expected systematic sources of error between theory and simulation here, the stability diagram in Fig. 2.7, to the best of our knowledge, for the first time, compares 3D direct numerical simulations with linear stability analysis of instability in an angled Hele-Shaw cell. Consequently, the present work might provide a framework through which to understand interfacial (in)stability in the presence of geometry variations. Specifically, researchers may:

1. compare quantitatively their simulation or experimental results against the stability diagram (Fig. 2.7) to determine in which regime applies, and therefore understand whether the depth gradient is stabilizing or destabilizing;

2. solve the ordinary differential equation (2.19) for the growth of the interface under the specific flow and geometric conditions of their simulation or experiment, to determine the expected behavior of perturbations of the fluid–fluid interface (growth, decay, or *both*).

Additionally, we hope that this stability diagram provides a methodology for addressing the question of how one might improve the sweep efficiency of fluid–fluid displacements in complex fractured rock composed of a network of non-uniform passages. For example, if the flow (for a particular diverging or converging flow passage) can be controlled and forced into Regime I, or at least into Regime II, the interfacial instabilities can be mitigated. Such fundamental understanding of fingering control can also be employed to minimize the risk of geomechanical phenomena during overflushing. In fact, it was shown [171] that viscous fingering (occurring in Regime III) causes a non-uniform sweep of proppants in a fracture, which are important to distribute uniformly to prevents the fracture's collapse.

Further work considering a weakly-nonlinear analysis with mode coupling to extend the predictive capability of the stability theory is appended in Sect. 2.A.2. In future, direct numerical simulation could be employed to verify studies on the critical wave number k_c at fixed Ca, such as the prior work of [150]. In fact, simulations possess a crucial advantage over experiments: simulations allow precise control over the initial conditions, including the wave number of the interfacial disturbance. Finally, the effects of shear-dependent viscosity [172], yield stress [173] and viscoelasticity [174] on the interfacial instability in angled Hele-Shaw cells should be investigated, building upon the previous work in parallel cells. This aspect of future work is particularly relevant given that non-Newtonian fluids are commonly used in hydraulic fracturing applications [4], [6].

2.A Appendix

2.A.1 Supplementary steps in the main analytical derivations

To derive the pressure jump at the interface, we first substitute Eq. (2.8) into Eq. (2.5) and collect terms at $\mathcal{O}(1)$ to obtain

$$\frac{d^2 p_{0j}}{dx^2} + \frac{3\alpha}{h_{in}} \frac{dp_{0j}}{dx} = 0, \qquad j = 1, 2 \qquad (\alpha \ll 1). \tag{2.32}$$

Solving the ordinary differential equation in Eq. (2.32), we have

$$p_{0j} = C_{1j} e^{-3\alpha x / h_{in}} + C_{2j}. \tag{2.33}$$

Here, the constants C_{2j} are set by the arbitrary pressure gauge for each fluid; specifically, we can set $C_{2j} = 0$ without loss of generality. (Eq. (2.3) can also be solved without the linearization in α that leads to Eq. (2.32) [175]. However, it is not clear whether the significantly more complicated expressions contribute much within the lubrication approximation with $\alpha \ll 1$.) Now, we must specify boundary conditions. At the interface, $x = \zeta = \zeta_0(t) + \mathcal{O}(\epsilon)$, the x-velocities at the leading order (i.e., for an unperturbed interface) must match:

$$\lim_{x \to \zeta_0^-} u_{x1} = \lim_{x \to \zeta_0^+} u_{x2} = U\Big(\zeta_0(t)\Big), \tag{2.34}$$

where U is the local velocity at the interface. Then, using Eqs. (2.1) and (2.33), we can re-express Eq. (2.34) as

$$\lim_{x \to \zeta_0^-} \frac{dp_{01}}{dx} = - \left. \frac{12\mu_1 U(x)}{[h(x)]^2} \right|_{x=\zeta_0(t)}, \tag{2.35a}$$

$$\lim_{x \to \zeta_0^+} \frac{dp_{02}}{dx} = - \left. \frac{12\mu_2 U(x)}{[h(x)]^2} \right|_{x=\zeta_0(t)}. \tag{2.35b}$$

Applying the boundary condition from Eqs. (2.35) to the solution in Eq. (2.33), we have

$$p_{0j} = \frac{4\mu_j U\Big(\zeta_0(t)\Big) h_{in}}{\alpha [h\Big(\zeta_0(t)\Big)]^2} e^{-\frac{3\alpha}{h_{in}}\Big(x - \zeta_0(t)\Big)} \qquad (\alpha \ll 1). \tag{2.36}$$

Similarly, substituting Eqs. (2.8) and (2.10) into Eq. (2.5) and collecting terms at $\mathcal{O}(\epsilon)$, we have

$$\frac{d^2 g_j}{dx^2} + \frac{3\alpha}{h_{in}} \frac{dg_j}{dx} - k^2 g_j = 0, \qquad j = 1, 2 \qquad (\alpha \ll 1), \tag{2.37}$$

subject to

$$\lim_{x \to -\infty} g_1(x) = \lim_{x \to +\infty} g_2(x) = 0. \tag{2.38}$$

The solution to Eq. (2.37) is of the form $g_j = b_{j1} e^{m_1 x} + b_{j2} e^{m_2 x}$, where b_{j1} and b_{j2} are constants, and

$$m_{1,2} = -\frac{3\alpha}{2h_{in}} \left(1 \pm \sqrt{1 + \frac{4k^2 h_{in}^2}{9\alpha^2}} \right). \tag{2.39}$$

Therefore,

$$g_1(x) = b_{11} e^{m_1 x} + b_{12} e^{m_2 x}. \tag{2.40}$$

In a diverging cell, $\alpha > 0$, thus $m_1 < 0$ and $m_2 > 0$. From the boundary condition from Eq. (2.38), $b_{11} = 0$. In a converging cell, $\alpha < 0$, thus $m_1 > 0$, $m_2 < 0$ and $b_{12} = 0$. Hence,

$$g_1(x) = \begin{cases} b_{12} e^{m_2 x}, & \alpha > 0; \\ b_{11} e^{m_1 x}, & \alpha < 0. \end{cases} \tag{2.41}$$

Similarly,

$$g_2(x) = \begin{cases} b_{21} e^{m_1 x}, & \alpha > 0; \\ b_{22} e^{m_2 x}, & \alpha < 0. \end{cases} \tag{2.42}$$

Following [54], Eq. (2.41) and (2.42) can be combined into a single equation:

$$g_j = \hat{b}(j, \alpha) e^{\hat{m}(j,\alpha) x}, \tag{2.43}$$

where

$$\hat{m}(j, \alpha) = -\frac{3\alpha}{2h_{in}} \left(1 + (-1)^j \operatorname{sgn}(\alpha) \sqrt{1 + \frac{4k^2 h_{in}^2}{9\alpha^2}} \right), \tag{2.44}$$

where $\mathrm{sgn}(\alpha) = |\alpha|/\alpha$ for $\alpha \neq 0$ and vanishes otherwise. Therefore, Eq. (2.10) becomes

$$p_{1j} = \hat{b}(j,\alpha)e^{\hat{m}(j,\alpha)x+iky+\lambda(t)} \qquad (\alpha \ll 1). \tag{2.45}$$

Finally, substituting the leading-order pressure from Eq. (2.36) and the pressure-correction term from Eq. (2.45) into the definition of p_j from Eq. (2.8), leads to

$$p_j(x,y,t) = \frac{4\mu_j U\Big(\zeta_0(t)\Big)h_{in}}{\alpha[h\Big(\zeta_0(t)\Big)]^2}e^{-\frac{3\alpha}{h_{in}}\Big(x-\zeta_0(t)\Big)} + \epsilon\hat{b}(j,\alpha)e^{\hat{m}(j,\alpha)x+iky+\lambda(t)}. \tag{2.46}$$

Now, onto the boundary conditions for p_j at the interface. First, consider the kinematic condition, which states that interface velocity equals the fluid velocity at the interface:

$$\frac{\partial\zeta}{\partial t} = \boldsymbol{u}_j \cdot \hat{\boldsymbol{n}}|_{x=\zeta(y,t)}, \tag{2.47}$$

where $\boldsymbol{u}_j$ is given by Eq. (2.1). Letting $F = 0$, where $F(x,y) := x - \zeta(y,t)$, implicitly define the interface position, the unit surface normal $\hat{\boldsymbol{n}}$ can be defined, in Cartesian coordinates, as

$$\hat{\boldsymbol{n}} = \frac{\boldsymbol{\nabla}F}{\|\boldsymbol{\nabla}F\|} = \frac{1}{\|\boldsymbol{\nabla}F\|}\left(\frac{\partial F}{\partial x}, \frac{\partial F}{\partial y}\right) = \left[1 + \left(\frac{\partial\zeta}{\partial y}\right)^2\right]^{-1/2}\left(1, -\frac{\partial\zeta}{\partial y}\right). \tag{2.48}$$

Using a Taylor-series expansion for $|\partial\zeta/\partial y| \ll 1$, we have

$$\begin{aligned}\hat{\boldsymbol{n}} &= \left(1, -\frac{\partial\zeta}{\partial y}\right)\left[1 - \frac{1}{2}\left(\frac{\partial\zeta}{\partial y}\right)^2 + \mathcal{O}\left(\left(\frac{\partial\zeta}{\partial y}\right)^4\right)\right] \\ &\simeq \left(1, -\epsilon a e^{iky+\lambda(t)}ik\right),\end{aligned} \tag{2.49}$$

if only leading-order terms are kept.

Next, we combine Eq. (2.1) with p_j as given by Eq. (2.46) to obtain the Darcy velocities

$$\boldsymbol{u}_j = -\frac{[h\Big(\zeta(t)\Big)]^2}{12\mu_j}\left(\frac{\partial p_j}{\partial x}, \frac{\partial p_j}{\partial y}\right), \qquad j = 1, 2. \tag{2.50}$$

Combining Eqs. (2.49) and (2.50), we find the normal velocity to be

$$\boldsymbol{u}_j \cdot \hat{\boldsymbol{n}} = -\frac{[h\big(\zeta(t)\big)]^2}{12\mu_j}\left(\frac{\partial p_j}{\partial x} - \frac{\partial p_j}{\partial y}\frac{\partial \zeta}{\partial y}\right). \tag{2.51}$$

Therefore, each fluid's velocity normal to the interface is given by

$$\begin{aligned}\boldsymbol{u}_j \cdot \hat{\boldsymbol{n}}|_{x=\zeta(y,t)} &= U\big(\zeta_0(t)\big) \\ &+ \epsilon\left\{U\big(\zeta_0(t)\big)a\left(\frac{2\alpha}{h\big(\zeta_0(t)\big)} - \frac{3\alpha}{h_{in}}\right) - \frac{[h\big(\zeta_0(t)\big)]^2\hat{b}\hat{m}}{12\mu_j}e^{\hat{m}\zeta_0}\right\}e^{iky+\lambda(t)} + \mathcal{O}(\epsilon^2).\end{aligned} \tag{2.52}$$

Substituting Eq. (2.7) and Eq. (2.52) back into Eq. (2.47), we obtain

$$\hat{b}(j,\alpha) = -\frac{12\mu_j U\big(\zeta_0(t)\big)a}{\hat{m}[h\big(\zeta_0(t)\big)]^2}\left[\frac{\dot{\lambda}}{U\big(\zeta_0(t)\big)} + \alpha\left(\frac{3}{h_{in}} - \frac{2}{h\big(\zeta_0(t)\big)}\right)\right]e^{-\hat{m}\zeta_0(t)}. \tag{2.53}$$

For sufficiently large wave numbers compared to the gap gradient [54], i.e., $|kh_{in}/\alpha| \gg 1$, we can approximate the exponents, given in Eq. (2.44), as $\hat{m}(1,\alpha) \approx k$ and $\hat{m}(2,\alpha) \approx -k$. Then, the pressure at the interface becomes

$$\begin{aligned}p_j(x,y,t)|_{x=\zeta} &= \frac{4\mu_j U\big(\zeta_0(t)\big)h_{in}}{\alpha[h(\zeta_0(t))]^2} \\ &- \epsilon e^{iky+\lambda(t)}\frac{12U\big(\zeta_0(t)\big)a}{[h\big(\zeta_0(t)\big)]^2}\left\{\mu_j + \left[\frac{\dot{\lambda}}{U\big(\zeta_0(t)\big)} + \alpha\left(\frac{3}{h_{in}} - \frac{2}{h\big(\zeta_0(t)\big)}\right)\right]\frac{\mu_j}{\hat{m}(j,\alpha)}\right\} + \mathcal{O}(\epsilon^2).\end{aligned} \tag{2.54}$$

Thus, finally, the pressure difference across the interface takes the form of Eq. (2.11) above.

2.A.2 Weakly nonlinear analysis

If we keep the $\mathcal{O}(\epsilon^2)$ perturbation, the interface can be described as

$$\zeta = \zeta_0 + \epsilon a_1 e^{iky+\lambda_1(t)} + \epsilon^2 a_2 e^{2iky+\lambda_2(t)}, \tag{2.55}$$

then

$$\frac{\partial \zeta}{\partial t} = \epsilon a_1 e^{iky+\lambda_1(t)}\dot{\lambda}_1 + \epsilon^2 a_2 e^{2iky+\lambda_2(t)}\dot{\lambda}_2. \tag{2.56}$$

Similarly, the pressure at the interface is

$$p_j = p_{0j} + \epsilon p_{1j} + \epsilon^2 p_{2j}, \tag{2.57}$$

where $p_{1j} = g_{1j}(x)e^{iky+\lambda_1}$, $p_{2j} = g_{2j}(x)e^{2iky+\lambda_2}$. Substituting the pressure back into governing equation, we obtain the following three equations by respectively collecting the $\mathcal{O}(1)$ terms:

$$\frac{\partial^2 p_{0j}}{\partial x^2} + \frac{\partial^2 p_{0j}}{\partial y^2} + \frac{3\alpha}{h_{in}}\frac{\partial p_{0j}}{\partial x} = 0; \tag{2.58}$$

the $\mathcal{O}(\epsilon)$ terms:

$$\frac{\partial^2 g_{1j}}{\partial x^2} - k^2 g_{1j} + \frac{3\alpha}{h_{in}}\frac{\partial g_{1j}}{\partial x} = 0; \tag{2.59}$$

and the $\mathcal{O}(\epsilon^2)$ terms:

$$\frac{\partial^2 g_{2j}}{\partial x^2} - k^2 g_{2j} + \frac{3\alpha}{h_{in}}\frac{\partial g_{2j}}{\partial x} = 0. \tag{2.60}$$

For the $\mathcal{O}(1)$ terms, the solution is the same with the linear analysis:

$$p_{0j} = \frac{4\mu_j U h_{in}}{\alpha[h\Big(\zeta_0(t)\Big)]^2} e^{-\frac{3\alpha}{h_{in}}\Big(x-\zeta_0(t)\Big)}, \tag{2.61}$$

Similarly,

$$p_{1j} = \hat{b}_1(j,\alpha)e^{\hat{m}_1(j,\alpha)x+iky+\lambda_1}, \tag{2.62}$$

$$p_{2j} = \hat{b}_2(j,\alpha)e^{\hat{m}_2(j,\alpha)x+2iky+\lambda_2}. \tag{2.63}$$

Therefore the total pressure can be written as

$$p_j = \frac{4\mu_j U h_{in}}{\alpha[h\Big(\zeta_0(t)\Big)]^2} e^{-\frac{3\alpha}{h_{in}}\Big(x-\zeta_0(t)\Big)} + \epsilon\hat{b}_1(j,\alpha)e^{\hat{m}_1(j,\alpha)x+iky+\lambda_1} + \epsilon^2\hat{b}_2(j,\alpha)e^{\hat{m}_2(j,\alpha)x+2iky+\lambda_2}. \tag{2.64}$$

Then we have the partial differential expression of the pressure

$$
\begin{aligned}
\left.\frac{\partial p_j}{\partial x}\right|_{x=\zeta} &= \left.\frac{\partial p_{0j}}{\partial x}\right|_{x=\zeta} + \epsilon \left.\frac{\partial p_{1j}}{\partial x}\right|_{x=\zeta} + \epsilon^2 \left.\frac{\partial p_{2j}}{\partial x}\right|_{x=\zeta} \\
&= -\frac{12\mu_j U}{[h\Big(\zeta_0(t)\Big)]^2} + \epsilon \left(\frac{12\mu_j U}{[h\Big(\zeta_0(t)\Big)]^2} \frac{3\alpha}{h_{in}} a_1 e^{iky+\lambda_1} + \hat{b}_1(j,\alpha)\hat{m}_1(j,\alpha) e^{\hat{m}_1(j,\alpha)\zeta_0 + iky + \lambda_1} \right) \\
&\quad + \epsilon^2 \Bigg[\frac{12\mu_j U}{[h\Big(\zeta_0(t)\Big)]^2} \left(\frac{3\alpha}{h_{in}} a_2 e^{2iky+\lambda_2} - \frac{9\alpha^2}{2h_{in}^2} a_1^2 e^{2iky+2\lambda_1} \right) \\
&\quad + a_1 \hat{b}_1(j,\alpha)\hat{m}_1(j,\alpha)^2 e^{\hat{m}_1(j,\alpha)\zeta_0 + 2iky + 2\lambda_1} + \hat{b}_2(j,\alpha)\hat{m}_2(j,\alpha) e^{\hat{m}_2(j,\alpha)\zeta_0 + 2iky + \lambda_2} \Bigg] \\
&\quad + \mathcal{O}(\epsilon^3).
\end{aligned} \tag{2.65}
$$

Similarly, the partial differential expression of the pressure over y are calculated as:

$$
\begin{aligned}
\left.\frac{\partial p_j}{\partial y}\right|_{x=\zeta} &= \left.\frac{\partial p_{0j}}{\partial y}\right|_{x=\zeta} + \epsilon \left.\frac{\partial p_{1j}}{\partial y}\right|_{x=\zeta} + \epsilon^2 \left.\frac{\partial p_{2j}}{\partial y}\right|_{x=\zeta} \\
&= \epsilon i k \hat{b}_1(j,\alpha) e^{\hat{m}_1(j,\alpha)\zeta_0 + iky + \lambda_1} \\
&\quad + \epsilon^2 i k \Big(a_1 \hat{b}_1(j,\alpha)\hat{m}_1(j,\alpha) e^{\hat{m}_1(j,\alpha)\zeta_0 + 2iky + 2\lambda_1} \\
&\quad + \hat{b}_2(j,\alpha) e^{\hat{m}_2(j,\alpha)\zeta_0 + 2iky + \lambda_2} \Big).
\end{aligned} \tag{2.66}
$$

Therefore,

$$
\begin{aligned}
\left.\frac{\partial p_j}{\partial x} - \frac{\partial p_j}{\partial y}\frac{\partial \zeta}{\partial y}\right|_{x=\zeta} &= -\frac{12\mu_j U}{[h\Big(\zeta_0(t)\Big)]^2} + \epsilon \Bigg[\frac{12\mu_j U}{[h\Big(\zeta_0(t)\Big)]^2} \frac{3\alpha}{h_{in}} a_1 e^{iky+\lambda_1} \\
&\quad + \hat{b}_1(j,\alpha)\hat{m}_1(j,\alpha) e^{\hat{m}_1(j,\alpha)\zeta_0 + iky + \lambda_1} \Bigg] \\
&\quad + \epsilon^2 \Bigg[\frac{12\mu_j U}{[h\Big(\zeta_0(t)\Big)]^2} \left(\frac{3\alpha}{h_{in}} a_2 e^{2iky+\lambda_2} - \frac{9\alpha^2}{2h_{in}^2} a_1^2 e^{2iky+2\lambda_1} \right) \\
&\quad + a_1 \hat{b}_1(j,\alpha)\hat{m}_1(j,\alpha)^2 e^{\hat{m}_1(j,\alpha)\zeta_0 + 2iky + 2\lambda_1} \\
&\quad + \hat{b}_2(j,\alpha)\hat{m}_2(j,\alpha) e^{\hat{m}_2(j,\alpha)\zeta_0 + 2iky + \lambda_2} \\
&\quad + k^2 a_1 \hat{b}_1(j,\alpha) e^{\hat{m}_1(j,\alpha)\zeta_0 + 2iky + 2\lambda_1} \Bigg] + \mathcal{O}(\epsilon^3).
\end{aligned} \tag{2.67}
$$

Keeping the $\mathcal{O}(\epsilon^2)$ terms in Eq. (2.49), we have

$$\begin{aligned}\boldsymbol{u}_j \cdot \boldsymbol{n} &= -\frac{[h\big(\zeta_0(t)\big)]^2}{12\mu_j}\left(\frac{\partial p_j}{\partial x}, \frac{\partial p_j}{\partial y}\right)\cdot\left(1, -\frac{\partial \zeta}{\partial y}\right)\left[1-\frac{1}{2}\left(\frac{\partial \zeta}{\partial y}\right)^2\right] \\ &= -\frac{[h\big(\zeta_0(t)\big)]^2}{12\mu_j}\left(1+\frac{1}{2}\epsilon^2 k^2 a_1^2 e^{2iky+2\lambda_1}\right)\left(\frac{\partial p_j}{\partial x}-\frac{\partial p_j}{\partial y}\frac{\partial \zeta}{\partial y}\right).\end{aligned} \tag{2.68}$$

Plugging Eq. (2.67) into Eq. (2.68), we find that in Eq. (2.68), to $\mathcal{O}(1)$,

$$\frac{[h\big(\zeta_0(t)\big)]^2}{12\mu_j}\frac{12\mu_j U}{[h\big(\zeta_0(t)\big)]^2} = U, \tag{2.69}$$

and to $\mathcal{O}(\epsilon)$,

$$-\frac{3\alpha U}{h_{in}} a_1 e^{iky+\lambda_1} - \frac{[h\big(\zeta_0(t)\big)]^2}{12\mu_j}\hat{b}_1(j,\alpha)\hat{m}_1(j,\alpha)e^{\hat{m}_1(j,\alpha)\zeta_0+iky+\lambda_1}, \tag{2.70}$$

and to $\mathcal{O}(\epsilon^2)$,

$$\begin{aligned}-\frac{3\alpha U}{h_{in}} a_2 e^{2iky+\lambda_2} + \frac{9\alpha^2 U}{2h_{in}^2} a_1^2 e^{2iky+2\lambda_1} \\ - \frac{[h\big(\zeta_0(t)\big)]^2}{12\mu_j}[a_1\hat{b}_1(j,\alpha)\hat{m}_1(j,\alpha)^2 e^{\hat{m}_1(j,\alpha)\zeta_0+2iky+2\lambda_1} \\ + \hat{b}_2(j,\alpha)\hat{m}_2(j,\alpha)e^{\hat{m}_2(j,\alpha)\zeta_0+2iky+\lambda_2} + k^2 a_1\hat{b}_1(j,\alpha)e^{\hat{m}_1(j,\alpha)\zeta_0+2iky+2\lambda_1}] \\ + \frac{1}{2}Uk^2 a_1^2 e^{2iky+2\lambda_1}.\end{aligned} \tag{2.71}$$

Matching Eqs. (2.70) and (2.71) with the $\mathcal{O}(\epsilon)$ and $\mathcal{O}(\epsilon^2)$ terms in Eq. (2.56), we obtain two equations related to the linear and weakly nonlinear growth rate, i.e., $\dot{\lambda}_1$ and $\dot{\lambda}_2$, respectively:

$$a_1 e^{iky+\lambda_1(t)}\dot{\lambda}_1 = -\frac{3\alpha U}{h_{in}} a_1 e^{iky+\lambda_1} - \frac{[h\big(\zeta_0(t)\big)]^2}{12\mu_j}\hat{b}_1(j,\alpha)\hat{m}_1(j,\alpha)e^{\hat{m}_1(j,\alpha)\zeta_0+iky+\lambda_1}, \tag{2.72}$$

which reduces to

$$\hat{b}_1(j,\alpha)\hat{m}_1(j,\alpha)e^{\hat{m}_1(j,\alpha)\zeta_0} = -\frac{12\mu_j U a_1}{[h\Big(\zeta_0(t)\Big)]^2}\left(\frac{\dot{\lambda}_1}{U}+\frac{3\alpha}{h_{in}}\right), \tag{2.73}$$

and

$$\begin{aligned} a_2 e^{2iky+\lambda_2(t)}\dot{\lambda}_2 = &-\frac{3\alpha U}{h_{in}}a_2 e^{2iky+\lambda_2} + \frac{9\alpha^2 U}{2h_{in}^2}a_1^2 e^{2iky+2\lambda_1} \\ &- \frac{[h\Big(\zeta_0(t)\Big)]^2}{12\mu_j}[a_1\hat{b}_1(j,\alpha)\hat{m}_1(j,\alpha)^2 e^{\hat{m}_1(j,\alpha)\zeta_0+2iky+2\lambda_1} \\ &+ \hat{b}_2(j,\alpha)\hat{m}_2(j,\alpha)e^{\hat{m}_2(j,\alpha)\zeta_0+2iky+\lambda_2} \\ &+ k^2 a_1\hat{b}_1(j,\alpha)e^{\hat{m}_1(j,\alpha)\zeta_0+2iky+2\lambda_1}] + \frac{1}{2}Uk^2 a_1^2 e^{2iky+2\lambda_1}, \end{aligned} \tag{2.74}$$

which reduces to

$$\begin{aligned} \hat{b}_2(j,\alpha)\hat{m}_2(j,\alpha)e^{\hat{m}_2(j,\alpha)\zeta_0+\lambda_2} = &\frac{12\mu_j U}{[h\Big(\zeta_0(t)\Big)]^2}\left[-\left(\frac{a_2\dot{\lambda}_2}{U}+\frac{3\alpha a_2}{h_{in}}\right)e^{\lambda_2} + \left(\frac{9\alpha^2}{2h_{in}^2}+\frac{1}{2}k^2\right)a_1^2 e^{2\lambda_1}\right] \\ &+ \frac{12\mu_j U a_1^2}{[h\Big(\zeta_0(t)\Big)]^2}\left(\frac{\dot{\lambda}_1}{U}+\frac{3\alpha}{h_{in}}\right)\left(\frac{k^2}{\hat{m}_1}+\hat{m}_1\right)e^{2\lambda_1}. \end{aligned} \tag{2.75}$$

Substituting Eqs. (2.73) and (2.75) back into the pressure equation Eq. (2.64), we can rewrite it as

$$\begin{aligned} p_j|_{x=\zeta} = &\frac{4\mu_j U h_{in}}{\alpha[h\Big(\zeta_0(t)\Big)]^2} - \epsilon\left[\frac{12\mu_j U a_1 e^{iky+\lambda_1}}{[h\Big(\zeta_0(t)\Big)]^2} + \frac{12\mu_j U a_1 e^{iky+\lambda_1}}{\hat{m}_1[h\Big(\zeta_0(t)\Big)]^2}\left(\frac{\dot{\lambda}_1}{U}+\frac{3\alpha}{h_{in}}\right)\right] \\ &+ \epsilon^2\Bigg\{-\frac{12U\mu_j a_2 e^{2iky+\lambda_2}}{[h\Big(\zeta_0(t)\Big)]^2} + \frac{9\alpha^2}{2h_{in}^2}a_1^2 e^{2iky+2\lambda_1} - \frac{12\mu U a_1^2 e^{2iky+2\lambda_1}}{[h\Big(\zeta_0(t)\Big)]^2}\left(\frac{\dot{\lambda}_1}{U}+\frac{3\alpha}{h_{in}}\right) \\ &+ \frac{12\mu_j U}{\hat{m}_2(j,\alpha)[h\Big(\zeta_0(t)\Big)]^2}\left[-\left(\frac{a_2\dot{\lambda}_2}{U}+\frac{3\alpha a_2}{h_{in}}\right)e^{2iky+\lambda_2} + \left(\frac{9\alpha^2}{2h_{in}^2}+\frac{1}{2}k^2\right)a_1^2 e^{2iky+2\lambda_1}\right] \\ &+ \frac{12\mu_j U a_1^2}{\hat{m}_2(j,\alpha)[h\Big(\zeta_0(t)\Big)]^2}\left(\frac{\dot{\lambda}_1}{U}+\frac{3\alpha}{h_{in}}\right)\left(\frac{k^2}{\hat{m}_1}+\hat{m}_1\right)e^{2iky+2\lambda_1}\Bigg\} + \mathcal{O}(\epsilon^3). \end{aligned} \tag{2.76}$$

Following our previous analysis in the linear stage, it is easy to conclude that $\hat{m}_1(1,\alpha) = \hat{m}_2(1,\alpha) = k$, and $\hat{m}_1(2,\alpha) = \hat{m}_2(2,\alpha) = -k$, in which the subscript represents the first order or second order perturbation.

Therefore, the pressure jump at the interface is written as

$$
\begin{aligned}
p_1 - p_2|_{x=\zeta} &= \frac{4Uh_{in}}{\alpha[h\big(\zeta_0(t)\big)]^2}(\mu_1-\mu_2) - \epsilon\frac{12Ua_1e^{iky+\lambda_1}}{[h\big(\zeta_0(t)\big)]^2}\Bigg[(\mu_1-\mu_2) \\
&+ \left(\frac{\dot{\lambda}_1}{U}+\frac{3\alpha}{h_{in}}\right)\left(\frac{\mu_1}{\hat{m}_{11}}-\frac{\mu_2}{\hat{m}_{12}}\right)\Bigg] + \epsilon^2\Bigg\{\frac{12U(\mu_1-\mu_2)}{[h\big(\zeta_0(t)\big)]^2}\Bigg[-a_2e^{2iky+\lambda_2} \\
&- a_1^2e^{2iky+2\lambda_1}\left(\frac{\dot{\lambda}_1}{U}+\frac{3\alpha}{h_{in}}\right)\Bigg] \\
&+ \frac{12a_2U}{[h\big(\zeta_0(t)\big)]^2}\left(\frac{\mu_1}{\hat{m}_{11}}-\frac{\mu_2}{\hat{m}_{12}}\right)\Bigg[-\left(\frac{\dot{\lambda}_2}{U}+\frac{3\alpha}{h_{in}}\right)e^{2iky+\lambda_2} \\
&+ \left(\frac{9\alpha^2}{2h_{in}^2}+\frac{1}{2}k^2\right)a_1^2e^{2iky+2\lambda_1}\Bigg] \\
&+ \frac{12Ua_1^2k^2}{[h\big(\zeta_0(t)\big)]^2}\left(\frac{\dot{\lambda}_1}{U}+\frac{3\alpha}{h_{in}}\right)e^{2iky+2\lambda_1}\left(\frac{\mu_1}{\hat{m}_{11}\hat{m}_{21}}-\frac{\mu_2}{\hat{m}_{12}\hat{m}_{22}}\right) \\
&+ \frac{12Ua_1^2}{[h\big(\zeta_0(t)\big)]^2}\left(\frac{\dot{\lambda}_1}{U}+\frac{3\alpha}{h_{in}}\right)\left(\frac{\mu_1\hat{m}_{11}}{\hat{m}_{21}}-\frac{\mu_2\hat{m}_{12}}{\hat{m}_{22}}\right)e^{2iky+2\lambda_1}\Bigg\} + \mathcal{O}(\epsilon^3) \\
&= \frac{Ca\gamma h_{in}}{3\alpha[h\big(\zeta_0(t)\big)]^2}(M-1) - \epsilon\frac{Ca\gamma a_1e^{iky+\lambda_1}}{[h\big(\zeta_0(t)\big)]^2}\left[(M-1)+\left(\frac{\dot{\lambda}_1}{U}+\frac{3\alpha}{h_{in}}\right)\frac{M+1}{k}\right] \\
&+ \epsilon^2e^{2iky}\Bigg\{-\frac{Caa_2\gamma(M-1)e^{\lambda_2}}{[h\big(\zeta_0(t)\big)]^2} + \frac{Ca\gamma a_2}{k[h\big(\zeta_0(t)\big)]^2}(M+1)\Bigg[-\left(\frac{\dot{\lambda}_2}{U}+\frac{3\alpha}{h_{in}}\right)e^{\lambda_2} \\
&+ \left(\frac{9\alpha^2}{2h_{in}^2}+\frac{1}{2}k^2\right)a_1^2e^{2\lambda_1}\Bigg] + \frac{Ca\gamma a_1^2}{[h\big(\zeta_0(t)\big)]^2}\left(\frac{\dot{\lambda}_1}{U}+\frac{3\alpha}{h_{in}}\right)(M-1)e^{2\lambda_1}\Bigg\} + \mathcal{O}(\epsilon^3).
\end{aligned}
\tag{2.77}
$$

On the other hand, the capillary pressure jump given by Young-Laplace equation is

$$
p_1 - p_2 = \gamma\left\{\frac{2\cos\theta_c}{h[\zeta(y,t)]} + \kappa\right\}, \tag{2.78}
$$

where

$$\begin{aligned}\frac{1}{h(\zeta)} &= \frac{1}{h(\zeta_0)+\alpha(\epsilon a_1 e^{iky+\lambda_1}+\epsilon^2 a_2 e^{2iky+\lambda_2})} \\ &= \frac{1}{h(\zeta_0)} - \epsilon\frac{\alpha a_1 e^{iky+\lambda_1}}{[h(\zeta_0)]^2} + \epsilon^2\left(-\frac{\alpha a_2 e^{2iky+\lambda_2}}{[h(\zeta_0)]^2} + \frac{\alpha^2 a_1^2 e^{2iky+2\lambda_1}}{[h(\zeta_0)]^3}\right) + \mathcal{O}(\epsilon^3),\end{aligned} \tag{2.79}$$

and

$$\begin{aligned}\kappa &= -\frac{\partial^2\zeta/\partial y^2}{[1+(\partial\zeta/\partial y)^2]^{3/2}} \\ &= k^2\epsilon a_1 e^{iky+\lambda_1} + \epsilon^2 a_2 k^2 e^{2iky+\lambda_2} + \mathcal{O}(\epsilon^3).\end{aligned} \tag{2.80}$$

Thus Eq. (2.78) is rewritten as

$$\begin{aligned}p_1 - p_2 = &\frac{2\gamma\cos\theta_c}{h(\zeta_0)} + \epsilon\gamma\left(-\frac{2\cos\theta_c\alpha a_1 e^{iky+\lambda_1}}{[h(\zeta_0)]^2} + k^2 a_1 e^{iky+\lambda_1}\right) \\ &+ \epsilon^2\gamma(2\cos\theta_c\left(-\frac{\alpha a_2 e^{2iky+\lambda_2}}{[h(\zeta_0)]^2} + \frac{\alpha^2 a_1^2 e^{2iky+2\lambda_1}}{[h(\zeta_0)]^3}\right) \\ &+ a_2 k^2 e^{2iky+\lambda_2}) + \mathcal{O}(\epsilon^3).\end{aligned} \tag{2.81}$$

Collecting the $\mathcal{O}(\epsilon)$ terms in Eqs. (2.77) and (2.81), we obtain

$$\begin{aligned}&-\frac{Ca\gamma a_1 e^{iky+\lambda_1}}{[h\big(\zeta_0(t)\big)]^2}\left[(M-1)+\left(\frac{\dot\lambda_1}{U}+\frac{3\alpha}{h_{in}}\right)\frac{M+1}{k}\right] \\ &\qquad = \gamma\left(-\frac{2\cos\theta_c\alpha a_1 e^{iky+\lambda_1}}{[h(\zeta_0)]^2} + k^2 a_1 e^{iky+\lambda_1}\right),\end{aligned} \tag{2.82}$$

reducing to

$$(1+M)\left(\frac{\dot\lambda_1}{U}+\frac{3\alpha}{h_{in}}\right) = \left(1-M+\frac{2\alpha\cos\theta_c}{Ca}\right)k - \frac{k^3[h\big(\zeta_0(t)\big)]^2}{Ca}, \tag{2.83}$$

which is exactly the same with the linear analysis in the previous section.

Similarly, collecting the $\mathcal{O}(\epsilon^2)$ terms in Eqs. (2.77) and (2.81), we obtain

$$-\frac{Caa_2\gamma(M-1)e^{\lambda_2}}{[h\big(\zeta_0(t)\big)]^2} + \frac{Ca\gamma a_2(M+1)}{k[h\big(\zeta_0(t)\big)]^2}\left[-\left(\frac{\dot\lambda_2}{U}+\frac{3\alpha}{h_{in}}\right)e^{\lambda_2} + \left(\frac{9\alpha^2}{2h_{in}^2}+\frac{1}{2}k^2\right)a_1^2 e^{2\lambda_1}\right]$$

$$+\frac{Ca\gamma a_1^2}{[h\Big(\zeta_0(t)\Big)]^2}\left(\frac{\dot{\lambda}_1}{U}+\frac{3\alpha}{h_{in}}\right)(M-1)e^{2\lambda_1}$$
$$=\gamma\left[2\cos\theta_c\left(-\frac{\alpha a_2 e^{\lambda_2}}{[h(\zeta_0)]^2}+\frac{\alpha^2 a_1^2 e^{2\lambda_1}}{[h(\zeta_0)]^3}\right)+a_2k^2e^{\lambda_2}\right] \quad (2.84)$$

which reduces to

$$\begin{aligned}(M+1)\left(\frac{\dot{\lambda}_2}{U}+\frac{3\alpha}{h_{in}}\right) &= k(1-M)+\frac{ka_1^2(M-1)}{a_2}\left(\frac{\dot{\lambda}_1}{U}+\frac{3\alpha}{h_{in}}\right)e^{2\lambda_1-\lambda_2}\\ &+(M+1)\left(\frac{9\alpha^2}{2h_{in}^2}+\frac{1}{2}k^2\right)a_1^2e^{2\lambda_1-\lambda_2}\\ &-\frac{2\cos\theta_c k}{Ca}\left(-\alpha+\frac{\alpha^2a_1^2e^{2\lambda_1-\lambda_2}}{h(\zeta_0)a_2}\right)-\frac{k^3[h\Big(\zeta_0(t)\Big)]^2}{Ca},\end{aligned} \quad (2.85)$$

which is the newly derived weakly nonlinear growth rate $\dot{\lambda}_2$ equation.

3. THE HYDRAULIC CONDUCTIVITY OF A SHAPED FRACTURE WITH PERMEABLE WALLS

SUMMARY

We investigate the flow-wise variation of the hydraulic conductivity inside a non-uniformly shaped fracture with permeable walls. Using lubrication theory for viscous flows, in conjunction with the Beavers–Joseph–Saffman boundary condition at the permeable walls, we obtain an analytical expression for the velocity profile, conductivity, and wall permeation velocity. These predictions highlight the effects of geometric variation (through the local slope of the aperture's flow-wise variation), the permeability of the walls (through a dimensionless slip coefficient), and the effect of flow inertia (through a Reynolds number). The theory is validated against an OpenFOAM® solver for the Navier–Stokes equations subject to a tensorial slip boundary condition, showing good agreement. The mathematical results have implications on system-level (multiscale) modeling of hydraulically fractured reservoirs, in which the Darcy conductivity of each non-uniform passage must be accurately accounted for, throughout the fractured porous rock.

The material in this chapter was published in [D. Lu, F. Municchi, and I. C. Christov, "The hydraulic conductivity of a shaped fracture with permeable walls," *Mech. Res. Commun.*, vol. 111, 103650, 2021] [176].

3.1 Problem statement

Currently, the theory of fracture conductivity is based on many assumptions: smooth, impermeable walls with a constant aperture and span. However, both naturally and fractured formations violates the assumptions. The bounding surfaces of a fracture are the porous rock formations themselves, therefore they should not be idealized as impermeable plates [94]. Generally, the walls of fractures are not parallel [89], in part due to the flow-wise deformation of the fracture due to large injection pressures [90], requiring corrections to Darcy's laws arise via a modified conductivity and transmissivity models [91]–[93]. So far, a theory for the conductivity of variable-aperture fractures with porous walls (the most common case in the subsurface) is lacking.

In this chapter, we aim to fill this knowledge gap by deriving a theory for the conductivity of variable-aperture fractures with porous walls (the most common case in the subsurface). We take the perturbative mathematical approach, based on the notion of slow variation in fluid mechanics [177], to calculate the conductivity of a shaped fracture with permeable walls (see Sect. 3.2). Importantly, in Sect. 3.3, we also validate our proposed model for $\mathcal{K}$ against direct numerical simulations using a custom solver built on OpenFOAM® [159], [178]. We provide an implementation of the *semi-implicit method for pressure-linked equations* (SIMPLE) algorithm (see, e.g., [160, Ch. 15]) for the Navier–Stokes equations subject to the tensorial form of the Beavers–Joseph–Saffman (BJS) boundary condition.

3.2 Mathematical analysis

3.2.1 Governing equations

The flow geometry and notation are shown in Fig. 1.5. An incompressible Newtonian fluid of density ρ and dynamic viscosity μ fills the gap. The fracture is long and thin, which justifies taking $h(x)$ to be a linear function [179]. Alternatively, one is allowed to substitute $\alpha = \alpha(x)$ in the results below if $dh/dx \neq const.$, as long as $\max_x \alpha(x)$ satisfies the original smallness assumption [86], [92]. Let U_0 be the average inlet velocity at the inlet ($x = 0$), which serves as the scale for the horizontal velocity $u(x, z)$ in the fracture. The flow is assumed to be 2D,

i.e., the fracture is infinite in the transverse y-direction. Then, conservation of mass requires that the scale for the vertical velocity $v(x,z)$ be $V_0 = U_0 h_0/L = \epsilon U_0$ [104, Sect. 4.9].

Now, we define the dimensionless (starred) variables

$$x^* = x/L, \quad z^* = z/h_0, \quad h^*(x^*) = h(x)/h_0,$$
$$u^*(x^*,z^*) = u(x,z)/U_0, \quad v^*(x^*,z^*) = v(x,z)/V_0,$$
$$p^*(x^*,z^*) = \epsilon h_0 p(x,z)/(\mu U_0), \quad \mathcal{K}^*(x^*) = \mathcal{K}(x)/h_0^2, \tag{3.1}$$

where $Re = \rho U_0 h_0/\mu$ is the Reynolds number and $\tilde{Re} = \epsilon Re$ is a reduced Reynolds number [86]. Then, the dimensionless conservation of mass and momentum equations are

$$\frac{\partial u^*}{\partial x^*} + \frac{\partial v^*}{\partial z^*} = 0, \tag{3.2a}$$
$$\tilde{Re}\left(u^*\frac{\partial u^*}{\partial x^*} + v^*\frac{\partial u^*}{\partial z^*}\right) = -\frac{\partial p^*}{\partial x^*} + \epsilon^2\frac{\partial^2 u^*}{\partial x^{*2}} + \frac{\partial^2 u^*}{\partial z^{*2}}, \tag{3.2b}$$
$$\epsilon^2\tilde{Re}\left(u^*\frac{\partial v^*}{\partial x^*} + v^*\frac{\partial v^*}{\partial z^*}\right) = -\frac{\partial p^*}{\partial z^*} + \epsilon^4\frac{\partial^2 v^*}{\partial x^{*2}} + \epsilon^2\frac{\partial^2 v^*}{\partial z^{*2}}, \tag{3.2c}$$

subject to the following boundary conditions (BCs):

$$\text{symmetry at } z^* = 0: \qquad \frac{\partial u^*}{\partial z^*} = 0 \ \text{ and } \ v^* = 0; \tag{3.3a}$$
$$\text{partial slip at } z^* = h^*: \qquad u^* = -\phi\frac{\partial u^*}{\partial z^*}, \tag{3.3b}$$

where ϕ is the slip coefficient, and $h^* = h^*(x^*) = 1 + \alpha x^*/\epsilon$. Observe that, here, we can introduce $\delta = \alpha/\epsilon = [h(L) - h(0)]/h_0 = \Delta h/h_0$, which is the percent change of $h(x)$ over the typical fracture variation length L, so that $h^*(x^*) = 1 + \delta x^*$. The assumption of *slow variation* dictates that $\delta \ll 1$, while the assumption of *lubrication* (small aspect ration) dictates that $\epsilon = h_0/L \ll 1$ (see also [86], [104]). These two assumptions are independent and lead to $\alpha = \epsilon\delta \lll 1$, which is typical of fractures, as discussed in Sect. 1.1.

The BC in Eq. (3.3a) is the centerline symmetry condition, while the BC in Eq. (3.3b) comes from the BJS partial slip BC [105], [107], [108], [180], [181] on the permeable wall (see Sect. 3.A for details). Physically, the BJS BC enforces a shear stress balance along the fluid–

porous solid interface by relating the tangential velocity component to the normal component of the velocity gradient via the slip coefficient ϕ (which is an empirically-measurable constant set by the permeability of the surrounding medium and its pore geometry, recall Sect. 1.1). Importantly, the BJS BC allows us to solve for the flow in the fracture without solving for the flow in the surround porous medium.

3.2.2 Perturbation solution for the velocity profile

Following the standard procedure of a regular perturbation expansion [182], the velocity field is expanded as $u^* = u_0^* + \tilde{Re}\, u_1^* + \cdots$ and $v^* = v_0^* + \tilde{Re}\, v_1^* + \cdots$ ($\tilde{Re} \ll 1$). Then, we find the horizontal velocity at the leading order (see Sect. 3.A.1 for details):

$$u_0^*(x^*, z^*) = \left(\frac{h^{*2} - z^{*2}}{2} + \phi h^*\right)\left(-\frac{dp^*}{dx^*}\right). \tag{3.4}$$

Since the flow is in the direction of positive x^*, $dp^*/dx^* < 0$. Then, the leading-order depth-averaged velocity is

$$\begin{aligned}\langle u_0^* \rangle(x^*) &= \frac{1}{h^*(x^*)} \int_0^{h^*(x^*)} u_0^*(x^*, z^*)\, dz^* \\ &= \frac{3\phi h^* + h^{*2}}{3}\left(-\frac{dp^*}{dx^*}\right).\end{aligned} \tag{3.5}$$

And, the vertical velocity at the leading order is

$$v_0^*(x^*, z^*) = (h^* + \phi)\frac{dh^*}{dx^*} z^* \frac{dp^*}{dx^*} - \left(\frac{z^{*2}}{6} - \frac{h^{*2}}{2} - \phi h^*\right) z^* \frac{d^2 p^*}{dx^{*2}}. \tag{3.6}$$

At the next order in $\tilde{Re}$, we find the depth-averaged velocity's correction:

$$\begin{aligned}\langle u_1^* \rangle(x^*) = \left(\frac{3}{35}h^{*2} + \frac{\phi}{3}h^* + \frac{\phi^2}{3}\right) h^{*4} \left(-\frac{dp^*}{dx^*}\right) \frac{d^2 p^*}{dx^{*2}} \\ - \left(\frac{h^*}{5} + \frac{\phi}{3}\right) h^{*3}(h^* + \phi) \frac{1}{\epsilon}\frac{dh^*}{dx^*}\left(\frac{dp^*}{dx^*}\right)^2.\end{aligned} \tag{3.7}$$

For the present purposes, it is not necessary to write out u_1^* and v_1^* but they can be calculated (see Sect. 3.A.1).

3.2.3 Equivalent Darcy's law and the hydraulic conductivity

To obtain the conductivity $\mathcal{K}$ in a shaped fracture with porous walls, we must put the flow field thus obtained into the form of a Darcy-like law, i.e., $\langle u^* \rangle \propto -dp^*/dx^*$, with the proportionality factor being the sought-after result. To this end, combining Eqs. (3.5) and (3.7) we obtain the "full" depth-average horizontal velocity up to $\mathcal{O}(\tilde{Re})$: $\langle u^* \rangle = \langle u_0^* \rangle + \tilde{Re}\langle u_1^* \rangle$. However, at this point, the pressure distribution $p^*(x^*)$ is still *unknown*. To close the problem, we need another constraint. Mohais, Xu, Dowd, *et al.* [14] provided one solution by assuming a *constant* permeation velocity v_w in a parallel fracture ($\alpha = dh^*/dx^* = 0$, $h^* = 1$), i.e., $v_0|_{z=\pm h_0} = \pm v_w$. We could apply this BC here too (see Sect. 3.A.1), however, as discussed in Sect. 1.1, the assumption of a constant v_w is not suitable for shaped fractures, due to the flow-wise x^*-variation of the aperture.

Instead, to close the problem, we impose the full flux onto the leading-order depth-averaged velocity, i.e., we set $\langle u_0^* \rangle = 1$. We impose this condition because, as discussed in Sect. 1.1, the representative fracture region of interest is away from the crack tip, and thus the flow is not leak-off dominated, following Refs. [14], [92], [112], [183] but in contrast to Refs. [3], [4], [184] (or, e.g., Refs. [185], [186] in the context of filtration). Thus, v_w^* will *not* be constant and will be self-consistently determined as a function of x^*. Another modeling approach is to set the wall-normal velocity via the local pressure, as in filtration problems [185], [186], however this approach is beyond the scope of the present study focused on porous media flows.

Applying the constraint $\langle u_0^* \rangle = 1$ to Eq. (3.5), we compute dp^*/dx^* and d^2p^*/dx^{*2} (see Sect. 3.A.1). Substituting the latter results into Eq. (3.7) and putting it all together,

$$\begin{aligned} \langle u^* \rangle &= -\mathcal{K}^* \frac{dp^*}{dx^*}, \\ \mathcal{K}^*(x^*) &= \left[\frac{3\phi h^* + h^{*2}}{3} - \tilde{Re} \frac{h^{*3}(28\phi^2 + 22\phi h^* + 3h^{*2})\delta}{35(3\phi + h^*)^2} \right], \end{aligned} \tag{3.8}$$

which is already in the form of Darcy's law. Finally, Eq. (3.8) can be put in dimensional form:

$$\langle u \rangle = -\frac{\mathcal{K}}{\mu}\frac{\partial p}{\partial x}, \qquad \mathcal{K} = \frac{h_0^2}{3}C, \tag{3.9}$$

where we have defined the dimensionless function

$$\begin{aligned} C(x) &= \left[3\phi h^* + h^{*2} - 3\tilde{Re}\frac{h^{*3}(28\phi^2 + 22\phi h^* + 3h^{*2})\delta}{35(3\phi + h^*)^2}\right] \\ &= \underbrace{1}_{\text{(I)}} + \underbrace{3\phi}_{\text{(II)}} + \underbrace{\left[(2+3\phi)\frac{x}{L} - 3\tilde{Re}\,\frac{3 + 22\phi + 28\phi^2}{35(3\phi+1)^2}\right]\delta}_{\text{(III)}} \\ &\quad + \mathcal{O}\left(\delta^2\right) \end{aligned} \tag{3.10}$$

to represent the "correction" to the hydraulic conductivity of the fracture. As discussed in Sect. 1.1, typical fractures are long and shallow ($\epsilon \ll 1$), and the slopes of the wall variation are even smaller ($\alpha = \epsilon\delta \lll 1$), thus we expanded a number of terms in Eq. (3.10) into Taylor series and kept only terms up to $\mathcal{O}(\delta)$ to highlight the key physical effects of shape variation in a fracture with permeable walls.

The function C accounts for wall permeation through the BJS slip coefficient $\phi = \sqrt{k_w}/(bh_0)$, the shape of the fracture through the slope $\alpha = dh/dx$ and aspect ratio $\epsilon = h_0/L$, and weak inertia through the reduced Reynolds number $\tilde{Re} = \rho U_0 h_0^2/(\mu L)$. The first term (I) on the right-hand side of Eq. (3.10) corresponds to the classic conductivity calculated by the Hele-Shaw analogy [87]; the second term (II) comes from wall permeation [14]; the third term (III), which is the novel contribution of our calculation, and is explicitly a function of the flow-wise coordinate x, is due to the *coupled* effect of geometry variation, fluid inertia, and wall permeation.

3.2.4 Wall permeation velocity

Substituting the expression for dp^*/dx^* into the vertical velocity from Eq. (3.6), and evaluating the result at $z^* = h^*$, we obtain the *a priori* unknown wall permeation velocity

$$v_w(x) = -V_0 \frac{h(x)\delta}{3\phi h_0 + h(x)}. \tag{3.11}$$

Recall that $\alpha < 0$ ($\Rightarrow \delta < 0$), so $v_w > 0$, i.e., the velocity is *into* the wall. Observe that both v_w and the term (III) in C vanish for $\alpha = 0$ ($\Rightarrow \delta = 0$) (parallel walls) because, in this case, there is no driving force to push fluid into the porous walls. We have imposed the full volumetric flux onto the leading-order solution (see also [183]), and it must be conserved. Note $v_w \neq 0$ for $\phi = 0$ because there can still be fluid penetrating the wall in the normal direction even if there is no (tangential) slip. The permeation velocity for $\phi = 0$ is driven by the flow-wise contraction of the aperture (rather than being imposed *a priori* [14]).

3.3 Results and Discussion

Figure 3.1 shows the flow profile generated from the perturbative solution from Sect. 3.2, for a fracture with linear aperture variation. The streamlines highlight the 2D nature of the velocity field, as well as permeation through the fracture's top wall. The pressure does not vary with z^*, as required by the lubrication (small aspect ratio, $\epsilon \ll 1$) approximation.

Next, we validate our mathematical results against "full" Navier–Stokes direct numerical simulations (DNS) [187]. We carried out DNS using the simpleFoam solver in OpenFOAM® ver. 7.0 [159], [178], an open-source library based on the *finite volume method* [160]. The simulations (see Supplementary Material for description of the method) were performed using the Hele-Shaw cell geometry with varying aperture along x from Fig. 1.5. Importantly, unlike previous computational studies on flow in fractures with permeable walls [188], we did *not* impose the wall (tangent and normal) velocities from the theory onto the simulations. The latter approach is akin to verification, while we seek validation [189] between theory and simulation. Instead, we imposed a tensorial slip condition on the tangential velocity (the BJS BC) coupled with a normal pressure flux BC, to allow the simulation to self-

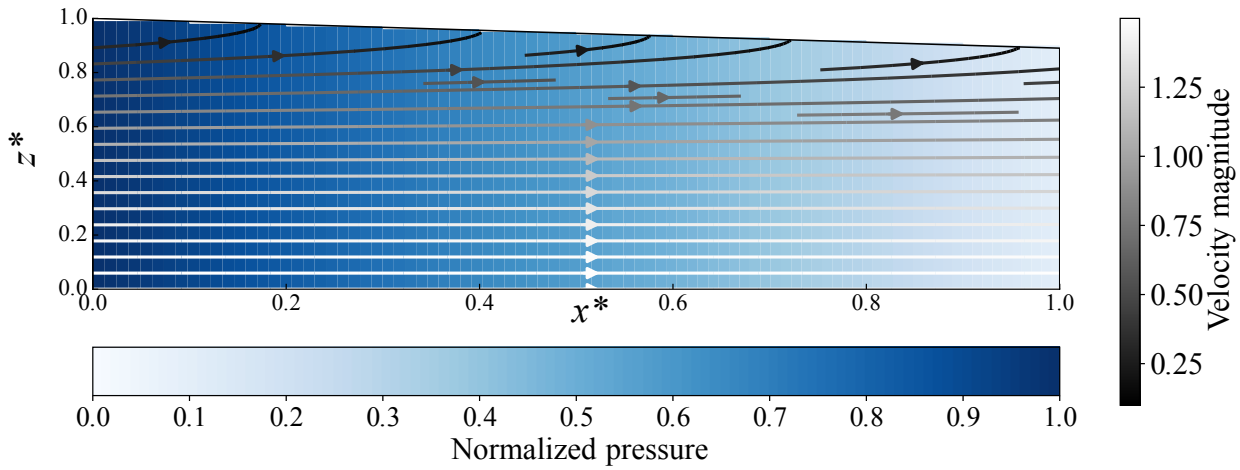

Figure 3.1. Illustration of the dimensionless analytical flow solution (Eqs. (3.4), (3.5) and (3.6)) obtained for the model shaped fracture with permeable angled walls. Only the top half ($0 \leq z^* \leq 1$) is shown, for clarity. Background color denotes pressure, and curves are streamlines shaded by velocity magnitude. Here, $\alpha = -10^{-3}$, $\epsilon = 0.01$, $\tilde{Re} = 0.01$, $\phi = 10^{-3}$.

consistently determine the flow (in particular, the unknown wall permeation velocity) and pressure profiles.

The DNSs provide the 2D velocity field and the pressure distribution, i.e., it solves for $\left(u^*(x^*, z^*), v^*(x^*, z^*)\right)$ and $p^*(x^*, z^*)$ (both scaled as in Eq. (3.1)). From these quantities, the volumetric flux across a vertical cross-section and the pressure gradient at a given x^* are computed, yielding $\langle u^*(x^*)\rangle$ and dp^*/dx^*. Their ratio, $\langle u^*\rangle/(-dp^*/dx^*)$ is to be compared to the theoretically predicted dimensionless hydraulic conductivity $\mathcal{K}^*(x^*)$ from Eq. (3.8).

First, in Fig. 3.2, we show the velocity profiles across the midlength plane ($x^* = 0.5$) of fractures with different slopes. The simulation results agree well with theory. The zoomed-in inset in Fig. 3.2(a) highlights that u^* does not start from 0, but rather some finite value, as required by the BJC partial slip BC. For all α, $v^* = 0$ at the centerline ($z^* = 0$) as required by symmetry, then increases smoothly in absolute value towards the walls (Fig. 3.2(b)). Fluid enters into the surrounding porous medium and the wall permeation velocity $v_w^* = v^*|_{z^*=h^*}$ is self-consistently computed (shown in Supplementary Material Fig. S.7). The wall permeation velocity increases with $|\alpha|$ to maintain the imposed flux through these narrowing fractures.

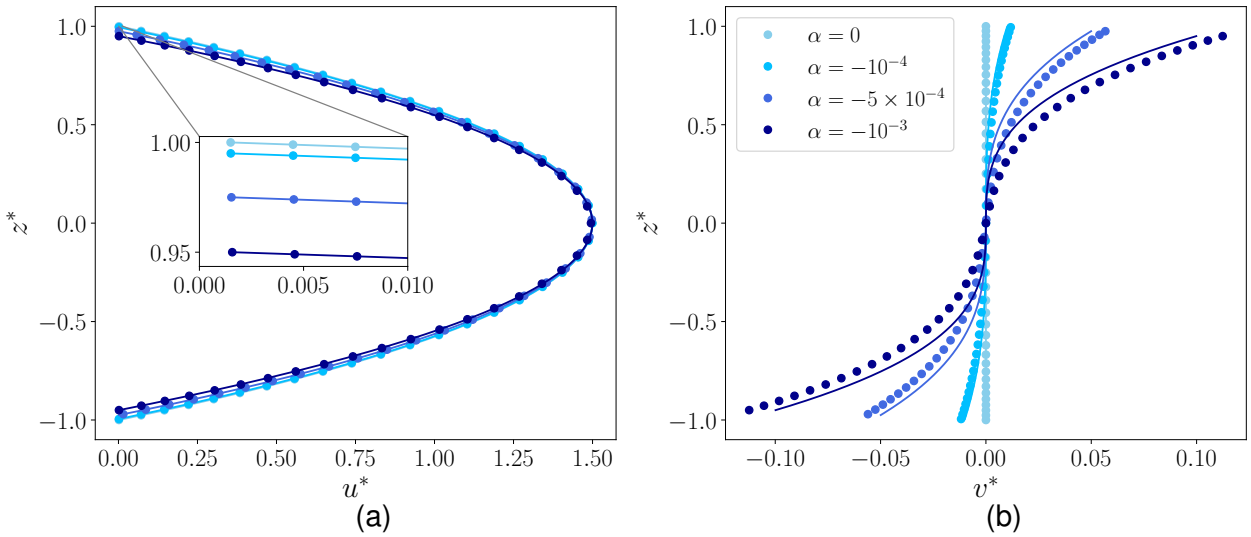

Figure 3.2. Dimensionless velocity profiles across the fracture aperture z^*, at the mid-fracture plane $x^* = 0.5$, for $\phi = 5 \times 10^{-4}$ and $\tilde{Re} = 0.01$: (a) the horizontal component $u^*(x^*, z^*)$ (inset highlights the non-zero slip velocity at the wall); (b) the vertical component $v^*(x^*, z^*)$. Solid curves are the theoretical profiles from Eq. (3.6), and filled circles with the same colors are the corresponding simulation results. Colors represent different α values (see legend).

Meanwhile, for $\alpha = 0$, $v^* = 0$ for all z^*, i.e., there is no permeation into the porous medium, only slip at the fluid–solid interfaces ($z^* = \pm 1$).

To verify the derived analytical expression for the hydraulic conductivity in a shaped fracture, we compute $\mathcal{K}^*(x^*)$ in multiple angled fractures with permeable walls, based on typical reservoir properties summarized in Table 1.1. Figure 3.3(a) shows the predicted $\mathcal{K}^*$ (from theory) against the simulated $\mathcal{K}^*$ values along the fracture (multiple x^* for each) for multiple slope values α, and multiple slip coefficients ϕ, for fixed $\tilde{Re}$. In the same color family, the brightness of the color refers to the value of ϕ: the darker the color, the smaller ϕ is. The classical conductivity $\mathcal{K} = 1/3$ (i.e., for $\alpha = \phi = 0$) calculated from the Hele-Shaw analogy [86], [87] is shown by • (simulated) and — (predicted). All data points in Fig. 3.3(a) lie close to the line of slope 1, which means that the predicted conductivity (from theory) is in good agreement with the simulations. For $\phi > 10^{-3}$, the correlated trend continues, but in these cases the slip length is large and the single-domain simulation approach is not

appropriate (the flow in the surrounding porous medium should be resolved as well to be able to impose suitable BCs numerically).

In Fig. 3.3(b), we plot the conductivity variation along the flow-wise (x^*) direction, a novel prediction of the present theory. By comparing the conductivity for the same α but different ϕ, for example, $\alpha = -10^{-3}$ (the red color family), we observe that wall slip has only a weak effect on $\mathcal{K}^*$. By comparing the conductivity for different α (different color families), we observe that $\mathcal{K}^*$ decreases with x^*, which means that it becomes "harder" for the fluid to flow through the narrowing fractures. Of course this is expected on physical grounds, but this effect of α on $\mathcal{K}^*$ had not been quantified prior to this study. In particular, our results in Fig. 3.3 show that that even weak slopes have a much more significant impact on the conductivity, than wall slip due to the permeability of the walls. Likewise, the wall permeation velocity v_w^* has *not* been *a priori* specified, and is also a strong function of α (recall Sect. 3.2.4 and Fig. 3.10 below in Sect. 3.A.2).

3.4 Conclusions and Outlook

The contribution of this study is the mathematical expressions, Eqs. (3.9) and (3.10), that relate the fracture conductivity to the geometric and physical quantities, and which explicitly shows the coupling between the fracture shape (in terms of its wall angle), the permeability of the porous wall (in terms of the Beavers–Joseph–Saffman slip length), and the inertia of the fluid in the fracture (in terms of a Reynolds number). Additionally, unlike previous studies on fractures with permeable walls, we self-consistently determined the wall permeation velocity, Eq. (3.6), which is *a priori* unknown and is set by the balance of pressure forces pushing fluid into the walls, and the permeability of the surrounding matrix. From these results, we concluded that the coupling effect of geometric variation, wall permeation and inertia leads to a decreasing conductivity along a narrowing fracture. Importantly, what has not been appreciated in previous studies is that, among these factors, the geometric variation (specifically, the resistance to flow induced by the narrowing of a fracture) dominates the conductivity change, even for slow shape variation (small slopes). The theory was validated

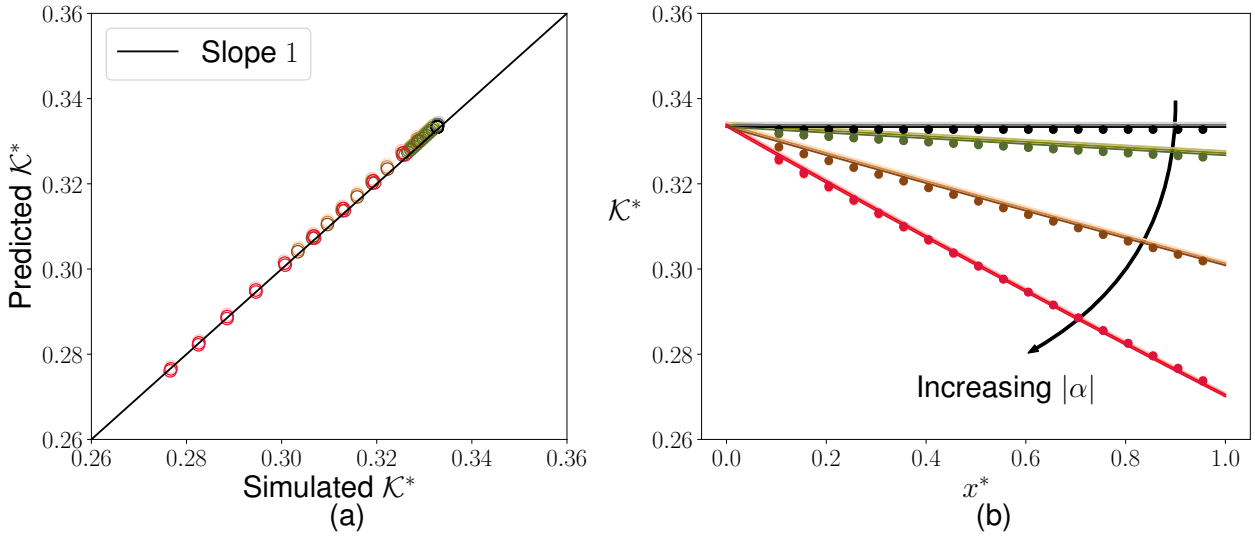

Figure 3.3. The dimensionless conductivity $\mathcal{K}^*$ of shaped fractures, for different slip coefficients ϕ and wall slopes α: (a) correlation plot of predicted $\mathcal{K}^*$ values from Eq. (3.8) versus simulated $\mathcal{K}^*$ values; (b) the variation of $\mathcal{K}^*(x^*)$ along the fracture length. Colors represent cases with different α and ϕ values: ●●●: $\alpha = 0$, $\phi \in \{0, 5\times10^{-4}, 10^{-3}\}$; ●●●: $\alpha = -10^{-4}$, $\phi \in \{0, 5\times10^{-4}, 10^{-3}\}$; ●●●: $\alpha = -5\times10^{-3}$, $\phi \in \{0, 5\times10^{-4}, 10^{-3}\}$; ●●●: $\alpha = -10^{-3}$, $\phi \in \{0, 5\times10^{-4}, 10^{-3}\}$. In (b), filled circles represent the simulation results, and solid curves of the same color represent the corresponding theoretical prediction Eq. (3.10) with $\tilde{Re} = 0.01$.

against direct numerical simulation of the Navier–Stokes equations in a model Hele-Shaw geometry.

3.A Appendix

The supporting material consists of two sections, seven figures 3.4 to 3.10, and Table 3.1.

Section 3.A.1 provides the steps in the derivation of the hydraulic conductivity presented and discussed in the main text. These steps are included for completeness and to aid a reader in following the mathematical derivation.

Section 3.A.2 describes the OpenFOAM® solver methodology for generating the direct numerical simulation data reported in the main text. Section 3.A.2 includes ancillary details about the verification of the simulations (grid independence tests) and post-processing of

the simulation data. Toward these ends, Figs. 3.4 through 3.9 are appended to the end of Section 3.A.2.

The OpenFOAM® solver and post-processing scripts are freely available at the repository https://github.com/daihui-lu/HydraulicConductivityofShapedFractures, per the "Research data availability" statement in the main text.

Figures 3.9 and 3.10 are complementary representations of data and information discussed in the main text. They are provided for completeness but are not essential to the conclusions in the main text.

3.A.1 Supplementary steps in the main analytical derivations

The Beavers–Joseph–Saffman (BJS) [105], [107] partial slip boundary condition (BC) on the permeable wall is

$$u^* = -\phi\left(\frac{\partial u^*}{\partial z^*} + \epsilon^2\frac{\partial v^*}{\partial x^*}\right) = -\phi\frac{\partial u^*}{\partial z^*} + \mathcal{O}(\epsilon^2) \qquad \text{at} \qquad z^* = \pm h^*(x^*). \tag{3.12}$$

The slip coefficient ϕ, which is a dimensionless slip length (i.e., $\phi = \ell_{\text{slip}}/h_0$), is an empirically-measurable quantity that enforces a shear stress balance at the porous walls, as discussed in the Introduction of the main text.

Let $\tilde{Re} = \epsilon Re$ be finite as $\epsilon \to 0$. Then, upon taking the limit $\epsilon \to 0$ of Eqs. (3.2), Eq. (3.2a) remains unchanged, and Eqs. (3.2b) and (3.2c) become

$$\tilde{Re}\, u^*\frac{\partial u^*}{\partial x^*} + \tilde{Re}\, v^*\frac{\partial u^*}{\partial z^*} = -\frac{\partial p^*}{\partial x^*} + \frac{\partial^2 u^*}{\partial z^{*2}}, \tag{3.13a}$$

$$0 = -\frac{\partial p^*}{\partial z^*}. \tag{3.13b}$$

Now, assume a regular perturbation expansion in $\tilde{Re} \ll 1$. The velocity field is expanded as

$$u^* = u_0^* + \tilde{Re}\, u_1^* + \cdots, \tag{3.14a}$$

$$v^* = v_0^* + \tilde{Re}\, v_1^* + \cdots. \tag{3.14b}$$

Substituting Eqs. (3.14) into Eqs. (3.13) and neglecting $\mathcal{O}(\tilde{Re})$ and higher-order terms, we obtain the leading-order momentum equations:

$$0 = -\frac{\partial p^*}{\partial x^*} + \frac{\partial^2 u_0^*}{\partial z^{*2}}, \tag{3.15a}$$

$$0 = -\frac{\partial p^*}{\partial z^*}, \tag{3.15b}$$

subject to the boundary conditions (BCs):

$$\underbrace{\left.\frac{\partial u_0^*}{\partial z^*}\right|_{z^*=0} = 0, \quad v_0^*|_{z^*=0} = 0}_{\text{symmetry}} \quad \text{and} \quad \underbrace{u_0^*|_{z^*=h^*} = -\phi \left.\frac{\partial u^*}{\partial z^*}\right|_{z^*=h^*}}_{\text{BJS BC}}. \tag{3.16}$$

Recall that, by symmetry, we are only solving for the profile in the top half of the fracture. Therefore, the leading-order solution for the horizontal velocity has the form

$$u_0^*(x^*, z^*) = \frac{1}{2}\frac{dp^*}{dx^*} z^{*2} + \mathfrak{C}_1(x^*) z^* + \mathfrak{C}_2(x^*), \tag{3.17}$$

where $\mathfrak{C}_1$ and $\mathfrak{C}_2$ are arbitrary (integration) functions of x^*. Since p^* is independent of z^* by Eq. (3.15b), henceforth we write $\partial p^*/\partial x^* = dp^*/dx^*$. Imposing the boundary conditions (3.16) onto Eq. (3.17), we obtain

$$u_0^*(x^*, z^*) = \left(\frac{h^{*2} - z^{*2}}{2} + \phi h^*\right)\left(-\frac{dp^*}{dx^*}\right). \tag{3.18}$$

Since the flow is in the direction of positive x^*, $dp^*/dx^* < 0$, so we choose to associate a negative sign with this term in some equations, for clarity, as is standard in the fluid mechanics literature. Then, the leading-order depth-averaged velocity is

$$\langle u_0^* \rangle(x^*) = \frac{1}{h^*(x^*)} \int_0^{h^*(x^*)} u_0^*(x^*, z^*)\, dz^* = \frac{3\phi h^*(x^*) + h^*(x^*)^2}{3}\left(-\frac{dp^*}{dx^*}\right). \tag{3.19}$$

Next, we determine the leading-order vertical velocity. From the conservation of mass equation,

$$\frac{\partial u^*}{\partial x^*} + \frac{\partial v^*}{\partial z^*} = 0, \tag{3.20}$$

we deduce that

$$\frac{\partial v_0^*}{\partial z^*} = -\frac{\partial u_0^*}{\partial x^*} = \left(h^* \frac{dh^*}{dx} + \phi \frac{dh^*}{dx}\right) \frac{dp^*}{dx^*} - \left(\frac{z^{*2} - h^{*2}}{2} - \phi h^*\right) \frac{d^2 p^*}{dx^{*2}}. \tag{3.21}$$

Now, integrating both sides of Eq. (3.21) from 0 to an arbitrary z^*, and using the second boundary condition in Eq. (3.16), we find that the vertical velocity is

$$v_0^*(x^*, z^*) = \left(h^* \frac{dh^*}{dx} + \phi \frac{dh^*}{dx}\right) z^* \frac{dp^*}{dx^*} - \left(\frac{z^{*3}}{6} - \frac{h^{*2} z^*}{2} - \phi h^* z^*\right) \frac{d^2 p^*}{dx^{*2}}. \tag{3.22}$$

From Eqs. (3.13), we obtain the first-order perturbation equation:

$$u_0^* \frac{\partial u_0^*}{\partial x^*} + v_0^* \frac{\partial u_0^*}{\partial z^*} = \frac{\partial^2 u_1^*}{\partial z^{*2}}. \tag{3.23}$$

Substituting the $\mathcal{O}(1)$ solution from Eq. (3.18) above into Eq. (3.23), we obtain

$$\frac{\partial^2 u_1^*}{\partial z^{*2}} = \left[\left(\frac{h^{*2}}{2} + \phi h^*\right)^2 + \frac{z^{*4}}{12}\right] \frac{dp^*}{dx^*} \frac{d^2 p^*}{dx^{*2}} + \left(\frac{h^{*2} + z^{*2}}{2} + \phi h^*\right) (h^* + \phi) \frac{\alpha}{\epsilon} \left(\frac{dp^*}{dx^*}\right)^2, \tag{3.24}$$

subject to homogeneous BCs:

$$\left.\frac{\partial u_1^*}{\partial z^*}\right|_{z^*=0} = 0 \quad \text{and} \quad u_1^*|_{z^*=h^*} = 0. \tag{3.25}$$

Integrating both sides of Eq. (3.24) from 0 to an arbitrary z^*, and substituting the boundary conditions from Eq. (3.25), we obtain the first-order inertial correction to the horizontal velocity component:

$$\begin{aligned} u_1^*(x^*, y^*) = &\left[\left(\frac{h^{*2}}{2} + \phi h^*\right)^2 \frac{z^{*2} - h^{*2}}{2} + \frac{1}{360}\left(z^{*6} - h^{*6}\right)\right] \frac{dp^*}{dx^*} \frac{d^2 p^*}{dx^{*2}} \\ &+ \left[\left(\frac{h^{*2}}{2} + \phi h^*\right) \frac{z^{*2} - h^{*2}}{2} + \frac{z^{*4} - h^{*4}}{24}\right] (h^* + \phi) \frac{\alpha}{\epsilon} \left(\frac{dp^*}{dx^*}\right)^2. \end{aligned} \tag{3.26}$$

From the latter, we find the depth-averaged velocity correction:

$$\begin{aligned}\langle u_1^* \rangle &= \frac{1}{h^*(x^*)} \int_0^{h^*(x^*)} u_1^*(x^*, z^*)\, dz^* \\ &= \left(\frac{3}{35}h^{*6} + \frac{1}{3}\phi h^{*5} + \frac{\phi^2}{3}h^{*4}\right)\left(-\frac{dp^*}{dx^*}\right)\frac{d^2p^*}{dx^{*2}} - \left(\frac{1}{5}h^{*4} + \frac{1}{3}\phi h^{*3}\right)(h^* + \phi)\frac{\alpha}{\epsilon}\left(\frac{dp^*}{dx^*}\right)^2 .\end{aligned} \tag{3.27}$$

To close the problem, we need another constraint. Mohais, Xu, Dowd, *et al.* [14] provided one solution by assuming a *constant* permeation velocity v_w in a parallel fracture ($\alpha = 0$, $h^* = 1$), i.e., $v_0|_{z=\pm h} = \pm v_w$ ($v_0^*\big|_{z^*=\pm 1} = \pm 1$). If we apply this constraint to the above analysis, the dimensionless average horizontal velocity becomes

$$\begin{aligned}\langle u^* \rangle &= \left[\frac{3\phi + 1}{3} + \tilde{Re}\left(\frac{3}{35} + \frac{1}{3}\phi + \frac{\phi^2}{3}\right)\frac{3}{3\phi + 1}\right]\left(-\frac{dp^*}{dx^*}\right) \\ &= \left(\frac{3\phi + 1}{3}\right)\left[1 + \tilde{Re}\left(\frac{3}{35} + \frac{1}{3}\phi + \frac{\phi^2}{3}\right)\frac{9}{(3\phi + 1)^2}\right]\left(-\frac{dp^*}{dx^*}\right).\end{aligned} \tag{3.28}$$

This solution differs from [14] in that the we have expanded only the velocity u^* in powers of $\tilde{Re}$, while Mohais, Xu, Dowd, *et al.* [14] expanded p^* as well and obtained (using our notation):

$$-\frac{dp^*}{dx^*} = \langle u^* \rangle \left\{\frac{3}{1 + 3\phi} - \tilde{Re}\left[\frac{9(7\phi + 1)}{140(1 + 3\phi)^3} + \left(\frac{3 + 6\phi}{2 + 6\phi}\right)^2\right]\right\}. \tag{3.29}$$

To the leading order in $\tilde{Re}$, we may use the Taylor series $(1 - \xi)^{-1} = 1 + \xi + \mathcal{O}(\xi^2)$ to rewrite (3.29) as

$$\langle u^* \rangle = \left(\frac{3\phi + 1}{3}\right)\left\{1 + \tilde{Re}\left[\frac{3(7\phi + 1)}{140(3\phi + 1)^2} + \frac{3(2\phi + 1)^2}{4(3\phi + 1)}\right]\right\}\left(-\frac{dp^*}{dx^*}\right). \tag{3.30}$$

Despite the different expansion methods used to obtain Eqs. (3.28) and (3.30), the leading-order terms are the same, i.e., they both yield:

$$\langle u^* \rangle = \frac{1}{3}(1 + 3\phi)\left(1 + \frac{27}{35}\tilde{Re}\right)\left(-\frac{dp^*}{dx^*}\right) + \mathcal{O}(\tilde{Re}^2, \phi^2, \phi\tilde{Re}), \tag{3.31}$$

meaning they are asymptotically equivalent for $\phi \ll 1$ and $\tilde{Re} \ll 1$.

Now, however, the wall permeation velocity v_w (and its relation to the pressure gradient dp/dx) is not necessarily known *a priori*. To close the problem, we apply the flux constraint $\langle u_0^* \rangle = 1$ to Eq. (3.19), and we obtain

$$\frac{dp^*}{dx^*} = -\frac{3}{3\phi h^*(x^*) + h^*(x^*)^2} \qquad \Rightarrow \qquad \frac{d^2p^*}{dx^{*2}} = \frac{(9\phi + 6h^*)\delta}{[3\phi h^*(x^*) + h^*(x^*)^2]^2}. \tag{3.32}$$

Substituting the latter results into Eq. (3.27) and suppressing the explicit notation that h^* is a function of x^*, we have

$$\langle u_1^* \rangle = \frac{h^{*3}(28\phi^{*2} + 22\phi h^* + 3h^{*2})\delta}{35(3\phi + h^*)^2} \frac{dp^*}{dx^*}. \tag{3.33}$$

Finally, from Eqs. (3.19) and (3.33), $\langle u^* \rangle$ can be reconstituted into a Darcy's law, as shown in Eq. (3.8) in the main text and discussed therein.

3.A.2 Implementation of the numerical solver and its verification

The solution algorithm for the incompressible Navier–Stokes equations [Eqs. (3.2) in the main text] used in our direct numerical simulation (DNS) study is SIMPLE (*semi-implicit method for pressure-linked equations*) [see, e.g., 160, Ch. 15]. In this study, we set the tolerance for the pressure and velocity components' residuals to be 10^{-5} (see the example convergence plot in Fig. 3.4). The BCs applied in the simulation are summarized in the schematic in Fig. 3.5. In particular, note that the BJS BC (3.12) is, mathematically, a Robin (or mixed-type) BC. However, within the iterative algorithm, we reformulated it as a Dirichlet boundary condition to enhance stability and ensure consistency of fluxes within the pressure iterations.

The BJS BC, as given in the computational paper by Layton, Schieweck, and Yotov [180], is essentially a slip condition enforcing a specific value of the velocity field in the face-planar direction of the boundary cell. In this formulation, the condition does not alter the velocity normal to the porous walls.

In OpenFOAM® [159], [178] and, more generally, in the finite volume method [160], discretization is performed by summing all the contribution from the volumetric source

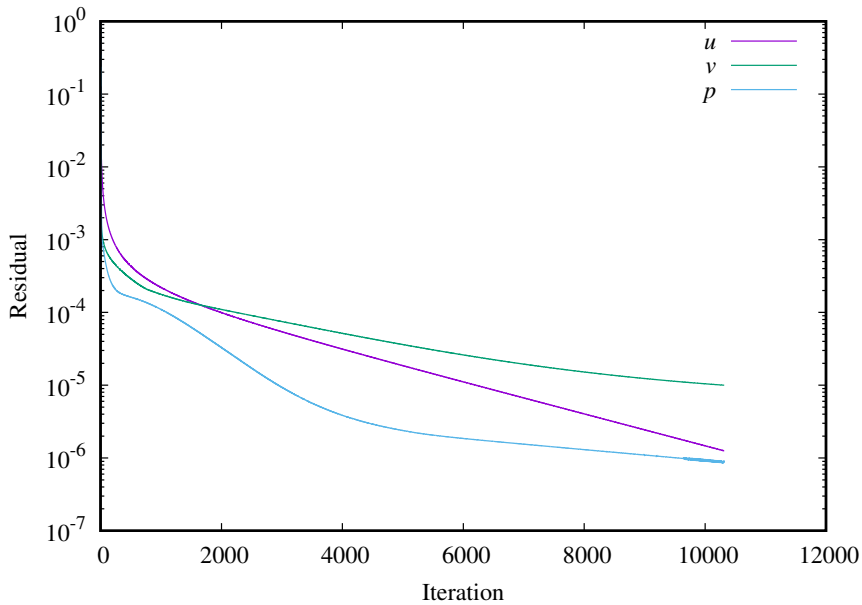

Figure 3.4. SIMPLE algorithm's residuals plot for a sample simulation with $\alpha = -10^{-3}$, $\phi = 5 \times 10^{-4}$ and $\tilde{Re} = 0.01$. The tolerance used is 10^{-5} for both the pressure residual and each velocity component's residual. The simulation converges after about 10 000 iterations.

terms (if present) and fluxes, looping over all the cell faces. In order to discretize generic differential equations without any specific knowledge of the form of the fluxes, OpenFOAM® requires that each flux is expressed in terms of a face value $\boldsymbol{u}_f$ and a face-normal gradient $(\nabla \boldsymbol{u})_f \cdot \boldsymbol{n}_f$, where f is a generic face and $\boldsymbol{n}_f$ is the vector normal to such face. Therefore, an explicit or implicit (i.e., matrix coefficients) expression for those two face-based fields is required. Boundary faces are no exception. Thus, with reference to Fig. 3.6, it is necessary to provide expressions for $\boldsymbol{u}_b$ and $(\nabla \boldsymbol{u})_b \cdot \boldsymbol{n}$ that take into account the BJS BC. In vector form, the boundary condition reads:

$$\mathbf{T} \cdot \boldsymbol{u}_b = -\mathbf{T} \cdot \left(\ell \frac{\partial \boldsymbol{u}}{\partial n} \right)_b , \tag{3.34}$$

where $\mathbf{T} = (\mathbf{I} - \boldsymbol{n}\boldsymbol{n})$ is the projector on the tangential plane, $\mathbf{I}$ is the identity operator, and $\ell = \ell_{\text{slip}}$ is the BJS slip length discussed in the main text.

However, a problem described by the Navier–Stokes equations with a BC of the type in Eq. (3.34) is not well posed, since such condition only constrains the face-planar field.

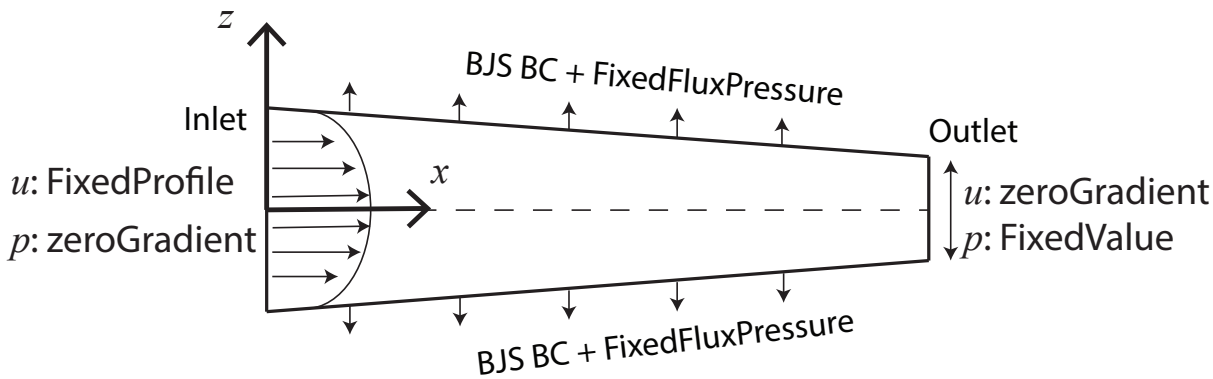

Figure 3.5. Schematic of the OpenFOAM® boundary conditions used in the numerical simulations.

Therefore, it is necessary to specify a condition on the face-normal field. Since the BJS BC does not provide such a constrain, we assume that all the flow arriving normal to the boundary leaves the domain. This assumption corresponds to:

$$\boldsymbol{n} \cdot \left(\frac{\partial \boldsymbol{u}}{\partial n} \right)_b = 0 \,. \tag{3.35}$$

In this sense, condition (3.35) merely correspond to copying the value of the velocity field in the first cell. In fact, using a linear interpolation scheme one obtains:

$$\boldsymbol{n} \cdot \left(\frac{\partial \boldsymbol{u}}{\partial n} \right)_b \approx \frac{\boldsymbol{n} \cdot (\boldsymbol{u}_b - \boldsymbol{u}_c)}{\delta x} \,, \tag{3.36}$$

which results in:

$$\boldsymbol{n} \cdot \boldsymbol{u}_b = \boldsymbol{n} \cdot \boldsymbol{u}_c \,. \tag{3.37}$$

Equation (3.34) is also discretized using a linear interpolation scheme:

$$\mathbf{T} \cdot \boldsymbol{u}_b = -\mathbf{T} \cdot \left(\ell \frac{\boldsymbol{u}_b - \boldsymbol{u}_c}{\delta x} \right) = \mathbf{T} \cdot \left(\ell \frac{\boldsymbol{u}_c}{\delta x + \ell} \right) \,. \tag{3.38}$$

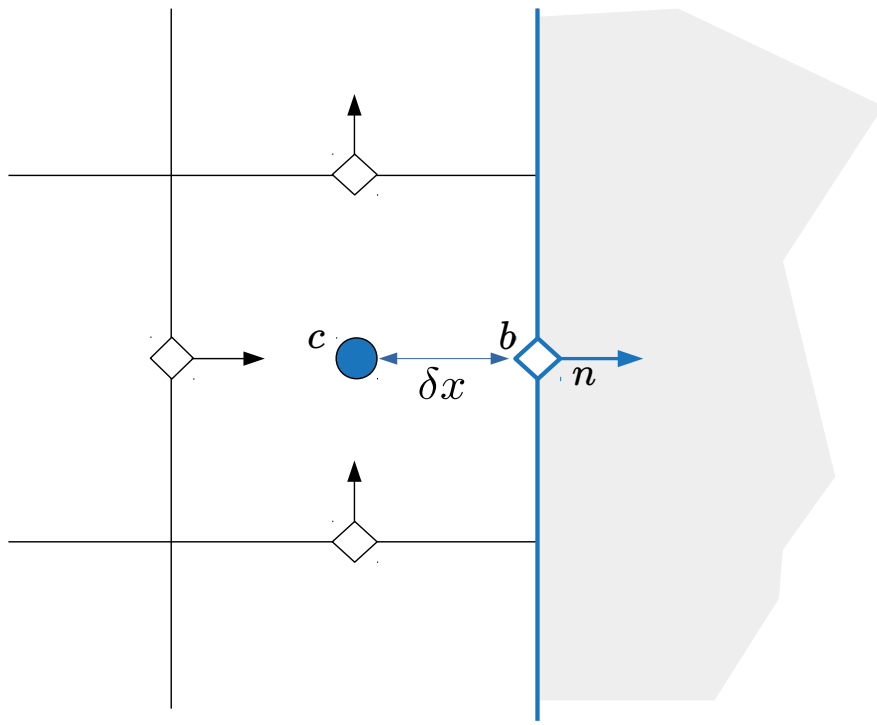

Figure 3.6. Illustration of a boundary cell with face centers an face normals. In this figure, c is the cell center (blue dot) and the blue line represents the boundary. The BJS BC is applied at point b, corresponding to the center of the boundary face, where δx is the distance between b and c, and $\boldsymbol{n}$ is the vector normal to the boundary face.

The final form of the BC is then implemented as a Dirichlet BC:

$$\boldsymbol{u}_b = \boldsymbol{n}(\boldsymbol{n} \cdot \boldsymbol{u}_b) + \mathbf{T} \cdot \boldsymbol{u}_b = \boldsymbol{n}(\boldsymbol{n} \cdot \boldsymbol{u}_b) + \mathbf{T} \cdot \left(\ell \frac{\boldsymbol{u}_c}{\delta x + \ell} \right) . \tag{3.39}$$

This formulation clearly requires multiple fixed point iterations that, if they converge, result in the correct calculation of $\boldsymbol{u}_p$ up to second-order accuracy. For the pressure field, we employ a *fixedFluxPressure* BC, which essentially imposes a pressure gradient based on the flux leaving the domain, and allows the simulation to self-consistently determine the wall permeation velocity.

Since we study steady flow, the initial conditions are only relevant for the convergence (rather than the accuracy), so they are simply specified as zero velocity and zero pressure.

At the inlet of the fracture ($x = 0$), we impose the theoretically computed velocity profile given by Eqs. (3.18) and (3.21) (with dp^*/dx^* computed from Eq. (3.27) under the constraint $\langle u^* \rangle = 1$), which has a non-zero permeation velocity and satisfies the BJS BC at the inlet's walls ($z = \pm h_0$).

A zero-gradient velocity BC is employed across the outlet plane ($x = L$), and the pressure there is set to zero gauge pressure (see Fig. 3.5). We do not consider the case of a closed fracture, so we do not need to impose a crack-tip condition.

To find the optimal computational grid arrangement for the simulations results presented in the main text, we ran a series of test cases with different numbers of grid elements and with different grid resolutions (spacing), as summarized in Table 3.1. The simulations can be considered non-dimensional (the fluid's physical properties are chosen to fix the dimensionless parameters such as $\tilde{Re}$). To maintain ϵ, the simulation channel has length $L = 100$ and inlet half-aperture $h_0 = 1$. From each simulation, we extracted the velocities at the cross-sectional plane located at $x = L/2$ ($x^* = 0.5$). We also extracted the pressure gradient dp/dx variation along the whole channel. Then, we calculated the percent change of these quantities with respect to the theoretical values (see above). Finally, the velocities from the simulations were rescaled by $\langle u \rangle$ to be comparable to the theory, since the constraint $\langle u \rangle = 1$ was imposed in the derivation.

The grid independence study revealed that the optimal choice is 4000 grid elements with $\Delta x = 0.5$ and $\Delta z = 0.05$, as it showed significantly better performance on the permeation velocity than coarser girds and finer grids did not improve the accuracy notably (see Fig. 3.7). The slip velocity and axial pressure gradient showed convergence for 4000 grid elements, with the error increasing for larger grids. Therefore, we used 4000 grid elements for all DNS results reported in the main text. Note that a non-uniform grid spacing (see Fig. 3.8) was used in the vertical direction to better resolve the flow near the porous walls.

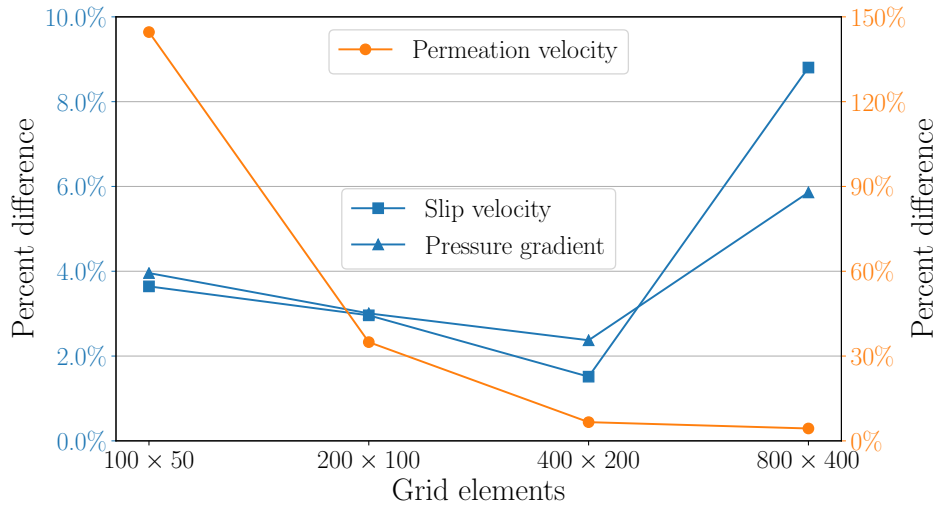

Figure 3.7. Grid independence of key (dimensionless) flow quantities. Percent difference (relative to the theoretical solution in the main text) of the wall permeation velocity $v^*\Big(x^*, h^*(x^*)\Big)$, the wall slip velocity $u^*\Big(x^*, h^*(x^*)\Big)$, and the axial component of the pressure gradient dp^*/dx^*, all evaluated at $x^* = 0.5$ but using different grids.

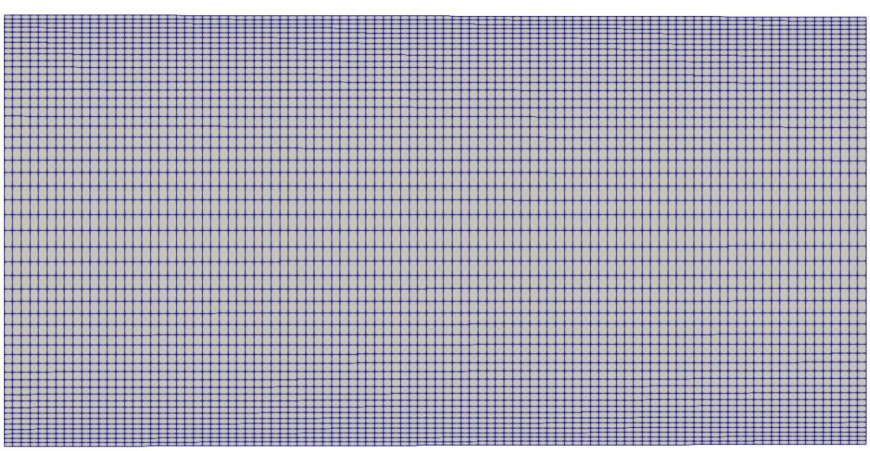

Figure 3.8. Schematic of the computational grid showing the non-uniform vertical spacing ("boundary layer meshing"). Notice that the grid spacing is scaled in the horizontal direction to fit the figure.

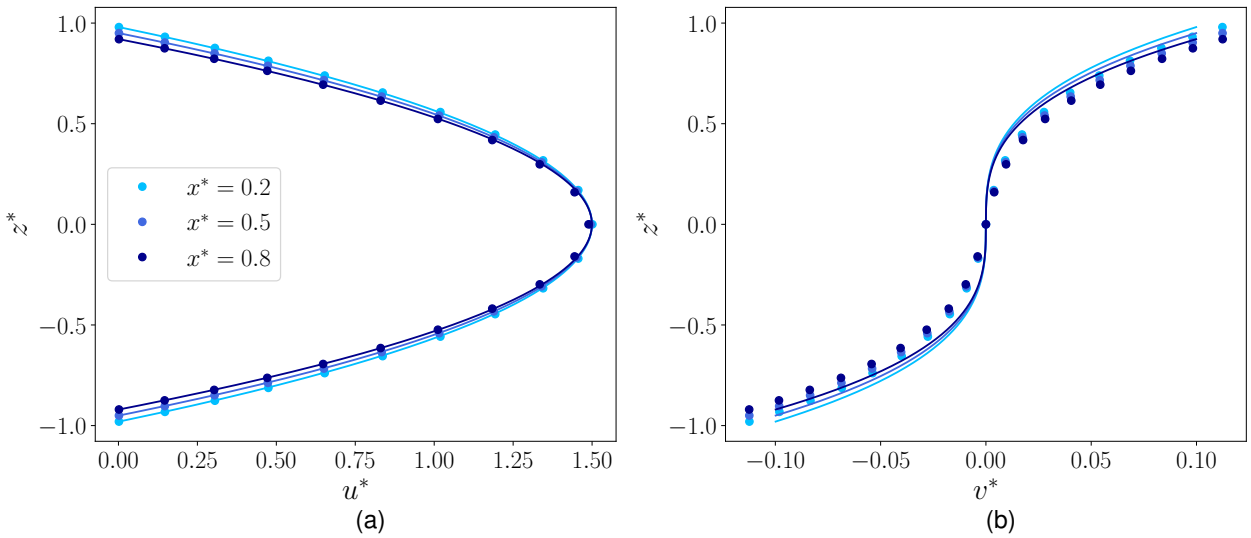

Figure 3.9. Flow-wise variation: Dimensionless velocity profiles versus fracture aperture z^* at the planes $x^* \in \{0.2, 0.5, 0.8\}$, for $\alpha = -10^{-3}$, $\phi = 10^{-4}$ and $\tilde{Re} = 0.01$: (a) the horizontal component $u^*(x^*, z^*)$; (b) the vertical component $v^*(x^*, z^*)$. Solid curves are the theoretical profiles from Eq. (3.22), and filled circles with the same colors are the corresponding simulation results. Profiles are color-coded by their x^* positions.

Table 3.1. Information about the grids used to establish grid independence of the direct numerical simulation results.

Grid arrangement	100×50	200×100	400×200	800×400
Total grid elements	5 000	20 000	80 000	320 000
Δx resolution	1	0.5	0.25	0.125
Δz resolution	0.02	0.01	0.005	0.0025

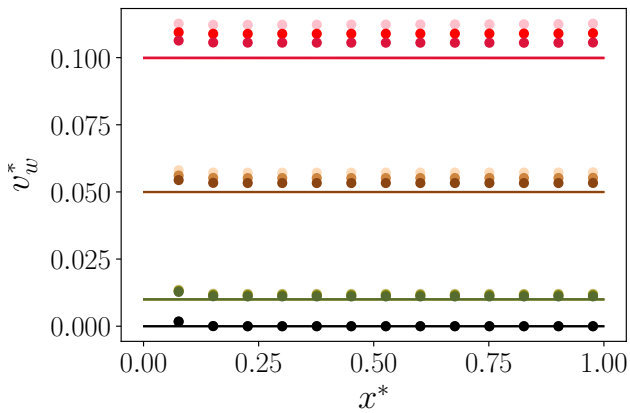

Figure 3.10. The dimensionless wall permeation velocity $v_w^*(x^*)$ along the channel for $\tilde{Re} = 0.01$. Colors represent cases with different α and ϕ values: ●●●: $\alpha = 0$, $\phi \in \{0, 5\times10^{-4}, 10^{-3}\}$; ●●●: $\alpha = -10^{-4}$, $\phi \in \{0, 5\times10^{-4}, 10^{-3}\}$; ●●●: $\alpha = -5\times10^{-3}$, $\phi \in \{0, 5\times10^{-4}, 10^{-3}\}$; ●●●: $\alpha = -10^{-3}$, $\phi \in \{0, 5\times10^{-4}, 10^{-3}\}$. Filled circles represent the simulation results, and solid curves of the same color represent the corresponding theoretical predictions.

4. PHYSICS-INFORMED NEURAL NETWORKS FOR UNDERSTANDING THE SHEAR MIGRATION OF PARTICLES IN VISCOUS FLOW

SUMMARY

We harness the physics-informed neural network (PINN) approach to extend the utility of phenomenological models for particle migration in shear flow. Specifically, we propose to constrain the neural network training via a model for the physics of shear-induced particle migration in suspensions. Then, we train the PINN against experimental data from the literature, showing that this approach provides both better fidelity to the experiments, and novel understanding of the relative roles of the hypothesized migration fluxes. We first verify the PINN approach for solving the inverse problem of radial particle migration in a non-Brownian suspension in an annular Couette flow. In this classical case, the PINN yields the same value (as reported in the literature) for the ratio of the two empirical model parameters. Next, we apply the PINN approach to analyze experiments on particle migration in both non-Brownian and Brownian suspensions in Poiseuille slot flow, for which a definitive calibration of the phenomenological migration model has been lacking. Using the PINN approach, we identify the unknown/empirical parameters in the physical model through the inverse solver capability of PINNs. Specifically, the values are significantly different from those for the Couette cell, highlighting an inconsistency in the literature that uses the latter value for Poiseuille flow. Importantly, the PINN results also show that the inferred values of the empirical model's parameters vary with the shear Péclet number and the particle bulk volume fraction of the suspension, instead of being constant as assumed in previous literature.

The material in this chapter has been submitted for publication as [D. Lu and I. C. Christov, "Physics-informed neural networks for understanding shear migration of particles in viscous flow," preprint, arXiv:2111.04684, 2021] [190].

4.1 Problem statement

Phillips, Armstrong, Brown, *et al.* [118] proposed an insightful phenomenological model for the shear-induced migration of particles in a low Reynolds number flow [124]. Specifically, they posited that the distribution of particles, accounted for by the volume fraction $\phi(\boldsymbol{x}, t)$ of the fluid–particle suspension, obeys a conservation law [118], [138]:

$$\frac{D\phi}{Dt} = -\boldsymbol{\nabla} \cdot \boldsymbol{J}. \tag{4.1}$$

In Eq. (4.1), the material derivative of the left-hand side represents the unsteady transport of particles by a flow $\boldsymbol{u}$, while $\boldsymbol{J}$ on the right-hand side represents a spatial flux arising from the hydrodynamic interactions of particles. Consequently, Eq. (4.1) is often referred to as a *diffusive-flux model* in the literature. Phillips, Armstrong, Brown, *et al.* [118] decomposed the flux as $\boldsymbol{J} = \boldsymbol{N}_c + \boldsymbol{N}_\eta + \boldsymbol{N}_B$, where they posited that $\boldsymbol{N}_c$, $\boldsymbol{N}_\eta$ and $\boldsymbol{N}_B$ represent the particle fluxes due to the variations in the particle collision frequency, the spatial variations of the viscosity of the suspension, and the spatial variations of the concentration (responsible for Brownian diffusion, by Fick's law), respectively. For unidirectional flows, $D\phi/Dt = \partial\phi/\partial t$ [138].

Specifically, Phillips, Armstrong, Brown, *et al.* [118] proposed the following "constitutive laws" for the diffusive fluxes:

$$\boldsymbol{N}_c = -K_c a_p^2 \left(\phi^2 \boldsymbol{\nabla} \dot{\gamma} + \phi \dot{\gamma} \boldsymbol{\nabla} \phi \right), \tag{4.2a}$$

$$\boldsymbol{N}_\eta = -K_\eta \dot{\gamma} \phi^2 \left(\frac{a_p^2}{\eta} \right) \frac{d\eta}{d\phi} \boldsymbol{\nabla} \phi, \tag{4.2b}$$

$$\boldsymbol{N}_B = -D \boldsymbol{\nabla} \phi, \tag{4.2c}$$

where K_c and K_η are *a priori* unknown constants of order unity, which are found from experimental data (by fitting/calibration). Therefore, Eq. (4.1), with the fluxes given in Eqs. (4.2), becomes a *parametrized partial differential equation* (PDE). Here, a_p is a particle's radius, D is its Brownian diffusivity (in principle, known from the Stokes–Einstein relation $D = k_B T / 6\pi\eta_s a_p$ with T being temperature and k_B being Boltzmann's constant), η is the

non-constant dynamic viscosity of the suspension, which may depend on many parameters [191], η_s is the carrier Newtonian fluid's viscosity, and $\dot{\gamma}(\boldsymbol{x}, t)$ is the non-uniform shear rate in the flow. For a general flow field $\boldsymbol{u}(\boldsymbol{x}, t)$, the shear rate is evaluated as the magnitude of the rate-of-strain tensor $\boldsymbol{E} = \frac{1}{2}(\boldsymbol{\nabla u} + \boldsymbol{\nabla u}^\top)$, i.e., $\dot{\gamma} = \sqrt{2\boldsymbol{E} : \boldsymbol{E}}$.

At steady state, $\partial(\,\cdot\,)/\partial t = 0$. Then, Eq. (4.1) can be integrated once in space over some domain $\mathcal{V}$, with the constant of integration set to zero by imposing a no-flux condition on the domain's boundary $\partial\mathcal{V}$. Therefore, the resulting governing physics equation at steady-state is

$$\boldsymbol{N}_c + \boldsymbol{N}_\eta + \boldsymbol{N}_B = \boldsymbol{0}, \tag{4.3}$$

which can be considered as a "continuity equation" expressing the conservation of particles. Equation (4.3) also implies that if the initial particle volume fraction is such that $\int_{\mathcal{A}} \phi(\boldsymbol{x}, 0)\, d\boldsymbol{x} = \phi_b = const.$ across any cross-section $\mathcal{A}$, then $\int_{\mathcal{A}} \phi(\boldsymbol{x}, t)\, d\boldsymbol{x} = \phi_b$ for any $t > 0$. Additionally, the flow field $\boldsymbol{u}$ obeys the Stokes flow momentum equation [118], which takes the form (using a more standard [37] sign convention and definition of $\boldsymbol{E}$ as above):

$$\boldsymbol{\nabla} \cdot \boldsymbol{\tau} = \boldsymbol{\nabla} p, \qquad \boldsymbol{\tau} = 2\eta \boldsymbol{E}, \qquad \eta = \eta_s \eta_r(\phi), \tag{4.4}$$

where η_r (dimensionless) is the contribution from the suspension to be introduced below, and $p(\boldsymbol{x})$ is the hydrodynamic pressure. We will consider only neutrally buoyant suspensions, and so body forces are neglected in Eq. (4.4). The velocity field is additionally incompressible, $\boldsymbol{\nabla} \cdot \boldsymbol{u} = 0$, but this relation is automatically satisfied by the unidirectional flows considered herein [37], so it is not a physical constraint that we need to enforce explicitly.

The fluid mechanics of particulate suspensions remains a frontier problem [137], and the diffusive-flux model of Phillips, Armstrong, Brown, *et al.* [118] is not without its criticisms [138]. Nevertheless, although much more sophisticated models of suspensions exist [20], [139], including the suspension balance model [126], [127], [140]–[142], the two-fluid model [143], even direct numerical simulation [129], Eqs. (4.1)–(4.2) remain a popular model through which to study shear-induced particle migration in suspensions [144]–[146].

"Disentagling" the individual effects of shear-induced fluxes in Eq. (4.3) has been of particular interest in the suspensions literature [192]. (Note that although Merhi, Lemaire, Bossis, *et al.* [192] also included a fourth, "curvature-induced" flux in Eq. (4.3), its origin has been disputed by Bricker and Butler [193].) Machine learning is a viable approach toward processing experimental data to disentangle the relative strengths of the fluxes in Eq. (4.3). To this end, in Section 4.2, we apply the novel physics-informed neural network (PINN) approach of Raissi, Perdikaris, and Karniadakis [148] towards understanding particle migration in shear flow. Specifically, we propose to constrain the neural network using the model given by Eqs. (4.3) and (4.4). In Section 4.3, we validate this approach on the classical Couette cell experiments (and modeling) of Phillips, Armstrong, Brown, *et al.* [118]. Then, in Section 4.4, we apply the PINN approach to the more challenging case of Poiseuille channel flow. In doing so, we re-interpret experiments on pressure-driven flows of both non-Brownian (Section 4.4.2) and Brownian (Section 4.4.3) suspensions, uncovering new aspects of the shear-induced migration model. Finally, conclusions are drawn in Section 4.5. Additional data pre-processing and verification details (regarding the PINN calculations) are provided in Appendices 4.A.1 and 4.A.2, respectively.

4.2 PINN algorithm description and implementation

In recent years, with the explosive growth of available data, computing modalities, and requisite hardware resources, deep learning algorithms have been applied to a range of problems arising from computer science, physics and engineering fields [194], including in the field of fluid mechanics [195]. It has been suggested that machine learning could "have influence closer to the principles of fluid mechanics, when [...] used in conjunction with human reasoning" [196, p. 4]. In this vein, *physics-informed machine learning* has emerged as an approach that "integrates seamlessly data and mathematical physics models, even in partially understood ... contexts" [197]. Specifically, Raissi, Perdikaris, and Karniadakis [148] developed a computational approach to couple machine learning with some underlying physics (human reasoning), which they termed *physics-informed neural networks* (PINNs). PINNs are a deep learning framework for solving problems involving PDEs by embedding

(in a suitable sense) the physics into the neural network. Due to their versatility, PINNs have been applied to solve forward and inverse problems in fluid mechanics [198]–[203], solid mechanics [204], [205], material science [206], and heat transfer [207], amongst many other applications. PINNs are appealing due to their standardized implementation. They use automatic differentiation [208] techniques to discretize the differential operators needed for the back-propagation problem, as well as the PDEs representing the physics [148], [209]. This approach makes PINNs mesh-free and, thus, easy to use for evaluating the PDE residual even from sparse experimental data sets ('observations'). Importantly, PINNs can determine unknown parameters in the physics embedded therein, even from incomplete (or partial) data sets, making PINNs useful for reduced-order model calibration.

In this chapter, we use a PINN to solve the inverse problem of reduced-model determination for particle migration in suspensions. Given measurements of a velocity field component u and a particle volume fraction profile ϕ, we seek to learn the unknown parameters K_c and K_η in the model given in Eq. (4.2). The governing physics equations are embedded into the PINN as shown in Fig. 4.1. We use two independent neural networks, NN(u) and NN(ϕ), to approximate the velocity distribution and particle distribution profile, respectively. Both NNs are fully-connected and feed-forward, with multiple hidden layers each.

Suppose that the measured data is available on N (possibly random) sample points. The residuals of the fluid's conservation of momentum equation (4.4) and the suspension's continuity equation (4.3) (suitably simplified for some given flow conditions and domain geometry) are evaluated from the approximated values of u and ϕ at these N collocation points. Then, combining the error between predictions and observations with the error in satisfying the physics from the residuals, along with any constraints, we formulate a loss function as:

$$\mathscr{L} = \underbrace{w_u \mathrm{MSE}_u + w_\phi \mathrm{MSE}_\phi}_{\text{training data}} + \underbrace{w_p \mathrm{MSE}_p + w_m \mathrm{MSE}_m}_{\text{physics}} + \underbrace{w_c \mathrm{MSE}_c}_{\text{constraints}}, \tag{4.5}$$

where, for example,

$$\mathrm{MSE}_u = \frac{1}{N}\sum_{i=1}^{N} \|\boldsymbol{u}(i) - \boldsymbol{u}_{\mathrm{train}}(i)\|^2, \tag{4.6a}$$

$$\mathrm{MSE}_\phi = \frac{1}{N}\sum_{i=1}^{N} |\phi(i) - \phi_{\mathrm{train}}(i)|^2, \tag{4.6b}$$

$$\mathrm{MSE}_p = \frac{1}{N}\sum_{i=1}^{N} \|\boldsymbol{N}_c(i) + \boldsymbol{N}_\eta(i) + \boldsymbol{N}_B(i)\|^2, \tag{4.6c}$$

$$\mathrm{MSE}_m = \frac{1}{N}\sum_{i=1}^{N} \|\boldsymbol{\nabla}\cdot\boldsymbol{\tau}(i) - \boldsymbol{\nabla}p(i)\|^2. \tag{4.6d}$$

The MSE terms in $\mathscr{L}$ represent various "mean squared errors." The notation "(i)" denotes the value of the quantity at the ith data point in the set of N observations. For clarity, we omit this explicit notation below without fear of confusion. The first two terms of $\mathscr{L}$ correspond to the errors between the predicted and the input velocity and particle distribution training data, respectively. Then, the following two terms of $\mathscr{L}$ correspond to error in satisfaction of the physics, *i.e.*, the suspension's momentum equation (4.4) and continuity equation (4.3), respectively. The last term of $\mathscr{L}$ represent errors committed in satisfaction of "constraints." The constraints can involve, *e.g.*, boundary conditions, integral constraints, or any other mathematical statement not captured in the "physics" term, which is typically used to denote only the satisfaction of governing (partial) differential equations. The coefficients w_j where $j \in \{u, \phi, m, p, c\}$, represent weights of the corresponding loss terms. Although the relative values of the weights of terms in the loss function may influence the ability to train the NN [210], here we generally take them to be equal.

Figure 4.1 shows the architecture of the PINN. Initially, a randomly selected set of network weight vectors $\boldsymbol{\Theta}_u^{(0)}$ and $\boldsymbol{\Theta}_\phi^{(0)}$ are used to construct NN(u) and NN(ϕ), respectively. Then, we feed NN(u) and NN(ϕ) with training data, and obtain predictions on u and ϕ. We calculate the derivatives of u and ϕ needed to evaluate the physics-informed loss terms via automatic differentiation in TensorFlow [211]. Then, starting with guesses $K_c^{(0)}$ and $K_\eta^{(0)}$ for the model parameters, we calculate the loss terms corresponding to the continuity and momentum equations, as well as any constraints. The activation function is the hyperbolic tangent function. During the process of minimizing $\mathscr{L}$, $\boldsymbol{\Theta}_u^{(k)}$, $\boldsymbol{\Theta}_\phi^{(k)}$, $K_c^{(k)}$ and $K_\eta^{(k)}$ are updated

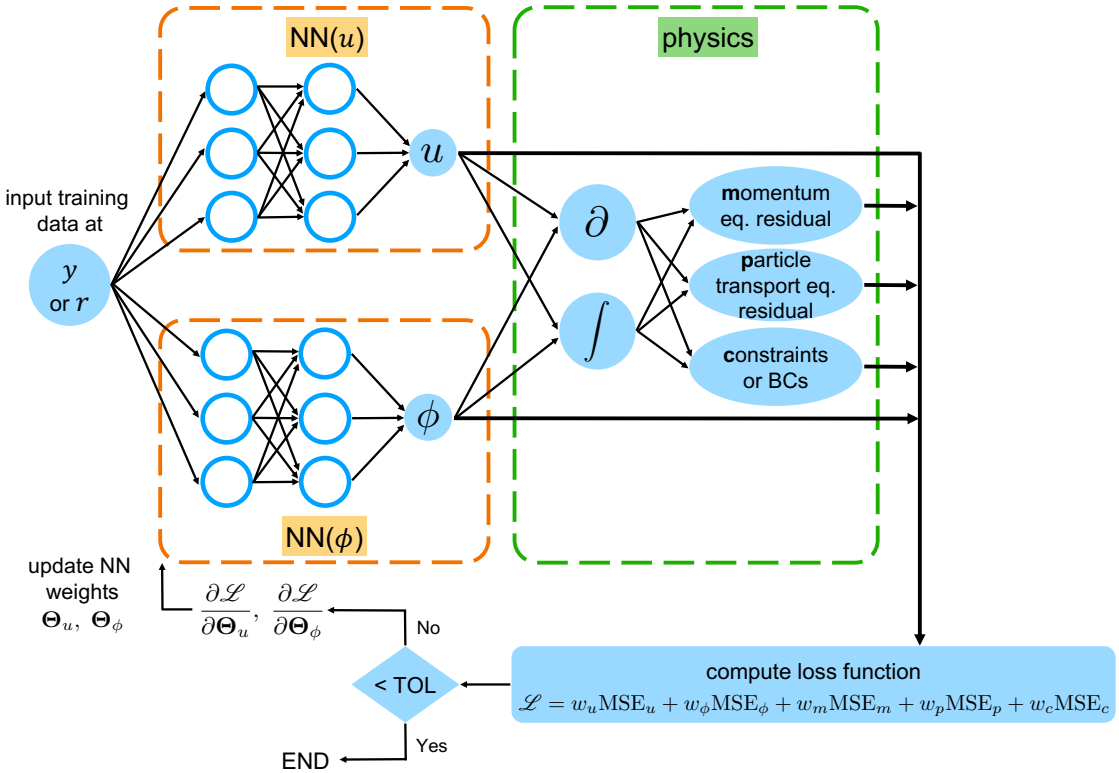

Figure 4.1. Architecture of the proposed PINN for solving the inverse problem of reduced-model determination for particle migration in suspensions. The loss $\mathscr{L}$ is formulated (as in Eq. (4.5)) in terms of root-mean-squared errors between predictions and observations (MSE_u, MSE_ϕ), and errors in satisfaction of the underlying PDEs from physics (MSE_m, MSE_p), as well as boundary conditions and/or additional constraints (MSE_c).

at each iteration k. The loss function is minimized using "Adam" [212], which is a stochastic gradient descent algorithm, and "L-BFGS-B" subsequently. The stopping criterion for the optimization is that the change in the loss function between iterations is less than machine precision. However, this stopping criterion may or may not satisfy our convergence criterion. So, upon the stoppage of the optimization procedure, we check that $\mathscr{L} < \mathrm{TOL}$, for some prescribed tolerance $\mathrm{TOL} \simeq 10^{-2}$. Upon satisfaction of the latter criterion, we consider the solution converged. Then, we have obtained not only the optimized neural networks' weights $\mathbf{\Theta}_u$ and $\mathbf{\Theta}_\phi$, but also the initially unknown model parameters K_c and K_η.

4.3 Couette flow

4.3.1 Governing physics equations

For flow between concentric rotating cylinders, the domain is $\mathcal{V} = \{\boldsymbol{x} = (r, \theta) \mid \kappa R \leq r \leq R,\ 0 \leq \theta < 2\pi\}$, where $\kappa < 1$ is dimensionless, and the problem is independent of the axial, z, coordinate. The radial component of the momentum equation (4.4) (where Stokes flow is now in cylindrical coordinates [37]) reduces to

$$\frac{1}{r^2}\frac{\partial}{\partial r}\left(r^2 \tau_{r\theta}\right) = 0 \qquad \Rightarrow \qquad \tau_{r\theta} = \frac{A}{r^2}, \tag{4.7}$$

where A is a constant to be calculated by imposing boundary conditions [118]. Note that in this case of axisymmetric flow, $\partial p/\partial\theta = 0$. Equivalently,

$$\dot{\gamma} = \dot{\gamma}_{r\theta} = \frac{A}{r^2\eta}, \qquad A = \frac{-\Omega}{\int_{\kappa R}^{R} (r^3\eta)^{-1}\, dr}, \tag{4.8}$$

where Ω is the angular velocity of the inner cylinder. On dimensional grounds alone, for a neutrally buoyant non-Brownian suspension at low Reynolds number at steady state, it is expected that $\eta/\eta_s = \eta_r(\phi)$ [191], where η_s is the Newtonian solvent's dynamic viscosity, and $\eta_r(\phi)$ is the dimensionless contribution to the viscosity due to particles. Indeed, the experiments of Phillips, Armstrong, Brown, *et al.* [118] were verified to be in this specific regime, and they used the empirical Krieger–Dougherty relation:

$$\eta_r(\phi) = \left(1 - \frac{\phi}{\phi_m}\right)^{-a}, \tag{4.9}$$

where $\phi_m = 0.68$ is the maximum packing volume fraction, and $a = 1.82$ is a positive empirical exponent (in principle, related to ϕ_m [191]). The form of Eq. (4.9) and values for ϕ_m and a are based on experimental correlations [213], [214], and they are well-established for non-Brownian suspensions [20], [215]. Here, we are only interested in interrogating the particle migration model, so any fitting parameters for the fluid and suspension properties are taken as per the literature.

Next, dimensionless governing equations are obtained by scaling the dimensional variables in the following way:

$$r^* = r/R, \qquad \dot{\gamma}^*(r^*) = \dot{\gamma}_{r\theta}(r)/\Omega, \qquad u^*(r^*) = u_\theta(r)/U_{\max}, \tag{4.10}$$

where $U_{\max} = \Omega\kappa R$ is the maximum velocity at the rotating wall. Therefore, the momentum equation (4.8) can be written as

$$\dot{\gamma}^*(r^*) = \frac{-1}{r^{*2}\eta_r \int_\kappa^1 (r^{*3}\eta_r)^{-1}\, dr^*}. \tag{4.11}$$

Neglecting the Brownian flux, the continuity equation (4.3) for the non-Brownian suspension in this geometry is

$$\frac{1}{\dot{\gamma}}\frac{d\dot{\gamma}}{dr} + \frac{1}{\phi}\frac{d\phi}{dr} + \frac{K_\eta}{K_c}\frac{1}{\eta}\frac{d\eta}{dr} = 0, \tag{4.12}$$

where we have dropped the '$r\theta$' subscript on $\dot{\gamma}$ without fear of confusion. Equation (4.12) can be nondimensionalized as follows:

$$\frac{1}{\dot{\gamma}^*}\frac{d\dot{\gamma}^*}{dr^*} + \frac{1}{\phi}\frac{d\phi}{dr^*} + \frac{K_\eta}{K_c}\frac{1}{\eta_r}\frac{d\eta_r}{dr^*} = 0. \tag{4.13}$$

Observe that in this (non-Brownian) case, only the ratio K_η/K_c of the two model parameters shows up in the final form of the particle transport equation. In other words, there is only a single quantity to "fit," and this fact is reflected in the PINN architecture used for this problem.

Additionally, the particle distribution satisfies

$$\frac{1}{1-\kappa}\int_\kappa^1 \phi(r^*)\, dr^* = \phi_b, \tag{4.14}$$

where ϕ_b is the bulk volume fraction. The uniform distribution of particles at the initial time is then $\phi(r, t = 0) = \phi_b$, and at steady state conservation of mass requires that Eq. (4.14) hold.

Phillips, Armstrong, Brown, *et al.* [118] suggested, based on analysis of their experiments, that $K_c/K_\eta \approx 0.66$ best fits the profile measured for steady-state Couette flow of suspensions of $2a_p = 675$ µm particles at $\phi_b = 0.55$. The agreement was also good when comparing with experimental data at $\phi_b = 0.45$, 0.50 and 0.55. In this section, we wish to investigate the best-fit value of K_c/K_η obtained by the PINN approach for solving the inverse problem.

4.3.2 PINN loss function

For this problem, the loss function is

$$\mathscr{L} = w_u \mathrm{MSE}_u + w_\phi \mathrm{MSE}_\phi + w_p \mathrm{MSE}_p + w_m \mathrm{MSE}_m + w_c \mathrm{MSE}_c. \tag{4.15}$$

The notation for the MSE terms was introduced in Sect. 4.2. These terms are now implemented as

$$\mathrm{MSE}_u = \frac{1}{N}\sum_{i=1}^{N} |u^* - u^*_{\mathrm{train}}|^2, \tag{4.16a}$$

$$\mathrm{MSE}_\phi = \frac{1}{N}\sum_{i=1}^{N} |\phi - \phi_{\mathrm{train}}|^2, \tag{4.16b}$$

$$\mathrm{MSE}_m = \frac{1}{N}\sum_{i=1}^{N} \left| \dot{\gamma}^* + \frac{1}{r^{*2}\eta_r \int_\kappa^1 (r^{*3}\eta_r)^{-1}\, dr^*} \right|^2, \tag{4.16c}$$

$$\mathrm{MSE}_p = \frac{1}{N}\sum_{i=1}^{N} \left| \frac{1}{\dot{\gamma}^*}\frac{d\dot{\gamma}^*}{dr^*} + \frac{1}{\phi}\frac{d\phi}{dr^*} + \frac{K_\eta}{K_c}\frac{1}{\eta_r}\frac{d\eta_r}{dr^*} \right|^2, \tag{4.16d}$$

$$\mathrm{MSE}_c = \left| \frac{1}{1-\kappa}\int_\kappa^1 \phi(r^*)\, dr^* - \phi_b \right|^2. \tag{4.16e}$$

The integrals in the expressions in Eqs. (4.16c) and (4.16e) are approximated by averages over the randomly selected set of collocation points (essentially a Monte Carlo quadrature): $\int_\kappa^1(\cdot) = \sum_{i=1}^N (\cdot) \times (1-\kappa)/N$. Appendix 4.A.1 describes how the experimental data (digitized from [118]) was pre-processed into training data.

Note that the output variables of the NNs are u and ϕ, as depicted in Fig. 4.1. Thus, the remaining variables η_r and $\dot{\gamma}^*$ have to be expressed in terms of these output variables.

Recall that $\dot{\gamma} = rd(u_\theta/r)/dr$ for purely azimuthal flow by definition [37]. Then, using the nondimensionalization from Eq. (4.10):

$$\dot{\gamma}^*(r^*) = \kappa r^* \frac{d}{dr^*}\left(\frac{u^*(r^*)}{r^*}\right). \tag{4.17}$$

Substituting the expression for $\dot{\gamma}^*$ from Eq. (4.17) and η_r from Eq. (4.9) into the MSE expressions (4.16c) and (4.16d), the loss function from Eq. (4.15) now depends only on the NN weights ($\mathbf{\Theta}_u$ and $\mathbf{\Theta}_\phi$) and the parameter K_c/K_η. By minimizing the resulting $\mathscr{L}(\mathbf{\Theta}_u, \mathbf{\Theta}_\phi, K_c/K_\eta)$ with respect to its arguments, we find the NNs and the value of K_c/K_η that simultaneously lead to the best agreement with the training data *and* the physics.

4.3.3 Comparison between PINN, theory and experiment

To evaluate the "theoretical" particle distribution profile, we use the chain $d\eta_r/dr^* = (d\eta_r/d\phi)(d\phi/dr^*)$ to re-write Eq. (4.13) as:

$$\left(\frac{1}{\phi} + \frac{K_\eta}{K_c}\frac{1}{\eta_r}\frac{d\eta_r}{d\phi}\right)\frac{d\phi}{dr^*} = -\frac{1}{\dot{\gamma}^*}\frac{d\dot{\gamma}^*}{dr^*} = \left(\frac{2}{r^*} + \frac{1}{\eta_r}\frac{d\eta_r}{d\phi}\frac{d\phi}{dr^*}\right), \tag{4.18}$$

where the second equality follows from using the dimensionless version of Eq. (4.8). Now, Eq. (4.18) can be rearranged as an ODE for $\phi(r^*)$:

$$\left[\frac{1}{\phi} + \left(\frac{K_\eta}{K_c} - 1\right)\frac{1}{\eta_r}\frac{d\eta_r}{d\phi}\right]\frac{d\phi}{dr^*} = \frac{2}{r^*}. \tag{4.19}$$

Finally, we can use the Krieger viscosity from Eq. (4.9), multiply both sides of Eq. (4.19) by ϕ and solve for $d\phi/dr^*$, to obtain a first-order nonlinear ODE for $\phi(r^*)$:

$$\frac{d\phi}{dr^*} = \frac{2\phi}{[(K_\eta/K_c - 1)a(\phi/\phi_m)(1-\phi/\phi_m)^{-1} + 1]r^*}, \tag{4.20}$$

which is the same as Eq. (21) of Phillips, Armstrong, Brown, *et al.* [118]. Equation (4.20) can be integrated from $r^* = \kappa$ to $r^* = 1$ using an arbitrary value $\phi(r^* = \kappa) = \phi_w \in [0, 1]$ as the initial condition. Then, a nonlinear iteration (implemented using `optimize.root_scalar`

from the SciPy stack in Python [168]) updates ϕ_w until the constrain (4.14) is satisfied for the given ϕ_b. This solution will be shown as the "theory" curve in the figures below.

In Fig. 4.2, we compare our PINN results using $w_u = w_\phi = w_p = w_m = w_c = 1$ to theory (numerical solution of Eq. (4.20)) and the experiments (by Phillips, Armstrong, Brown, *et al.* [118]). We use neural networks with two hidden layers with 10 nodes in each layer and a learning rate of 0.001 for the Adam optimizer. The process of choosing a suitable number of layers and nodes is discussed in Appendix 4.A.2.

Two versions of the theoretical prediction for the particle distribution profile are shown in Fig. 4.2(b). One is calculated by solving Eq. (4.20) (numerically by the method described above) using the value $K_c/K_\eta = 0.66$ suggested in [118]. The other theoretical prediction is derived via the *ad-hoc* approximation $1.82(1 - K_\eta/K_c) \approx -1$ made in Phillips, Armstrong, Brown, *et al.* [118]. We observe that the PINN prediction is an improvement over the numerical solution of Eq. (4.20). Surprisingly, the approximation $1.82(1 - K_\eta/K_c) \approx -1$ improves the agreement further between the theory and experiments. This approximation, made out of convenience in [118], does not appear to be justifiable on the basis of mathematical grounds (such as perturbation theory), therefore its good agreement with experiment must be simply coincidence.

As evidenced by Fig. 4.2, we obtain good agreement between the PINN predictions and the experimental data, for both u^* and ϕ. To account for the statistical variation in the converged ("learned") value of K_c/K_η due to the random initialization of the NNs, we averaged the predictions from 100 using different initializations to obtain a statistical result with mean and standard error: $K_c/K_\eta = 0.66 \pm 0.05$, which is consistent with the fitted value in [118] by their non-machine-learning approach. Thus, we have validated the PINN approach for the shear-induced migration of non-Brownian particles in a concentric Couette cell, showing that PINNs do not only provide suitable predictions for the velocity and particle distribution profiles, but they also "learn" the accepted value of the model parameter K_c/K_η given in the literature.

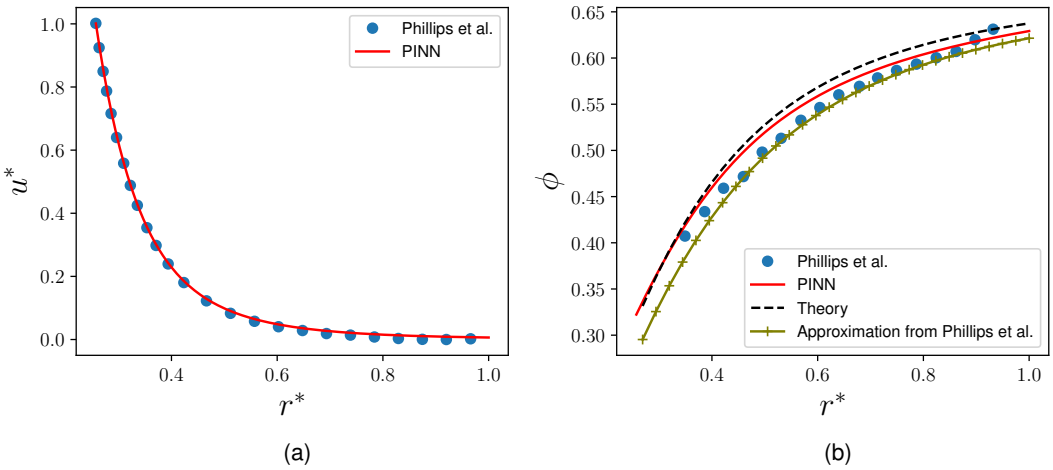

Figure 4.2. Validation of the proposed PINN approach to shear-induced migration. The PINN is applied to analyze the experiment from Phillips, Armstrong, Brown, *et al.* [118] in a concentric Couette cell at $\phi_b = 0.55$, yielding: (a) the dimensionless velocity profile $u^*(r^*)$ and (b) the particle distribution (volume fraction) $\phi(r^*)$. Symbols represent the experimental data from Phillips, Armstrong, Brown, *et al.* [118]; red solid curves are PINN predictions; dashed curve is the numerical solution of Eq. (4.20); curve with cross symbols in (b) is the approximate analytical solution from Phillips, Armstrong, Brown, *et al.* [118, Eqs. (24)–(25)]. The PINN "learns" a value of the unknown model parameter $K_c/K_\eta \approx 0.66$, which is in agreement with [118].

4.4 Poiseuille flow

4.4.1 Governing physics equations

For Poiseuille flow in a slot of height $2H$, the domain is $\mathcal{V} = \{\boldsymbol{x} = (x, y) \mid -H \leq y \leq +H,\ -\infty < x < \infty\}$. For fully developed flow, the x dependence drops out, and we introduce the dimensionless variables

$$x^* = x/L, \qquad y^* = y/H, \qquad \dot{\gamma}^*(y^*) = \dot{\gamma}(y)/\dot{\gamma}_0, \qquad u^*(y^*) = u_x(y)/U_{\max}, \tag{4.21}$$

where $U_{\max}$ is the centerline (maximum) velocity of the solvent fluid at the same volumetric flow rate, $\dot{\gamma}_0 = U_{\max}/H$ is the mean shear rate, and L is a typical axial length scale for the channel.

Now, the dimensionless continuity equation (4.3) for the suspension takes the form

$$K_c\phi\left(\phi\frac{d^2u^*}{dy^{*2}}+\frac{du^*}{dy^*}\frac{d\phi}{dy^*}\right)+K_\eta\frac{du^*}{dy^*}\frac{\phi^2}{\eta_r}\frac{d\eta_r}{dy^*}+\frac{1}{Pe}\frac{d\phi}{dy^*}=0. \tag{4.22}$$

In Eq. (4.22), Pe is the shear Péclet number, which quantifies the relative importance of shear migration to Brownian migration of particles [191], defined as

$$Pe=\frac{a_p^2\dot{\gamma}_0}{D}=\frac{6\pi\eta_s a_p^3\dot{\gamma}_0}{k_BT}, \tag{4.23}$$

where k_B is Boltzmann's constant, and T is temperature. Observe that unlike the case of Eq. (4.13), Eq. (4.22) for finite Pe cannot be divided by K_c (to only consider the ratio K_η/K_c). Again, the particle distribution is constrained such that

$$\frac{1}{2}\int_{-1}^{+1}\phi(y^*)\,dy^*=\int_0^1\phi(y^*)\,dy^*=\phi_b. \tag{4.24}$$

For a dense non-Brownian suspension ($Pe\gg 1$), the velocity is not parabolic [118], [216]. Its shape is found by solving the momentum equation (4.4) for pressure-driven Poiseuille flow of the suspension:

$$\frac{d}{dy^*}\left(\eta_r(\phi)\frac{du^*}{dy^*}\right)=G^*=\frac{GH^2}{\eta_sU_{\max}}, \tag{4.25}$$

where G^* (resp. G) is the dimensionless (resp. dimensional) axial pressure gradient, which is constant in unidirectional flow [37]. Integrating Eq. (4.25) once and imposing a centerline symmetry condition, we have

$$\eta_r(\phi)\frac{du^*}{dy^*}=G^*y^*. \tag{4.26}$$

Similarly to the approach of Reyes, Howard, Perdikaris, *et al.* [202], Eq. (4.26) will be enforced via the PINN's loss function to account for the blunted (non-parabolic) velocity profiles of dense suspensions. However, we will not enforce no-slip boundary conditions with Eq. (4.26) because experiments [216]–[218] suggest that dense suspensions can slip along the channel walls (see Fig. 4.3). The proposed machine learning methodology naturally

handles slip without further effort. To calculate G^* from the experimental data, Eq. (4.26) is integrated from $y^* = 0$ to $y^* = 1$ and rearranged, yielding

$$G^* = \frac{u^*(1) - u^*(0)}{\int_0^1 y^*/\eta_r(\phi)\, dy^*}, \tag{4.27}$$

which is evaluated using the experimental u^* and ϕ profiles and the trapezoidal rule for the integral.

For a strongly Brownian suspension ($Pe = \mathcal{O}(1)$), as we will discuss in Sect. 4.4.3, the velocity profile in experiments [219] is indistinguishable from a parabolic one, so instead of Eq. (4.26), we can simply enforce

$$u^*(y^*) = 1 - y^{*2}. \tag{4.28}$$

Put differently: now $\eta_r(\phi) \approx 1$, $u^*(1) = 0$ (the dilute suspension does not slip), and the scale $U_{\max}$ is chosen to make $G^* = -2$ in this case, consistent with Eq. (4.27).

4.4.2 Non-Brownian dense suspension

PINN loss function

In a non-Brownian dense suspension, the Brownian diffusive flux $\boldsymbol{N}_B$ can be neglected in Eq. (4.3), which eliminates the term $Pe^{-1} d\phi/dy^*$ from Eq. (4.22) (equivalently, the limit $Pe \to \infty$ corresponds to a non-Brownian suspension). Then, in this case, the MSE terms as introduced in Eq. (4.5) in Sect. 4.2 are now be implemented as:

$$\mathrm{MSE}_u = \frac{1}{N}\sum_{i=1}^{N} |u^* - u^*_{\mathrm{train}}|^2, \tag{4.29a}$$

$$\mathrm{MSE}_\phi = \frac{1}{N}\sum_{i=1}^{N} |\phi - \phi_{\mathrm{train}}|^2, \tag{4.29b}$$

$$\mathrm{MSE}_p = \frac{1}{N}\sum_{i=1}^{N} \left| \frac{K_c}{K_\eta}\phi \left(\phi \frac{d^2u^*}{dy^{*2}} + \frac{du^*}{dy^*}\frac{d\phi}{dy^*} \right) + \frac{du^*}{dy^*}\frac{\phi^2}{\eta_r}\frac{d\eta_r}{dy^*} \right|^2, \tag{4.29c}$$

$$\mathrm{MSE}_m = \frac{1}{N}\sum_{i=1}^{N} \left| \eta_r(\phi)\frac{du^*}{dy^*} - G^* y^* \right|^2, \tag{4.29d}$$

$$\mathrm{MSE}_c = \left| \int_0^1 \phi(y^*) dy^* - \phi_b \right|^2 . \tag{4.29e}$$

Appendix 4.A.1 describes how the experimental data (digitized from [216]) was pre-processed into training data.

Note that in MSE_p, $d\eta_r/dy^*$ is calculated by the chain rule: $d\eta_r/dy^* = (d\eta_r/d\phi)(d\phi/dy^*)$. Then, substituting η_r from Eq. (4.9) into the loss function, we obtain $\mathscr{L}$, which depends only on the NN weights ($\mathbf{\Theta}_u$ and $\mathbf{\Theta}_\phi$) and the ratio K_c/K_η. By minimizing the resulting $\mathscr{L}(\mathbf{\Theta}_u, \mathbf{\Theta}_\phi, K_c/K_\eta)$ with respect to its arguments using $w_u = w_\phi = w_p = w_m = w_c = 1$, we find the value of K_c/K_η that simultaneously leads to the best agreement with the training data *and* the physics.

Comparison between PINN, theory and experiment

We can solve for the "theoretical" prediction for ϕ from Eq. (4.22). For a non-Brownian suspensions, the dependence of the viscosity on the particle volume fraction is given by Eq. (4.9), and the velocity profile obeys Eqs. (4.26). Substituting these expressions into Eq. (4.22) and neglecting the Brownian term ($Pe \to \infty$), we once again obtain a nonlinear first-order ODE for $\phi(y^*)$:

$$\frac{d\phi}{dy^*} = \frac{\phi}{\left[(1 - K_\eta/K_c)\, a(\phi/\phi_m)\, (1 - \phi/\phi_m)^{-1} - 1\right] y^*}, \tag{4.30}$$

Similar to the result in Sect. 4.3.3, Koh, Hookham, and Leal [216] assumed $K_c/K_\eta = 0.66$. Then, Eq. (4.30) can be integrated numerically from $y^* = 1$ back to $y^* = 0$ (to handle the singularity at $y^* = 0$). An arbitrary value $\phi(y^* = 1) = \phi_w \in [0, 1]$ is used as an initial guess. Then, a nonlinear iteration (implemented using `optimize.root_scalar` from the SciPy stack in Python [168]) updates ϕ_w until the constrain (4.24) is satisfied for the given ϕ_b. This solution will be shown as the "theory" curve in the figures below.

In Fig. 4.3, 4.4, 4.5 we compare the PINN solutions to the laser-Doppler velocimetry experimental measurements of Koh, Hookham, and Leal [216] at $\phi_b = 0.1, 0.2, 0.3$, respectively. As in Sect. 4.3.1, we use the scaled viscosity function $\eta_r(\phi)$ given in Eq. (4.9), because

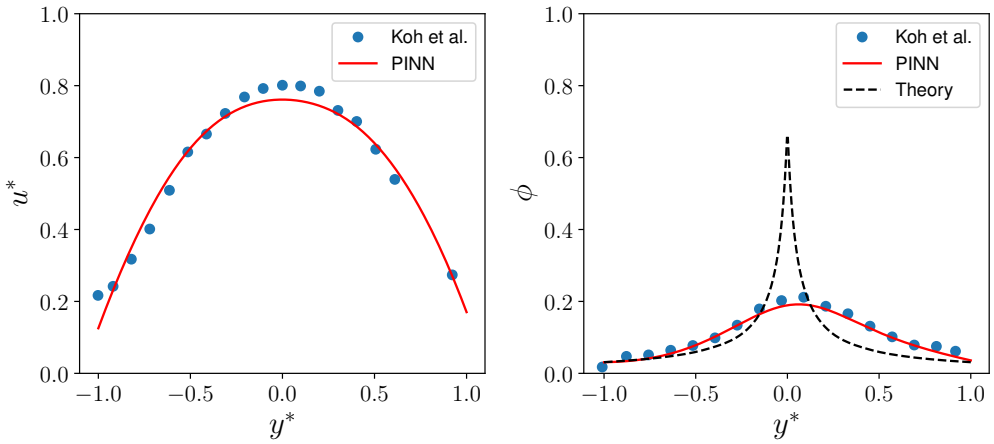

Figure 4.3. Application of the proposed PINN-based approach to experiment 187 from Koh, Hookham, and Leal [216] at $\phi_b = 0.1$ and $G^* = -1.51$. The PINN found $K_c/K_\eta = 0.10 \pm 0.012$.

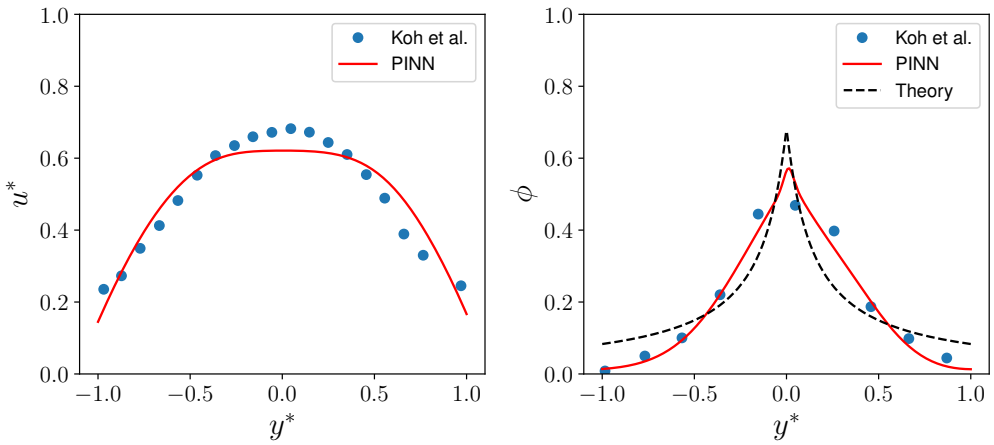

Figure 4.4. Application of the proposed PINN-based approach to experiment 189 from Koh, Hookham, and Leal [216] at $\phi_b = 0.2$ and $G^* = -1.22$. The PINN found $K_c/K_\eta = 0.44 \pm 0.018$.

their experiments are also for a neutrally buoyant non-Brownian suspension at low Reynolds number, like [118]. As can be deduced from the figures, the PINN predictions for the profiles $u^*(y^*)$ and $\phi(y^*)$ agree well with the experiment data. Specifically, the PINN predicts ϕ better than pure theory from Eq. (4.30) because, when using Eq. (4.30) as a constraint on the learning process, the PINN "smooths out" the physically-questionable singularity of the ODE at $y^* = 0$. Note that this feature of the PINN approach was also mentioned in [202],

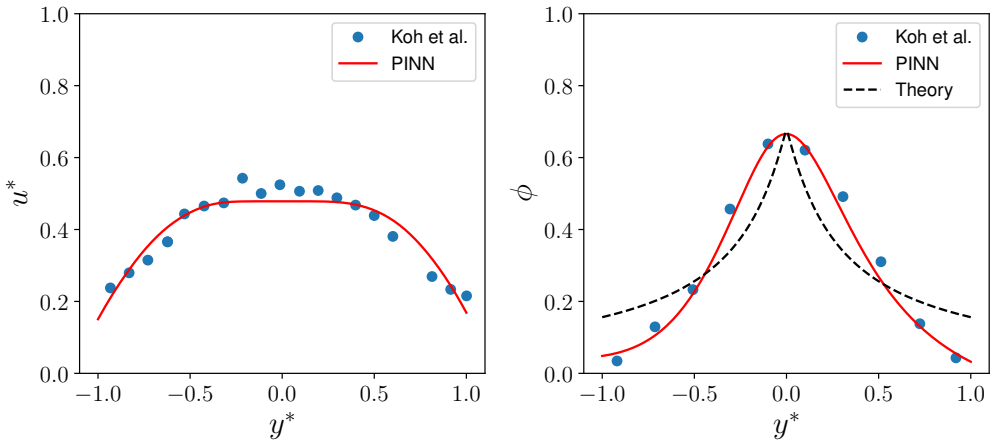

Figure 4.5. Application of the proposed PINN-based approach for to experiment 192 from Koh, Hookham, and Leal [216] at $\phi_b = 0.3$ and $G^* = -1.04$. The PINN found $K_c/K_\eta = 0.58 \pm 0.020$.

in the context of the shear stress singularity at the channel centerline under a power-law rheological model.

Table 4.1. Values of the shear-induced migration model's parameter K_c/K_η, as inferred by the PINN from non-Brownian experimental data of Koh, Hookham, and Leal [216], for different bulk volume fractions ϕ_b. As before, these statistical results, with a mean and a standard error, come from 100 runs of the PINN algorithm using different random initializations of the NNs.

ϕ_b	K_c/K_η
0.1	0.10 ± 0.012
0.2	0.44 ± 0.018
0.3	0.58 ± 0.020

Importantly, by training the PINN, we deduce best-fit K_c/K_η values *different* from the traditional value of 0.66, which has only been validated for the concentric Couette flow (Sec. 4.3.3). Table 4.1 summarizes the values that the PINN "learns" from experimental data with different values of ϕ_b for the Poiseuille flow in a slot.

4.4.3 Brownian suspension

Now, we return to the "full" Eq. (4.22) at finite Pe, which was defined in Eq. (4.23). Now, it is expected that $\eta/\eta_s = \eta_r(\phi, Pe)$ [191] (see also [20, Ch. 7]), while the suspension is

still neutrally buoyant, at steady state and at low Reynolds number. (The geometry is still that of Poiseuille flow in a slot as introduced in Sect. 4.4.2.)

Unlike the previous sections, we can no longer use the Krieger–Dougherty viscosity function from Eq. (4.9) for the Brownian suspension. Instead, motivated by the work of Kang and Mirbod [144], we take the Brownian suspension's shear viscosity to be

$$\eta_r(\phi, Pe) = \eta_\infty(\phi) + \frac{\eta_0(\phi) - \eta_\infty(\phi)}{1 + K_{Pe}\eta_s a_p^3 \dot{\gamma}/(k_B T)} = \eta_\infty(\phi) + \frac{\eta_0(\phi) - \eta_\infty(\phi)}{1 + K_{Pe} Pe \dot{\gamma}^*/(6\pi)}, \tag{4.31}$$

where

$$\eta_0(\phi) = (1 - \phi/\phi_{m_0})^{-\mathfrak{a}_0}, \tag{4.32a}$$

$$\eta_\infty(\phi) = (1 - \phi/\phi_{m_\infty})^{-\mathfrak{a}_\infty}, \tag{4.32b}$$

based on the correlations proposed by Kruif, Iersel, Vrij, *et al.* [220]. Typically, $\phi_{m_0} = 0.63$, $\phi_{m_\infty} = 0.71$, $\mathfrak{a}_0 = 1.96$, $\mathfrak{a}_\infty = 1.93$, and $K_{Pe} = 1.31$ are used in the literature [144] based on experimental fits. While the zero-Pe and infinite-Pe "plateaus" of the viscosity function (4.31) can be measured accurately (yielding the maximum volume fractions ϕ_{m_0} and ϕ_{m_∞}, along with the exponents $\mathfrak{a}_0$ and $\mathfrak{a}_\infty$), the transition over intermediate Pe is characterized by the dimensionless parameter K_{Pe}. This parameter is harder to infer from a single experiment (and, indeed, has *not* been reported in the papers on shear-induced migration of Brownian particles), thus we propose to treat it as *a priori* unknown, like K_c and K_η. In other words, we will self-consistently determine the unknown K_{Pe} via the inverse formulation in the PINN approach applied to experiments on shear-induced migration of Brownian suspensions.

Observe that we keep the (dimensionless, recall Eq. (4.21)) variable local shear rate $\dot{\gamma}^* = \dot{\gamma}^*(y^*) = du^*/dy^*$ in Eq. (4.31); $\dot{\gamma}^* \neq const.$ in Poiseuille flow. Nevertheless, using particle-image velocimetry, Frank, Anderson, Weeks, *et al.* [219] found experimentally that the velocity profile of a Brownian suspension flowing through a rectangular channel only slightly deviates from the parabolic profile of the solvent (see Fig. 4.6), hence $\dot{\gamma}^*(y^*) \approx -2y^*$.

Therefore, we shall use the parabolic profile from Eq. (4.28) to define MSE_m in the loss function, instead of the full momentum equation, for the Brownian suspensions.

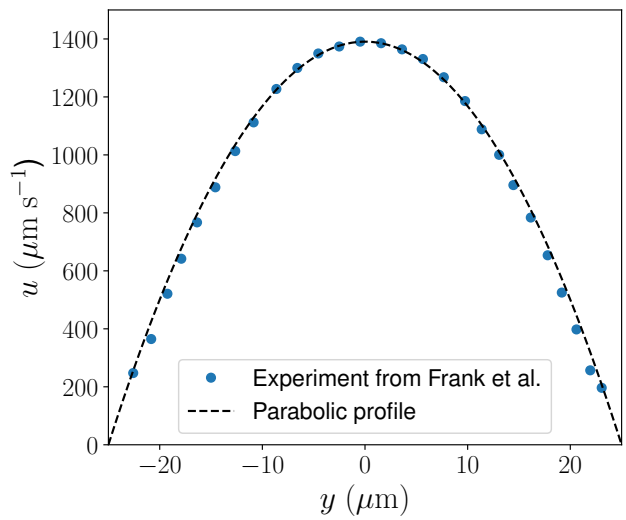

Figure 4.6. Measured axial velocity of a Brownian suspension in Poiseuille flow reproduced from Frank, Anderson, Weeks, *et al.* [219] is compared to a dimensional version of the parabolic profile from Eq. (4.28), showing good agreement. The channel width is $2H = 50$ µm, and $U_{\max} \approx 1391$ µm s^{-1} from the figure in [219].

PINN loss function

For the Brownian suspension, the MSE terms is as introduced in Eq. (4.5) in Sect. 4.2 are now implemented as:

$$\mathrm{MSE}_u = \frac{1}{N}\sum_{i=1}^{N} |u^* - u^*_{\mathrm{train}}|^2, \tag{4.33a}$$

$$\mathrm{MSE}_\phi = \frac{1}{N}\sum_{i=1}^{N} |\phi - \phi_{\mathrm{train}}|^2, \tag{4.33b}$$

$$\mathrm{MSE}_p = \frac{1}{N}\sum_{i=1}^{N} \left| K_c\phi\left(\phi\frac{d^2u^*}{dy^{*2}} + \frac{du^*}{dy^*}\frac{d\phi}{dy^*}\right) + K_\eta\frac{du^*}{dy^*}\frac{\phi^2}{\eta_r}\frac{d\eta_r}{dy^*} + \frac{1}{Pe}\frac{d\phi}{dy^*}\right|^2, \tag{4.33c}$$

$$\mathrm{MSE}_m = \frac{1}{N}\sum_{i=1}^{N} \left|u^* - 1 + y^{*2}\right|^2, \tag{4.33d}$$

$$\mathrm{MSE}_c = \left|\int_0^1 \phi(y^*)\,dy^* - \phi_b\right|^2. \tag{4.33e}$$

Appendix 4.A.1 describes how the experimental data (digitized from [219]) was pre-processed into training data.

Using η_r from Eq. (4.31), we can calculate $d\eta_r/dy^* = (d\eta_r/d\phi)(d\phi/dy^*)$ in Eq. (4.33c) by the chain rule. Now, the loss $\mathscr{L}$ (recall Eq. (4.5)) depends only on the neural network weights ($\mathbf{\Theta}_u$ and $\mathbf{\Theta}_\phi$) and the unknown model parameters K_c, K_η, and K_{Pe}. By minimizing the resulting $\mathscr{L}(\mathbf{\Theta}_u, \mathbf{\Theta}_\phi, K_c, K_\eta, K_{Pe})$ using $w_u = w_\phi = w_p = w_m = w_c = 1$, with respect to its arguments, we find suitable NN weights and values of the parameters K_c, K_η, and K_{Pe} that simultaneously lead to the best agreement with the training data *and* the physics.

Comparison between PINN, theory and experiment

For Brownian suspensions, we substitute the parabolic velocity profile from Eq. (4.28) and the Brownian suspension viscosity from Eq. (4.31) into Eq. (4.22), to again obtain a nonlinear first-order ODE for $\phi(y^*)$:

$$\frac{d\phi}{dy^*} = \frac{2K_c\phi^2\eta_r + 2y^*K_\eta\phi^2 f_2(\phi)}{(Pe^{-1} - 2K_c y^*\phi)\eta_r - 2y^*K_\eta\phi^2 f_1(\phi)}, \tag{4.34}$$

where

$$\begin{aligned} f_1(\phi) &= \frac{d\eta_\infty}{d\phi} + \frac{d\eta_0/d\phi - d\eta_\infty/d\phi}{1 + K_{Pe}Pe\, y^*/(3\pi)}, \\ &= \frac{\mathfrak{a}_0}{\phi_{m_0}}\left(1 - \frac{\phi}{\phi_{m_0}}\right)^{-\mathfrak{a}_0-1} + \frac{(\mathfrak{a}_0/\phi_{m_0})(1-\phi/\phi_{m_0})^{-\mathfrak{a}_0-1} - (\mathfrak{a}_\infty/\phi_{m_\infty})(1-\phi/\phi_{m_\infty})^{-\mathfrak{a}_\infty-1}}{1 + K_{Pe}Pe\, y^*/(3\pi)}, \end{aligned} \tag{4.35a}$$

$$f_2(\phi) = -[\eta_0(\phi) - \eta_\infty(\phi)]\frac{K_{Pe}Pe/(3\pi)}{[1 + K_{Pe}Pe\, y^*/(3\pi)]^2}. \tag{4.35b}$$

Using the numerical procedure described in Sect. 4.4.2, we solve for the "theory" prediction for $\phi(y^*)$ from Eqs. (4.34) and (4.24), using the values for K_c and K_η in Eq. (4.34) and K_{Pe} in Eq. (4.35) obtain by PINN.

The comparisons between the experimental data of Frank, Anderson, Weeks, *et al.* [219] (symbols), the theory (dashed), and the PINN (solid) are shown in Figs. 4.7 and 4.8. The comparisons show that the PINN predictions agree well with experiment data, while the

"theory" solutions do not. With a limited number of discrete observations of u^* and ϕ from the experiments used as training data, the PINN algorithm not only accurately predicts the distributions of $u^*(y^*)$ and $\phi(y^*)$, but also "learns" the suitable values of K_c, K_η, and K_{Pe}, which were *a priori* unknown.

Table 4.2 summarizes the values that the PINN "learns" from experimental data with different values of ϕ_b and Pe. To account for the variations in the converged values of the unknown model parameters, due to the random initialization of the NNs, we averaged the predictions from 100 different initializations to obtain a statistical result with a mean and a standard error. Importantly, the PINN analysis suggests that K_c and K_η vary with ϕ_b and Pe. This important issue was *not* addressed in previous literature, in which the values of K_c and K_η are taken from [118] and applied to any flow scenario (even if the values in [118] were validated only for the concentric Couette flow). Now, however, we discover that K_η (in particular) decreases with Pe. The last result for $Pe = 69$ suggests that a vanishing viscosity-variation flux, $\|\boldsymbol{N}_\eta\| \approx 0$, for this Brownian case of $Pe \not\gg 1$. This result is consistent with the fact that the velocity profile is parabolic (recall Fig. 4.6), and the strongly-Brownian suspension effectively has the same viscosity as the Newtonian carrier fluid. Further, while the values obtained for K_{Pe} in Table 4.2 is on the same order as the value 1.31 used in literature, they are not the same, suggesting that this parameter (quantifying the suspension rheology's shear-dependence) should be measured for each suspension experiment.

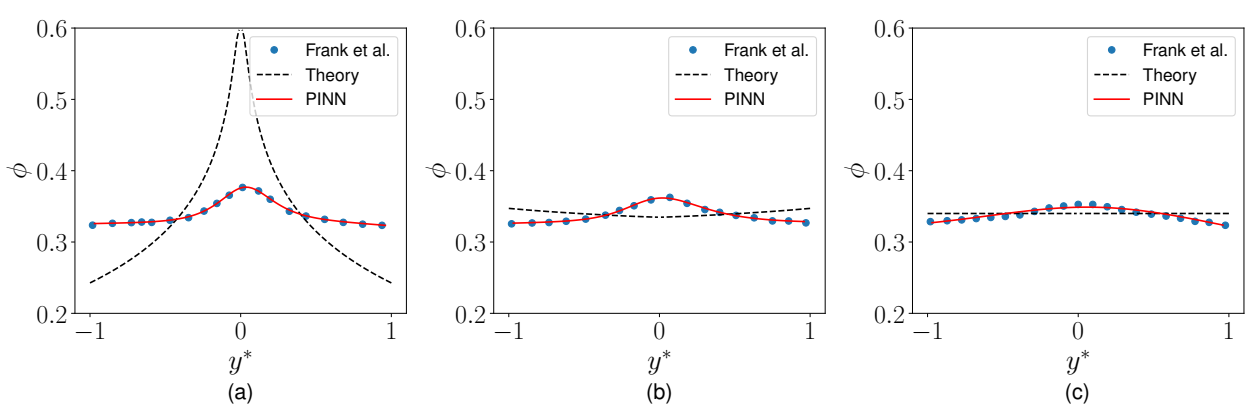

Figure 4.7. Application to experiment from Frank, Anderson, Weeks, *et al.* [219] at $\phi_b = 0.34$: (a) $Pe = 4400$; (b) $Pe = 550$; (c) $Pe = 69$.

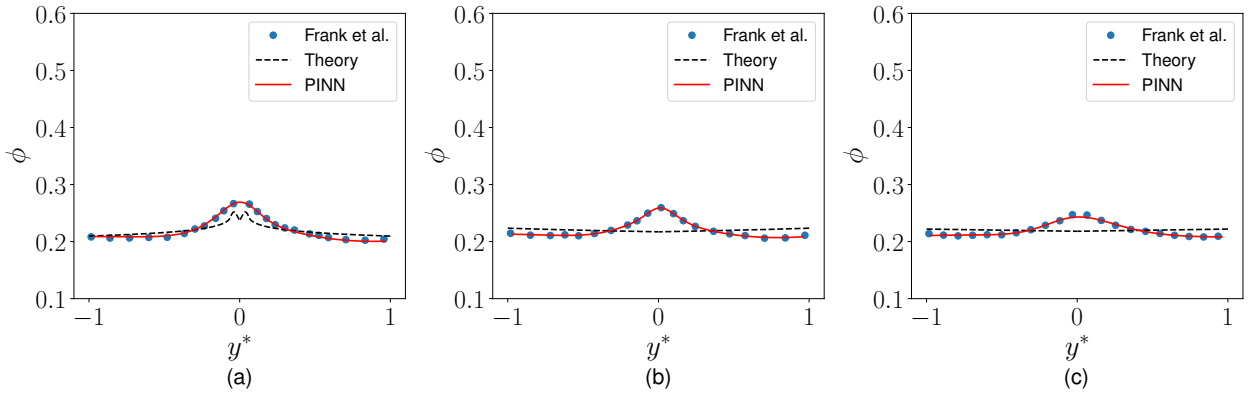

Figure 4.8. Application to experiment from Frank, Anderson, Weeks, *et al.* [219] at $\phi_b = 0.22$: (a) $Pe = 4400$; (b) $Pe = 550$; (c) $Pe = 69$.

Table 4.2. Values of the shear-induced migration model's parameters K_c, K_η, and K_{Pe}, as inferred by the PINN from the experimental data of Frank, Anderson, Weeks, *et al.* [219], for different bulk volume fractions ϕ_b and different values of shear Péclet number Pe. As before, these statistical results, with a mean and a standard error, come from 100 runs of the PINN algorithm using different random initializations of the NNs.

ϕ_b	Pe	K_c	K_η	K_{Pe}
0.34	4400	$2.74 \times 10^{-4} \pm 2.23 \times 10^{-3}$	$8.28 \times 10^{-3} \pm 5.38 \times 10^{-2}$	$1.77 \pm 0.61 \times 10^{-1}$
0.34	550	$7.84 \times 10^{-5} \pm 4.64 \times 10^{-4}$	$6.32 \times 10^{-4} \pm 5.88 \times 10^{-3}$	$1.46 \pm 5.69 \times 10^{-1}$
0.34	69	$2.47 \times 10^{-4} \pm 3.92 \times 10^{-4}$	$3.58 \times 10^{-7} \pm 2.97 \times 10^{-6}$	$1.51 \pm 2.58 \times 10^{-2}$
0.22	4400	$4.17 \times 10^{-4} \pm 1.94 \times 10^{-3}$	$1.21 \times 10^{-2} \pm 7.37 \times 10^{-2}$	$1.71 \pm 4.85 \times 10^{-2}$
0.22	550	$9.98 \times 10^{-5} \pm 9.18 \times 10^{-4}$	$1.61 \times 10^{-3} \pm 1.39 \times 10^{-2}$	$1.47 \pm 1.69 \times 10^{-2}$
0.22	69	$5.73 \times 10^{-4} \pm 7.35 \times 10^{-4}$	$5.51 \times 10^{-7} \pm 7.12 \times 10^{-7}$	$1.51 \pm 1.07 \times 10^{-2}$

Note that the model from Eq. (4.34) breaks down if $d\phi/dy^*$ changes sign at some $y^* \neq 0$. This situation can occur when the denominator in Eq. (4.34) reaches 0. The $\phi(y^*)$ profile develops a seemingly nonphysical maximum on each side of the centerline $y^* = 0$ (see Fig. 4.8(a)). This observation highlights a deficiency of using the Phillips, Armstrong, Brown, *et al.* [118] model for Brownian suspensions. Further, it is important to emphasize that this breakdown of the Brownian shear-induced migration model is unrelated to the fact that the shear rate vanishes at the center of the channel, which is a separate issue addressed by "nonlocal" shear rate modifications to account for the breakdown of the continuum theory at the scale of a single particle diameter [126], [138], [140]. On the other hand, the PINN

approach predicts a smooth curve that agrees with the experimental data because the PINN does not attempt to interpret the model in a point-wise sense (or as a "law of nature," which it is clearly not), but rather uses only its residual to constrain the learning process.

4.5 Conclusion

Thirty years later, the phenomenological model of Phillips, Armstrong, Brown, *et al.* [118] continues to be the "workhorse" of macroscopic modeling of shear-induced particle migration in low-Reynolds-number flows of suspensions, as recent studies on simulation of migration in Brownian suspensions [144] and experiments [145] and simulations [146] on migration in complex fluids demonstrate. However, the model's parameters were only ever properly calibrated against experiments in an annular Couette cell [118]. Subsequent studies on shear-induced migration in Poiseuille flows [216], [219] showed that the model, as calibrated against the annular Couette flow data, is only in *qualitative* agreement with slot-flow experiments (despite being quantitatively accurate for Couette flow). Furthermore, the application of the model to Brownian suspensions [144] showed even worse agreement between "theory" and experiments.

To remedy these apparent contradictions/difficulties exposed in the literature, we proposed to shift the paradigm of how such a phenomenological model should be used. In this chapter, we employed a machine learning methodology in which the Phillips, Armstrong, Brown, *et al.* [118] model is used constrain a machine learning approach to assimilating the experimental data on particle migration. Using the idea of physics-informed neural networks (PINNs) pioneered by Karnidakis and collaborators [148], [197], we constructed a loss function from the Phillips, Armstrong, Brown, *et al.* [118] model and optimized neural networks to simultaneously best-approximate velocity and volume fraction experimental data, as well as the unknown/phenomenological parameters in the model. The PINN approach seamlessly identified the unknown parameters in the model as part of the training process. In doing so, we found that the parameter values calibrated for annular Couette flow data are not accurate for other flow scenarios, such as Poiseuille flow and/or for a Brownian suspension. Additionally, the model's parameters were found to vary with the bulk volume fraction and

the shear Péclet number of the suspension, which was not previously established for this model (though the Péclet dependence was observed in experiments [219], and in the suspension balance model discussed therein). This point was particularly important for the case of Brownian suspensions, highlighting why the phenomenological model solved as "basic law" with the parameters from [118] (as done in [144]) could not match any of the experimental data.

In summary, we proposed to shift the paradigm of how phenomenological models for shear-induced migration should be used. The models widely used in the literature are only *post*dictive, requiring calibration against an experiment for each flow scenario they are to be used in. Even then, attempting to solve the models as a "basic law" to predict the particle distribution (having somehow best-fit the parameters) requires overcoming unphysical singularities. On the other hand, employing the models within the PINN approach does not require pointwise solutions or the parameters to be known *a priori*. Therefore, their values and, thus, the true relative importance of the different particle migration fluxes (collisional, viscosity-gradient or Brownian) in a given experiment can be uncovered via PINNs (but not via the standard approach in the literature, based on directly solving an ODE for the particle distribution). It should be re-emphasized that using the parameter values (calibrated in 1992 only for annular Couette flow) in varied flow scenarios strongly enforces physics that *may or may not* be manifested in the particular flow under consideration. We have demonstrated that, to gain an understanding of the "unknown physics" (to use the terminology of Reyes, Howard, Perdikaris, *et al.* [202]) of particle migration in a variety of flow experiments, PINNs can be effectively employed to simultaneously solve the inverse and forward problems and to significantly extend the practical utility of the standard phenomenological models.

4.A Appendix

4.A.1 Pre-processing of experimental data into training data

For training of the NNs, we utilize the experimental data from the literature. Specifically, we digitized the data from Fig. 7 of Ref. [118], Figs. 10, 11, 15, and 19 of Ref. [216], and Figs. 3 and 4 of Ref. [219]. Experimental data points in these figures are limited (approximately

20 points in each plot). The NNs need more data points to achieve successful training (approximately 50 times the number of weights [221]). Thus, assuming the particle migration profiles and suspension velocities are smooth functions, we use interpolation to generate more data samples for the training of the NNs from the limited experimental data points. Specifically, we use `interpolate.interp1d` from the SciPy stack in Python [168] to obtain values at sample points that are not part of the digitized experimental data.

4.A.2 Choice of number of hidden layers and neurons per layer

To attempt to find an optimal number of hidden layers and nodes per layer (and justify the choices made for the PINN architecture used in the main text), we plot the training error for different numbers of hidden layers, as shown in Fig. 4.9. We first train the PINNs for $10,000$ iterations using the "Adam" [212] optimizer, then we use the "L-BFGS-B" optimizer until convergence. Figure 4.9 shows that adding layers (and/or more neurons per layer) does not reduce the training error further, while this action leads to a significantly higher computational cost (and requires more computing resources for the training process to reach convergence). Fewer layers (and/or fewer neurons per layer) tends to lead to divergence, i.e., failure of the training process. Therefore, as a suitable trade-off, we use 2 hidden layers with 10 neurons in each layer in the NNs for PINN approach.

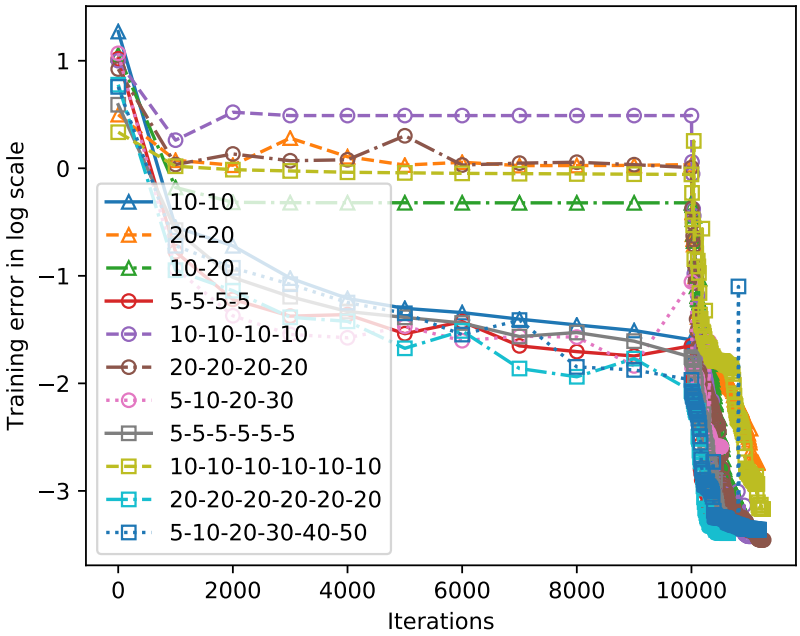

Figure 4.9. Training errors from PINNs with different numbers of hidden layers, and different number of neurons in each layer, in the NN architecture. The labels represent the layers and number of neurons per layer.

5. SUMMARY AND OUTLOOK

This chapter summarizes the main accomplishments of this thesis and presents avenues for future work.

5.1 Thesis summary

In this thesis, we have analyzed, through mathematical calculations, computational simulations, and machine learning, the fluid dynamics related to three topics inspired by multiphase flows relevant to hydraulically fractured flow passages: fluid–fluid interfacial instabilities, flow-wise variations of the hydraulic conductivity, and shear-induced particle migration in suspensions. Specifically, the chapter-wise accomplishments of this thesis are:

- **Chapter 2:** We formulated a three-regime theory to describe the interfacial instability of immiscible displacement in tapered passages (Hele-Shaw cells): (i) in Regime I, the growth rate of perturbations to the flat interface is always negative, thus the interface is stable; (ii) in Regime II, the growth rate of perturbations remains zero (parallel cells), changes from negative to positive (converging cells), or from positive to negative (diverging cells), thus the interface stability possibly changes type at some location in the cell; (iii) in Regime III, the growth rate of perturbations is always positive, thus the interface is unstable, leading to "finger" formation. We conducted three-dimensional direct numerical simulations (using the inteFoam solver from OpenFOAM®) to validate the proposed theory and to further explore the effect of the depth gradient (taper) on the interfacial instability. In doing so, we demonstrated that the depth gradient has only a slight influence in Regime I, and its effect is most pronounced in Regime III.

- **Chapter 3:** We derived an expression for the flow-wise variation of the hydraulic conductivity inside a non-uniformly shaped fracture with permeable walls. This analytical result highlights the effects of geometric variation (through the local slope of the aperture's flow-wise variation), the permeability of the walls (through a dimensionless slip coefficient), and the effect of flow inertia (through a Reynolds number). Among these factors, we found that the geometric variation (specifically, the resistance to flow

induced by the narrowing of a fracture) dominates the conductivity change, even for slow shape variation (small slopes). We validated the theory against an OpenFOAM® solver for the Navier–Stokes equations subject to a tensorial slip boundary condition.

- **Chapter 4:** We harnessed the physics-informed neural networks (PINNs) approach to extend the utility of phenomenological models for particle migration in shear flow. Using the PINN approach, we identified the unknown parameters in the empirical model through the inverse solver capability of PINNs. Specifically, we discovered that the model's parameters' values are significantly different in different flow regimes. For example the parameter values for Poiseuille flow do not match those for a concentric Couette flow. This result highlights an inconsistency in the literature, wherein the concentric Couette flow values are used for Poiseuille flow. Importantly, we found that the inferred values of the empirical model's parameters vary with the shear Péclet number and the particle bulk volume fraction of the suspension, instead of being constant as assumed in previous literature. In doing so, we demonstrated that the phenomenological model for shear migration is more useful as a constraint on a machine learning process, than a stand-alone "basic law."

5.2 Future work

In future work on the Saffman–Taylor (viscous fingering) instability, our analytical flow solution in Chapter 3 could be used to revisit the effect of wall permeation on the interfacial instability in angled Hele-Shaw cells. It is also of interest to study the effect of particle migration on the interfacial instability. Previous research [73], [75], [222] has found that viscous fingering of suspensions is strongly dependent on the particle volume fraction in the fluid: the suspended particles delay the onset of instability but accelerate a finger's growth rate once instability is triggered [75]. Xu, Kim, and Lee [73] hypothesized that the instability is caused by shear-induced migration and particle accumulation at the interface. Therefore, future work on the interaction between shear-induced particle migration and interfacial instabilities in angled Hele-Shaw cells can start by combining the models and results from Chapters 2 and 4.

In Chapter 3 we derived an analytical solution for the hydraulic conductivity inside a non-uniformly shaped fracture with permeable walls. In future work, the analytical solutions derived could be used to improve systems-level (network) modelling of hydraulically fractured reservoirs [223], in which the Darcy conductivity of each non-uniform passage must be accurately accounted for, throughout the fractured porous rock. Currently, only simple modifications of Darcy's law are used to capture the geometric variation and wall permeability [224]. As mentioned in Chapter 3, our analysis is easily applied to fractures with other (more complex but still "slow") types of geometric variations, such those considered in [92].

In Chapter 4 we harnessed physics-informed neural networks (PINNs) to understand particle migration in shear flow. Despite the success of the proposed PINN approach, we have found that it faces challenges in convergence during training. Our results indicate that, the training of the neural network might fail when the optimization procedure diverges (or converges to a local minimum) for different random initializations, which is a well known problem [210]. Although the Adam and BFGS optimizers have been used in succession to mitigate the local minimum issue, it still remains unclear how to guarantee that the optimization process on the networks' weights converges to a global minimum. In future work, further effort can be put in this direction. For example, a transfer learning technique may be worth exploring: first train a network solving a related problem, then initialize the network we intend to train with those fully trained weights and biases. Beyond improving the PINN training process, the proposed approach could also be applied to shear-induced migration in non-Newtonian fluids, along the lines of the phenomenological model of Hernández [146].

REFERENCES

[1] T. D. van Golf-Racht, *Fundamentals of Fractured Reservoir Engineering*, 1st, ser. Developments in Petroleum Science. Amsterdam, The Netherlands: Elsevier Scientific Publishing Company, 1982, vol. 12. DOI: 10.1016/S0376-7361(08)70330-3.

[2] J. McBride and M. Aly Sergie, "Hydraulic Fracturing (Fracking)," Council on Foreign Relations, Tech. Rep., 2015. [Online]. Available: https://www.cfr.org/backgrounder/hydraulic-fracturing-fracking.

[3] C. H. Yew and X. Weng, *Mechanics of Hydraulic Fracturing*, 2nd ed. Waltham, MA: Gulf Professional Publishing, 2015. DOI: 10.1016/C2013-0-12927-3.

[4] A. C. Barbati, J. Desroches, A. Robisson, and G. H. McKinley, "Complex fluids and hydraulic fracturing," *Annu. Rev. Chem. Biomol. Eng.*, vol. 7, pp. 415–453, 2016. DOI: 10.1146/annurev-chembioeng-080615-033630.

[5] E. Detournay, "Mechanics of hydraulic fractures," *Annu. Rev. Fluid Mech.*, vol. 48, pp. 311–339, 2016. DOI: 10.1146/annurev-fluid-010814-014736.

[6] A. A. Osiptsov, "Fluid mechanics of hydraulic fracturing: A review," *J. Petrol. Sci. Eng.*, vol. 156, pp. 513–535, 2017. DOI: 10.1016/j.petrol.2017.05.019.

[7] A. Muggeridge, A. Cockin, K. Webb, *et al.*, "Recovery rates, enhanced oil recovery and technological limits," *Phil. Trans. R. Soc. A*, vol. 372, p. 20 120 320, 2014. DOI: 10.1098/rsta.2012.0320.

[8] M. J. Economides and K. G. Nolte, *Reservoir Stimulation*, 3rd. John Wiley & Sons, 2000.

[9] J. D. Hyman, J. Jiménez-Martínez, H. S. Viswanathan, *et al.*, "Understanding hydraulic fracturing: a multi-scale problem," *Phil. Trans. R. Soc. A*, vol. 374, p. 20 150 426, 2016. DOI: 10.1098/rsta.2015.0426.

[10] C. H. Yew and X. Weng, "Proppant transport in a 3D fracture," in *Mechanics of Hydraulic Fracturing*, 2nd ed., Waltham, MA: Elsevier, 2015, ch. 3, pp. 49–68. DOI: 10.1016/B978-0-12-420003-6.00003-3.

[11] S. Rassenfoss, "What Do Fractures Look Like? A Picture Says A Lot, Even When It is Wrong," *J. Petrol. Tech.*, vol. 67, no. 5, pp. 60–68, 2015. DOI: 10.2118/0515-0060-JPT.

[12] O. M. Phillips, *Flow and Reactions in Permeable Rocks*. New York, NY: Cambridge University Press, 1991.

[13] M. Vincent, "Proving It - A Review of 80 Published Field Studies Demonstrating the Importance of Increased Fracture Conductivity," in *SPE Annual Technical Conference and Exhibition*, San Antonio, Texas: SPE, Sep. 2002, SPE-77675–MS. DOI: 10.2118/77675-MS.

[14] R. Mohais, C. Xu, P. A. Dowd, and M. Hand, "Permeability correction factor for fractures with permeable walls," *Geophys. Res. Lett.*, vol. 39, p. L03403, 2012. DOI: 10.1029/2011GL050519.

[15] R. Mohais, C. Xu, P. A. Dowd, and M. Hand, "Enhanced Geothermal Systems," in *Alternative Energy and Shale Gas Encyclopedia*, ser. Wiley Series on Energy, J. H. Lehr, J. Keeley, and T. B. Kingery, Eds., Hoboken, NJ: Wiley, 2016, ch. 27, pp. 265–289. DOI: 10.1002/9781119066354.ch27.

[16] P. Olasolo, M. C. Juárez, M. P. Morales, S. D'Amico, and I. A. Liarte, "Enhanced geothermal systems (EGS): A review," *Renew. Sust. Energ. Rev.*, vol. 56, pp. 133–144, 2016. DOI: 10.1016/j.rser.2015.11.031.

[17] P. Koumoutsakos, I. Pivkin, and F. Milde, "The fluid mechanics of cancer and its therapy," *Annu. Rev. Fluid Mech.*, vol. 45, pp. 325–355, 2013. DOI: 10.1146/annurev-fluid-120710-101102.

[18] D. J. McClements, *Food Emulsions: Principles, Practices, and Techniques*, 3rd. Boca Raton, FL: CRC Press, 2015. DOI: 10.1201/b18868.

[19] K. Armstrong, R. Card, R. Navarrete, *et al.*, "Advanced fracturing fluids improve well economies," *Oilfield Review*, vol. 7, no. 3, pp. 34–51, 1995.

[20] É. Guazzelli and J. F. Morris, *A Physical Introduction to Suspension Dynamics*. Cambridge: Cambridge University Press, 2011. DOI: 10.1017/CBO9780511894671.

[21] D. Vigolo, S. Radl, and H. A. Stone, "Unexpected trapping of particles at a T junction," *Proc. Natl Acad. Sci. USA*, vol. 111, pp. 4770–4775, 2014. DOI: 10.1073/pnas.1321585111.

[22] N. Y. C. Lin, S. Goyal, X. Cheng, R. N. Zia, F. A. Escobedo, and I. Cohen, "Far-from-equilibrium sheared colloidal liquids: Disentangling relaxation, advection, and shear-induced diffusion," *Phys. Rev. E*, vol. 88, p. 62 309, 2013. DOI: 10.1103/PhysRevE.88.062309.

[23] PetroWiki, *Fracturing fluids and additives*, 2018. [Online]. Available: http://petrowiki.org/Fracturing_fluids_and_additives.

[24] C. H. Bivins, C. Boney, C. Fredd, *et al.*, "New fibers for hydraulic fracturing," *Oilfield Review*, vol. 17, no. 2, pp. 34–43, 2005.

[25] Z. P. Bažant, M. Salviato, V. T. Chau, H. Viswanathan, and A. Zubelewicz, "Why fracking works," *ASME J. Appl. Mech.*, vol. 81, p. 101 010, 2014. DOI: 10.1115/1.4028192.

[26] A. Guha, "Transport and deposition of particles in turbulent and laminar flow," *Annu. Rev. Fluid Mech.*, vol. 40, pp. 311–341, 2008. DOI: 10.1146/annurev.fluid.40.111406.102220.

[27] S. Rassenfoss, "Rethinking proppant: From liquid to solid," *J. Petrol. Tech.*, vol. 67, no. 4, pp. 58–59, 2015. DOI: 10.2118/0415-0058-JPT.

[28] PetroWiki, *Hydraulic fracturing*, 2018. [Online]. Available: http://petrowiki.org/Hydraulic_fracturing.

[29] S. Rassenfoss, "Electromagnetic imaging offers first look at the propped rock," *J. Petrol. Tech.*, vol. 68, no. 3, pp. 32–40, 2016. DOI: 10.2118/0316-0032-JPT.

[30] B. Chen, B. R. Barboza, Y. Sun, *et al.*, "A Review of Hydraulic Fracturing Simulation," *Arch. Comput. Methods Eng.*, to appear, 2021. DOI: 10.1007/s11831-021-09653-z.

[31] S. Hill, "Channeling in packed columns," *Chem. Eng. Sci.*, vol. 1, pp. 247–253, 1952. DOI: 10.1016/0009-2509(52)87017-4.

[32] P. G. Saffman and G. Taylor, "The penetration of a fluid into a porous medium or Hele-Shaw cell containing a more viscous liquid," *Proc. R. Soc. Lond. A*, vol. 245, pp. 312–329, 1958. DOI: 10.1098/rspa.1958.0085.

[33] P. G. Saffman, "Viscous fingering in Hele-Shaw cells," *J. Fluid Mech.*, vol. 173, pp. 73–94, 1986. DOI: 10.1017/S0022112086001088.

[34] R. L. Chuoke, P. van Meurs, and C. van der Poel, "The instability of slow, immiscible, viscous liquid-liquid displacements in permeable media," *Petroleum Transactions, AIME*, vol. 216, pp. 188–194, 1959. DOI: 10.2118/1141-G.

[35] H. S. Hele-Shaw, "The flow of water," *Nature*, vol. 58, no. 1489, pp. 34–36, May 1898. DOI: 10.1038/058034a0.

[36] G. M. Homsy, "Viscous fingering in porous media," *Annu. Rev. Fluid Mech.*, vol. 19, pp. 271–311, 1987. DOI: 10.1146/annurev.fl.19.010187.001415.

[37] R. L. Panton, *Incompressible flow*, 4th. Hoboken, NJ: John Wiley & Sons, 2013. DOI: 10.1002/9781118713075.

[38] K. G. Libbrecht, "The physics of snow crystals," *Rep. Prog. Phys.*, vol. 68, pp. 855–895, 2005. DOI: 10.1088/0034-4885/68/4/R03.

[39] J. S. Langer, "Instabilities and pattern formation in crystal growth," *Rev. Mod. Phys.*, vol. 52, pp. 1–28, 1980. DOI: 10.1103/RevModPhys.52.1.

[40] M. E. Glicksman, S. R. Coriell, and G. B. McFadden, "Interaction of flows with the crystal-melt interface," *Annu. Rev. Fluid Mech.*, vol. 18, pp. 307–335, 1986. DOI: 10.1146/annurev.fl.18.010186.001515.

[41] R. Govindarajan and K. C. Sahu, "Instabilities in viscosity-stratified flow," *Annu. Rev. Fluid Mech.*, vol. 46, pp. 331–353, 2014. DOI: 10.1146/annurev-fluid-010313-141351.

[42] S. Michalland, M. Rabaud, and Y. Couder, "Instabilities of the upstream meniscus in directional viscous fingering," *J. Fluid Mech.*, vol. 312, pp. 125–148, 1996. DOI: 10.1017/S0022112096001942.

[43] S. J. Weinstein and K. J. Ruschak, "Coating flows," *Annu. Rev. Fluid Mech.*, vol. 36, pp. 29–53, 2004. DOI: 10.1146/annurev.fluid.36.050802.122049.

[44] A. Juel, D. Pihler-Puzović, and M. Heil, "Instabilities in blistering," *Annu. Rev. Fluid Mech.*, vol. 50, pp. 691–714, 2018. DOI: 10.1146/annurev-fluid-122316-045106.

[45] R. Scardovelli and S. Zaleski, "Direct numerical simulation of free-surface and interfacial flow," *Annu. Rev. Fluid Mech.*, vol. 31, pp. 567–603, 1999. DOI: 10.1146/annurev.fluid.31.1.567.

[46] L. Cueto-Felgueroso and R. Juanes, "Nonlocal interface dynamics and pattern formation in gravity-driven unsaturated flow through porous media," *Phys. Rev. Lett.*, vol. 101, p. 244 504, 2008. DOI: 10.1103/PhysRevLett.101.244504.

[47] S. L. Anna, "Droplets and bubbles in microfluidic devices," *Annu. Rev. Fluid Mech.*, vol. 48, pp. 285–309, 2016. DOI: 10.1146/annurev-fluid-122414-034425.

[48] F. Varela López, L. Pauchard, M. Rosen, and M. Rabaud, "Non-Newtonian effects on ribbing instability threshold," *J. Non-Newtonian Fluid Mech.*, vol. 103, pp. 123–139, 2002. DOI: 10.1016/S0377-0257(01)00165-3.

[49] H. Zhao, J. Casademunt, C. Yeung, and J. V. Maher, "Perturbing Hele-Shaw flow with a small gap gradient," *Phys. Rev. A*, vol. 45, pp. 2455–2462, 1992. DOI: 10.1103/PhysRevA.45.2455.

[50] E. Lajeunesse and Y. Couder, "On the tip-splitting instability of viscous fingers," *J. Fluid Mech.*, vol. 419, pp. 125–149, 2000. DOI: 10.1017/S0022112000001324.

[51] E. O. Dias and J. A. Miranda, "Finger tip behavior in small gap gradient Hele-Shaw flows," *Phys. Rev. E*, vol. 82, p. 056 319, 2010. DOI: 10.1103/PhysRevE.82.056319.

[52] E. O. Dias and J. A. Miranda, "Taper-induced control of viscous fingering in variable-gap Hele-Shaw flows," *Phys. Rev. E*, vol. 87, p. 053 015, 2013. DOI: 10.1103/PhysRevE.87.053015.

[53] T. T. Al-Housseiny, P. A. Tsai, and H. A. Stone, "Control of interfacial instabilities using flow geometry," *Nat. Phys.*, vol. 8, pp. 747–750, 2012. DOI: 10.1038/nphys2396.

[54] T. T. Al-Housseiny and H. A. Stone, "Controlling viscous fingering in tapered Hele-Shaw cells," *Phys. Fluids*, vol. 25, p. 092 102, Sep. 2013. DOI: 10.1063/1.4819317.

[55] S. J. Jackson, H. Power, D. Giddings, and D. Stevens, "The stability of immiscible viscous fingering in Hele-Shaw cells with spatially varying permeability," *Comput. Meth. Appl. Mech. Engng*, vol. 320, pp. 606–632, 2017. DOI: 10.1016/j.cma.2017.03.030.

[56] J. C. Grenfell-Shaw and A. W. Woods, "The instability of a moving interface in a narrow tapering channel of finite length," *J. Fluid Mech.*, vol. 831, pp. 252–270, 2017. DOI: 10.1017/jfm.2017.633.

[57] L. Díaz-Piola, R. Planet, O. Campàs, J. Casademunt, and J. Ortín, "Fluid front morphologies in gap-modulated Hele-Shaw cells," *Phys. Rev. Fluids*, vol. 2, p. 094 006, 2017. DOI: 10.1103/PhysRevFluids.2.094006.

[58] D. Pihler-Puzović, G. G. Peng, J. R. Lister, M. Heil, and A. Juel, "Viscous fingering in a radial elastic-walled Hele-Shaw cell," *J. Fluid Mech.*, vol. 849, pp. 163–191, 2018. DOI: 10.1017/jfm.2018.404.

[59] G. Bongrand and P. A. Tsai, "Manipulation of viscous fingering in a radially tapered cell geometry," *Phys. Rev. E*, vol. 97, p. 061 101, 2018. DOI: 10.1103/PhysRevE.97.061101.

[60] E. O. Dias and J. A. Miranda, "Control of radial fingering patterns: A weakly nonlinear approach," *Phys. Rev. E*, vol. 81, p. 016 312, 2010. DOI: 10.1103/PhysRevE.81.016312.

[61] E. O. Dias, F. Parisio, and J. A. Miranda, "Suppression of viscous fluid fingering: A piecewise-constant injection process," *Phys. Rev. E*, vol. 82, p. 067 301, 2010. DOI: 10.1103/PhysRevE.82.067301.

[62] E. O. Dias, E. Alvarez-Lacalle, M. S. Carvalho, and J. A. Miranda, "Minimization of viscous fluid fingering: A variational scheme for optimal flow rates," *Phys. Rev. Lett.*, vol. 109, p. 144 502, 2012. DOI: 10.1103/PhysRevLett.109.144502.

[63] H. S. Rabbani, D. Or, Y. Liu, *et al.*, "Suppressing viscous fingering in structured porous media," *Proc. Natl Acad. Sci. USA*, vol. 115, pp. 4833–4838, 2018. DOI: 10.1073/pnas.1800729115.

[64] R. Brandão, E. O. Dias, and J. A. Miranda, "Immiscible three-dimensional fingering in porous media: A weakly nonlinear analysis," *Phys. Rev. Fluids*, vol. 3, p. 034 002, 2018. DOI: 10.1103/PhysRevFluids.3.034002.

[65] L. Carrillo, F. X. Magdaleno, J. Casademunt, and J. Ortín, "Experiments in a rotating Hele-Shaw cell," *Phys. Rev. E*, vol. 54, pp. 6260–6267, 1996. DOI: 10.1103/PhysRevE.54.6260.

[66] E. Alvarez-Lacalle, J. Ortín, and J. Casademunt, "Low viscosity contrast fingering in a rotating Hele-Shaw cell," *Phys. Fluids*, vol. 16, pp. 908–924, 2004. DOI: 10.1063/1.1644149.

[67] J. A. Miranda and E. Alvarez-Lacalle, "Viscosity contrast effects on fingering formation in rotating Hele-Shaw flows," *Phys. Rev. E*, vol. 72, p. 026 306, 2005. DOI: 10.1103/PhysRevE.72.026306.

[68] E. Alvarez-Lacalle, E. Pauné, J. Casademunt, and J. Ortín, "Systematic weakly nonlinear analysis of radial viscous fingering," *Phys. Rev. E*, vol. 68, p. 026 308, 2003. DOI: 10.1103/PhysRevE.68.026308.

[69] P. H. A. Anjos, S. A. Lira, and J. A. Miranda, "Fingering patterns in magnetic fluids: Perturbative solutions and the stability of exact stationary shapes," *Phys. Rev. Fluids*, vol. 3, p. 044 002, 2018. DOI: 10.1103/PhysRevFluids.3.044002.

[70] D. H. Vlad and J. V. Maher, "Tip-splitting instabilities in the channel Saffman-Taylor flow of constant viscosity elastic fluids," *Phys. Rev. E*, vol. 61, pp. 5439–5444, 2000. DOI: 10.1103/PhysRevE.61.5439.

[71] A. Lindner, D. Bonn, E. C. Poiré, M. Ben Amar, and J. Meunier, "Viscous fingering in non-Newtonian fluids," *J. Fluid Mech.*, vol. 469, pp. 237–256, 2002. DOI: 10.1017/S0022112002001714.

[72] P. Tordjeman, "Saffman-Taylor instability of shear thinning fluids," *Phys. Fluids*, vol. 19, pp. 2005–2009, 2007. DOI: 10.1063/1.2795213.

[73] F. Xu, J. Kim, and S. Lee, "Particle-induced viscous fingering," *J. Non-Newtonian Fluid Mech.*, vol. 238, pp. 92–99, 2016. DOI: 10.1016/j.jnnfm.2016.06.014.

[74] J. Kim, F. Xu, and S. Lee, "Formation and destabilization of the particle band on the fluid-fluid interface," *Phys. Rev. Lett.*, vol. 118, p. 074 501, 2017. DOI: 10.1103/PhysRevLett.118.074501.

[75] Y. Chen, F. Malambri, and S. Lee, "Viscous fingering of a draining suspension," *Phys. Rev. Fluids*, vol. 3, p. 094 001, 2018. DOI: 10.1103/PhysRevFluids.3.094001.

[76] D. Pihler-Puzović, P. Illien, M. Heil, and A. Juel, "Suppression of complex fingerlike patterns at the interface between air and a viscous fluid by elastic membranes," *Phys. Rev. Lett.*, vol. 108, p. 074 502, 2012. DOI: 10.1103/PhysRevLett.108.074502.

[77] T. T. Al-Housseiny, I. C. Christov, and H. A. Stone, "Two-phase fluid displacement and interfacial instabilities under elastic membranes," *Phys. Rev. Lett.*, vol. 111, p. 034 502, 2013. DOI: 10.1103/PhysRevLett.111.034502.

[78] D. Pihler-Puzović, A. Juel, and M. Heil, "The interaction between viscous fingering and wrinkling in elastic-walled Hele-Shaw cells," *Phys. Fluids*, vol. 26, p. 022 102, 2014. DOI: 10.1063/1.4864188.

[79] J. V. Fontana, H. Gadêlha, and J. A. Miranda, "Development of tip-splitting and side-branching patterns in elastic fingering," *Phys. Rev. E*, vol. 93, p. 033 126, 2016. DOI: 10.1103/PhysRevE.93.033126.

[80] S. W. McCue, "Short, flat-tipped, viscous fingers: Novel interfacial patterns in a Hele-Shaw channel with an elastic boundary," *J. Fluid Mech.*, vol. 834, pp. 1–4, 2018. DOI: 10.1017/jfm.2017.692.

[81] Z. Zheng, H. Kim, and H. A. Stone, "Controlling viscous fingering using time-dependent strategies," *Phys. Rev. Lett.*, vol. 115, p. 174 501, 2015. DOI: 10.1103/PhysRevLett.115.174501.

[82] B. Dong, Y. Y. Yan, and W. Z. Li, "LBM simulation of viscous fingering phenomenon in immiscible displacement of two fluids in porous media," *Transp. Porous Med.*, vol. 88, pp. 293–314, 2011. DOI: 10.1007/s11242-011-9740-y.

[83] R. P. Nordgren, "Propagation of a vertical hydraulic fracture," *Soc. Petrol Eng. J.*, vol. 12, pp. 306–314, 1972. DOI: 10.2118/3009-PA.

[84] M. M. Rahman and M. K. Rahman, "A review of hydraulic fracture models and development of an improved pseudo-3D model for stimulating tight oil/gas sand," *Energy Sources Part A-Recovery Util. Environ. Eff.*, vol. 32, pp. 1416–1436, 2010. DOI: 10.1080/15567030903060523.

[85] D. Garagash and E. Detournay, "The tip region of a fluid-driven fracture in an elastic medium," *ASME J. Appl. Mech.*, vol. 67, pp. 183–192, 1999. DOI: 10.1115/1.321162.

[86] R. W. Zimmerman and G. S. Bodvarsson, "Hydraulic conductivity of rock fractures," *Transp. Porous Med.*, vol. 23, pp. 1–30, 1996. DOI: 10.1007/BF00145263.

[87] J. Bear, *Dynamics of Fluids in Porous Media*, ser. Environmental Science. New York, NY: American Elsevier Publishing Company, Inc., 1972.

[88] P. A. Witherspoon, J. S. Y. Wang, K. Iwai, and J. E. Gale, "Validity of Cubic Law for fluid flow in a deformable rock fracture," *Water Res. Res.*, vol. 16, pp. 1016–1024, 1980. DOI: 10.1029/WR016i006p01016.

[89] S. R. Brown, "Fluid flow through rock joints: The effect of surface roughness," *J. Geophys. Res.*, vol. 92, no. B2, pp. 1337–1347, 1987. DOI: 10.1029/JB092iB02p01337.

[90] O. Iliev, A. Mikelić, and P. Popov, "On upscaling certain flows in deformable porous media," *Multiscale Model. Simul.*, vol. 7, pp. 93–123, 2008. DOI: 10.1137/06067732X.

[91] Y. Jin, J. Dong, X. Zhang, X. Li, and Y. Wu, "Scale and size effects on fluid flow through self-affine rough fractures," *Int. J. Heat Mass Transfer*, vol. 105, pp. 443–451, 2017. DOI: 10.1016/j.ijheatmasstransfer.2016.10.010.

[92] Z. Wang, C. Xu, and P. Dowd, "Perturbation solutions for flow in a slowly varying fracture and the estimation of its transmissivity," *Transp. Porous Med.*, vol. 128, pp. 97–121, 2019. DOI: 10.1007/s11242-019-01237-7.

[93] M. E. Rosti, S. Pramanik, L. Brandt, and D. Mitra, "The breakdown of Darcy's law in a soft porous material," *Soft Matter*, vol. 16, pp. 939–944, 2020. DOI: 10.1039/C9SM01678C.

[94] B. Berkowitz, "Boundary conditions along permeable fracture walls: Influence on flow and conductivity," *Water Res. Res.*, vol. 25, pp. 1919–1922, 1989. DOI: 10.1029/WR025i008p01919.

[95] T. W. Patzek, F. Male, and M. Marder, "Gas production in the Barnett Shale obeys a simple scaling theory," *Proc. Natl Acad. Sci. USA*, vol. 110, pp. 19 731–19 736, 2013. DOI: 10.1073/pnas.1313380110.

[96] S. Karra, N. Makedonska, H. S. Viswanathan, S. L. Painter, and J. D. Hyman, "Effect of advective flow in fractures and matrix diffusion on natural gas production," *Water Res. Res.*, vol. 51, pp. 8646–8657, 2015. DOI: 10.1002/2014WR016829.

[97] A. S. Berman, "Laminar flow in channels with porous walls," *J. Appl. Phys.*, vol. 24, pp. 1232–1235, 1953. DOI: 10.1063/1.1721476.

[98] J. R. Sellars, "Laminar flow in channels with porous walls at high suction Reynolds numbers," *J. Appl. Phys.*, vol. 26, pp. 489–490, 1955. DOI: 10.1063/1.1722024.

[99] R. M. Terrill and G. M. Shrestha, "Laminar flow through parallel and uniformly porous walls of different permeability," *Z. Angew. Math. Phys. (ZAMP)*, vol. 16, pp. 470–482, 1964. DOI: 10.1007/BF01593923.

[100] J. F. Brady, "Flow development in a porous channel and tube," *Phys. Fluids*, vol. 27, p. 1061, 1984. DOI: 10.1063/1.864735.

[101] J. R. King and S. M. Cox, "Asymptotic analysis of the steady-state and time-dependent Berman problem," *J. Eng. Math.*, vol. 39, pp. 87–130, 2001. DOI: 10.1023/A:1004824527547.

[102] J. B. Grotberg, "Volume-cycled oscillatory flow in a tapered channel," *J. Fluid Mech.*, vol. 141, pp. 249–264, 1984. DOI: 10.1017/S0022112084000823.

[103] A. Kumar, S. Datta, and D. Kalyanasundaram, "Permeability and effective slip in confined flows transverse to wall slippage patterns," *Phys. Fluids*, vol. 28, p. 082 002, 2016. DOI: 10.1063/1.4959184.

[104] A. T. Conlisk, *Essentials of Micro- and Nanofluidics with Applications to the Biological and Chemical Sciences*. New York, NY: Cambridge University Press, 2012.

[105] G. S. Beavers and D. D. Joseph, "Boundary conditions at a naturally permeable wall," *J. Fluid Mech.*, vol. 30, pp. 197–207, 1967. DOI: 10.1017/S0022112067001375.

[106] G. I. Taylor, "A model for the boundary condition of a porous material. Part 1," *J. Fluid Mech.*, vol. 49, pp. 319–326, 1971. DOI: 10.1017/S0022112071002088.

[107] P. G. Saffman, "On the boundary condition at the surface of a porous medium," *Stud. Appl. Math.*, vol. 50, pp. 93–101, 1971. DOI: 10.1002/sapm197150293.

[108] G. S. Beavers, E. M. Sparrow, and R. A. Magnuson, "Experiments on coupled parallel flows in a channel and a bounding porous medium," *ASME J. Basic Eng.*, vol. 92, pp. 843–848, 1970. DOI: 10.1115/1.3425155.

[109] Q. Zhang and A. Prosperetti, "Pressure-driven flow in a two-dimensional channel with porous walls," *J. Fluid Mech.*, vol. 631, pp. 1–21, 2009. DOI: 10.1017/S0022112009005837.

[110] D. A. Nield and A. Bejan, "Mechanics of Fluid Flow Through a Porous Medium," in *Convection in Porous Media*, 4th ed., New York, NY: Springer Science+Business Media, 2013, ch. 1, pp. 1–29. DOI: 10.1007/978-1-4614-5541-7{_}1.

[111] A. Bottaro, "Flow over natural or engineered surfaces: an adjoint homogenization perspective," *J. Fluid Mech.*, vol. 877, P1, 2019. DOI: 10.1017/jfm.2019.607.

[112] R. Mohais, C. Xu, and P. Dowd, "Fluid flow and heat transfer within a single horizontal fracture in an enhanced geothermal system," *ASME J. Heat Transfer*, vol. 133, p. 112 603, 2011. DOI: 10.1115/1.4004369.

[113] G. D'Avino, F. Greco, and P. L. Maffettone, "Particle migration due to viscoelasticity of the suspending liquid and its relevance in microfluidic devices," *Annu. Rev. Fluid Mech.*, vol. 49, pp. 341–360, 2017. DOI: 10.1146/annurev-fluid-010816-060150.

[114] R. Fåhraeus, "The suspension stability of the blood," *Physiol. Rev.*, vol. 9, no. 3, pp. 399–431, 1929. DOI: 10.1152/physrev.1929.9.2.241.

[115] A. Karnis and S. G. Mason, "The flow of suspensions through tubes VI. Meniscus effects," *J. Colloid Interface Sci.*, vol. 23, pp. 120–133, 1967. DOI: 10.1016/0021-9797(67)90093-8.

[116] P. Vasseur and R. G. Cox, "The lateral migration of a spherical particle in a two-dimensional shear flows," *J. Fluid Mechanics*, vol. 78, pp. 385–413, 1976. DOI: 10.1017/S0022112076002498.

[117] J. R. Abbott, N. Tetlow, A. L. Graham, *et al.*, "Experimental observations of particle migration in concentrated suspensions: Couette flow," *J. Rheol.*, vol. 35, pp. 773–795, 1991. DOI: 10.1122/1.550157.

[118] R. J. Phillips, R. C. Armstrong, R. A. Brown, A. L. Graham, and J. R. Abbott, "A constitutive equation for concentrated suspensions that accounts for shear-induced particle migration," *Phys. Fluids A*, vol. 4, pp. 30–40, 1992. DOI: 10.1063/1.858498.

[119] M. A. Tehrani, "An experimental study of particle migration in pipe flow of viscoelastic fluids," *J. Rheol.*, vol. 40, pp. 1057–1077, 1996. DOI: 10.1122/1.550773.

[120] J. F. Morris and J. F. Brady, "Pressure-driven flow of a suspension: Buoyancy effects," *Int. J. Multiphase Flow*, vol. 24, pp. 105–130, 1998. DOI: 10.1016/S0301-9322(97)00035-9.

[121] Y. Ding and D. Wen, "Particle migration in a flow of nanoparticle suspensions," *Powder Technol.*, vol. 149, pp. 84–92, 2005. DOI: 10.1016/j.powtec.2004.11.012.

[122] D. Semwogerere, J. F. Morris, and E. R. Weeks, "Development of particle migration in pressure-driven flow of a Brownian suspension," *J. Fluid Mech.*, vol. 581, pp. 437–451, 2007. DOI: 10.1017/S0022112007006088.

[123] F. Gadala-Maria and A. Acrivos, "Shear-induced structure in a concentrated suspension of solid spheres," *J. Rheol.*, vol. 24, pp. 799–814, 1980. DOI: 10.1122/1.549584.

[124] D. Leighton and A. Acrivos, "The shear-induced migration of particles in concentrated suspensions," *J. Fluid Mech.*, vol. 181, pp. 415–439, 1987. DOI: 10.1017/S0022112087002155.

[125] A. Ramachandran and D. Leighton, "The effect of gravity on the meniscus accumulation phenomenon in a tube," *J. Rheol.*, vol. 51, pp. 1073–1098, 2007. DOI: 10.1122/1.2754309.

[126] P. R. Nott and J. F. Brady, "Pressure-driven flow of suspensions: simulation and theory," *J. Fluid Mech.*, vol. 275, pp. 157–199, 1994. DOI: 10.1017/S0022112094002326.

[127] P. R. Nott, E. Guazzelli, and O. Pouliquen, "The suspension balance model revisited," *Phys. Fluids*, vol. 23, p. 043 304, 2011. DOI: 10.1063/1.3570921.

[128] I. Kwon, H. W. Jung, J. C. Hyun, M.-S. Chun, and B. Chun, "Particle migration in planar Couette–Poiseuille flows of concentrated suspensions," *J. Rheol.*, vol. 62, pp. 419–435, 2018. DOI: 10.1122/1.4989416.

[129] M. Maxey, "Simulation methods for particulate flows and concentrated suspensions," *Annu. Rev. Fluid Mech.*, vol. 49, pp. 171–193, 2017. DOI: 10.1146/annurev-fluid-122414-034408.

[130] S. Shiozawa and M. McClure, "Simulation of proppant transport with gravitational settling and fracture closure in a three-dimensional hydraulic fracturing simulator," *J. Pet. Sci. Eng.*, vol. 138, pp. 298–314, 2016. DOI: 10.1016/j.petrol.2016.01.002.

[131] E. V. Dontsov and A. P. Peirce, "Slurry flow, gravitational settling and a proppant transport model for hydraulic fractures," *J. Fluid Mech.*, vol. 760, pp. 567–590, 2014. DOI: 10.1017/jfm.2014.606.

[132] E. V. Dontsov and A. P. Peirce, "Proppant transport in hydraulic fracturing: Crack tip screen-out in KGD and P3D models," *Int. J. Solids Structs*, vol. 63, pp. 206–218, 2015. DOI: 10.1016/j.ijsolstr.2015.02.051.

[133] F. Boyer, O. Pouliquen, and É. Guazzelli, "Dense suspensions in rotating-rod flows: Normal stresses and particle migration," *J. Fluid Mech.*, vol. 686, pp. 5–25, 2011. DOI: 10.1017/jfm.2011.272.

[134] K. Yeo and M. Maxey, "Numerical simulations of concentrated suspensions of monodisperse particles in a Poiseuille flow," *J. Fluid Mech.*, vol. 682, pp. 491–518, 2011. DOI: 10.1017/jfm.2011.241.

[135] S. Lomholt and M. R. Maxey, "Force-coupling method for particulate two-phase flow: Stokes flow," *J. Comput. Phys.*, vol. 184, pp. 381–405, 2003. DOI: 10.1016/S0021-9991(02)00021-9.

[136] S. Manoorkar, S. Krishnan, O. Sedes, E. S. G. Shaqfeh, G. Iaccarino, and J. F. Morris, "Suspension flow through an asymmetric T-junction," *J. Fluid Mech.*, vol. 844, pp. 247–273, 2018. DOI: 10.1017/jfm.2018.183.

[137] J. F. Morris, "Toward a fluid mechanics of suspensions," *Phys. Rev. Fluids*, vol. 5, p. 110 519, 2020. DOI: 10.1103/PhysRevFluids.5.110519.

[138] P. Mills and P. Snabre, "Rheology and structure of concentrated suspensions of hard spheres. Shear induced particle migration," *J. Physique II*, vol. 5, pp. 1597–1608, 1995. DOI: 10.1051/jp2:1995201.

[139] H. M. Vollebregt, R. G. M. Van Der Sman, and R. M. Boom, "Suspension flow modelling in particle migration and microfiltration," *Soft Matter*, vol. 6, pp. 6052–6064, 2010. DOI: 10.1039/c0sm00217h.

[140] J. F. Morris and F. Boulay, "Curvilinear flows of noncolloidal suspensions: The role of normal stresses," *J. Rheol.*, vol. 43, pp. 1213–1237, 1999. DOI: 10.1122/1.551021.

[141] R. M. Miller and J. F. Morris, "Normal stress-driven migration and axial development in pressure-driven flow of concentrated suspensions," *J. Non-Newtonian Fluid Mech.*, vol. 135, pp. 149–165, 2006. DOI: 10.1016/J.JNNFM.2005.11.009.

[142] D. Lhuillier, "Migration of rigid particles in non-Brownian viscous suspensions," *Phys. Fluids*, vol. 21, p. 023 302, 2009. DOI: 10.1063/1.3079672.

[143] F. Municchi, P. P. Nagrani, and I. C. Christov, "A two-fluid model for numerical simulation of shear-dominated suspension flows," *Int. J. Multiphase Flow*, vol. 120, p. 103 079, 2019. DOI: 10.1016/j.ijmultiphaseflow.2019.07.015.

[144] C. Kang and P. Mirbod, "Shear-induced particle migration of semi-dilute and concentrated Brownian suspensions in both Poiseuille and circular Couette flow," *Int. J. Multiphase Flow*, vol. 126, p. 103 239, 2020. DOI: 10.1016/j.ijmultiphaseflow.2020.103239.

[145] S. Fataei, E. Secrieru, and V. Mechtcherine, "Experimental Insights into Concrete Flow-Regimes Subject to Shear-Induced Particle Migration (SIPM) during Pumping," *Materials*, vol. 13, p. 1233, 2020. DOI: 10.3390/ma13051233.

[146] R. Hernández, "Dynamics of concentrated suspensions in two-dimensional channel flow for non-Newtonian slurries," *Int. J. Multiphase Flow*, p. 103 616, 2021. DOI: 10.1016/j.ijmultiphaseflow.2021.103616.

[147] I. Drijer, T. van de Laar, H. M. Vollebregt, and C. Schroën, "From highly specialised to generally available modelling of shear induced particle migration for flow segregation based separation technology," *Sep. Purif. Technol.*, vol. 192, pp. 99–109, 2018. DOI: 10.1016/j.seppur.2017.10.001.

[148] M. Raissi, P. Perdikaris, and G. Karniadakis, "Physics-informed neural networks: A deep learning framework for solving forward and inverse problems involving nonlinear partial differential equations," *J. Comput. Phys.*, vol. 378, pp. 686–707, 2019. DOI: 10.1016/j.jcp.2018.10.045.

[149] D. Lu, F. Municchi, and I. C. Christov, "Computational Analysis of Interfacial Dynamics in Angled Hele-Shaw Cells: Instability Regimes," *Transp. Porous Med.*, vol. 131, pp. 907–934, 2020. DOI: 10.1007/s11242-019-01371-2.

[150] J. A. Miranda and M. Widom, "Weakly nonlinear investigation of the Saffman-Taylor problem in a rectangular Hele-Shaw cell," *Int. J. Mod. Phys. B*, vol. 12, pp. 931–949, 1998. DOI: 10.1142/S0217979298000521.

[151] H. Zhao and J. V. Maher, "Viscous-fingering experiments with periodic boundary conditions," *Phys. Rev. A*, vol. 42, pp. 5894–5897, 1990. DOI: 10.1103/PhysRevA.42.5894.

[152] C.-W. Park and G. M. Homsy, "Two-phase displacement in Hele Shaw cells: theory," *J. Fluid Mech.*, vol. 139, pp. 291–308, 1984. DOI: 10.1017/S0022112084000367.

[153] K. V. McCloud and J. V. Maher, "Experimental perturbations to Saffman–Taylor flow," *Phys. Rep.*, vol. 260, pp. 139–185, Sep. 1995. DOI: 10.1016/0370-1573(95)91133-U.

[154] H.-W. Lu, K. Glasner, A. L. Bertozzi, and C.-J. Kim, "A diffuse-interface model for electrowetting drops in a Hele-Shaw cell," *J. Fluid Mech.*, vol. 590, pp. 411–435, 2007. DOI: 10.1017/S0022112007008154.

[155] E. Knobloch and R. Krechetnikov, "Problems on time-varying domains: Formulation, dynamics, and challenges," *Acta Appl. Math.*, vol. 137, pp. 123–157, 2015. DOI: 10.1007/s10440-014-9993-x.

[156] D. Pihler-Puzović, R. Périllat, M. Russell, A. Juel, and M. Heil, "Modelling the suppression of viscous fingering in elastic-walled Hele-Shaw cells," *J. Fluid Mech.*, vol. 731, pp. 162–183, 2013. DOI: 10.1017/jfm.2013.375.

[157] S. M. Damián, "Description and utilization of interFoam multiphase solver," International Center for Computational Methods in Engineering, Tech. Rep., 2009, pp. 1–64. [Online]. Available: http://infofich.unl.edu.ar/upload/3be0e16065026527477b4b948c4caa7523c8ea52.pdf.

[158] S. S. Deshpande, L. Anumolu, and M. F. Trujillo, "Evaluating the performance of the two-phase flow solver interFoam," *Comput. Sci. Disc.*, vol. 5, p. 014 016, 2012. DOI: 10.1088/1749-4699/5/1/014016.

[159] H. G. Weller, G. Tabor, C. Fureby, and H. Jasak, "A tensorial approach to computational continuum mechanics using object-oriented techniques," *Comput. Phys.*, vol. 12, pp. 620–631, 1998. DOI: 10.1063/1.168744.

[160] F. Moukalled, L. Mangani, and M. Darwish, *The Finite Volume Method in Computational Fluid Dynamics: An Advanced Introduction with OpenFOAM® and Matlab*, ser. Fluid Mechanics and its Applications. Cham, Switzerland: Springer International Publishing, 2016. DOI: 10.1007/978-3-319-16874-6.

[161] J. U. Brackbill, D. B. Kothe, and C. Zemach, "A continuum method for modeling surface tension," *J. Comput. Phys.*, vol. 100, pp. 335–354, 1992. DOI: 10.1016/0021-9991(92)90240-Y.

[162] S. Popinet, "Numerical models of surface tension," *Annu. Rev. Fluid Mech.*, vol. 50, pp. 49–75, 2018. DOI: 10.1146/annurev-fluid-122316-045034.

[163] C. W. Hirt and B. D. Nichols, "Volume of fluid (VOF) method for the dynamics of free boundaries," *J. Comput. Phys.*, vol. 39, pp. 201–225, 1981. DOI: 10.1016/0021-9991(81)90145-5.

[164] R. I. Issa, "Solution of the implicitly discretised fluid flow equations by operator-splitting," *J. Comput. Phys.*, vol. 62, pp. 40–65, 1986. DOI: 10.1016/0021-9991(86)90099-9.

[165] J. H. Ferziger and M. Perić, "Solution of the Navier-Stokes Equations," in *Computational Methods for Fluid Dynamics*, Berlin/Heidelberg: Springer, 2002, ch. 7, pp. 157–216. DOI: 10.1007/978-3-642-56026-2{_}7.

[166] S. V. Patankar and D. B. Spalding, "A calculation procedure for heat, mass and momentum transfer in three-dimensional parabolic flows," *Int. J. Heat Mass Transfer*, vol. 15, pp. 1787–1806, 1972. DOI: 10.1016/0017-9310(72)90054-3.

[167] J. Hu, B. Wang, and D. Sun, "Numerical investigation of viscous fingering in Hele-Shaw cell with spatially periodic variation of depth," *Appl. Math. Mech.-Engl. Ed.*, vol. 37, pp. 45–58, 2016. DOI: 10.1007/s10483-016-2017-9.

[168] P. Virtanen, R. Gommers, T. E. Oliphant, *et al.*, "SciPy 1.0: fundamental algorithms for scientific computing in Python," *Nat. Methods*, vol. 17, pp. 261–272, 2020. DOI: 10.1038/s41592-019-0686-2.

[169] L. C. Morrow, T. J. Moroney, and S. W. McCue, "Numerical investigation of controlling interfacial instabilities in non-standard Hele-Shaw configurations," *J. Fluid Mech.*, vol. 877, pp. 1063–1097, 2019. DOI: 10.1017/jfm.2019.623.

[170] P. H. A. Anjos, E. O. Dias, and J. A. Miranda, "Fingering instability transition in radially tapered Hele-Shaw cells: Insights at the onset of nonlinear effects," *Phys. Rev. Fluids*, vol. 3, p. 124 004, 2018. DOI: 10.1103/PhysRevFluids.3.124004.

[171] A. A. Osiptsov, S. A. Boronin, E. M. Zilonova, and J. Desroches, "Managed Saffman-Taylor instability during overflush in hydraulic fracturing," *J. Petrol. Sci. Eng.*, vol. 162, pp. 513–523, 2018. DOI: 10.1016/j.petrol.2017.10.018.

[172] M. Wang, Y. Xiong, L. Liu, G. Peng, and Z. Zhang, "Lattice Boltzmann simulation of immiscible displacement in porous media: Viscous fingering in a shear-thinning fluid," *Transp. Porous Med.*, vol. 126, pp. 411–429, 2019. DOI: 10.1007/s11242-018-1162-7.

[173] S. A. Boronin, A. A. Osiptsov, and J. Desroches, "Displacement of yield-stress fluids in a fracture," *Int. J. Multiphase Flow*, vol. 76, pp. 47–63, 2015. DOI: 10.1016/j.ijmultiphaseflow.2015.07.001.

[174] S. Malhotra and M. M. Sharma, "Impact of fluid elasticity on miscible viscous fingering," *Chem. Eng. Sci.*, vol. 117, pp. 125–135, 2014. DOI: 10.1016/j.ces.2014.06.023.

[175] J. R. A. Pearson, "The instability of uniform viscous flow under rollers and spreaders," *J. Fluid Mech.*, vol. 7, pp. 481–500, 1960. DOI: 10.1017/S0022112060000244.

[176] D. Lu, F. Municchi, and I. C. Christov, "The hydraulic conductivity of a shaped fracture with permeable walls," *Mech. Res. Commun.*, vol. 111, p. 103 650, 2021. DOI: 10.1016/j.mechrescom.2020.103650.

[177] M. Van Dyke, "Slow variations in continuum mechanics," *Adv. Appl. Mech.*, vol. 25, pp. 1–45, 1987. DOI: 10.1016/S0065-2156(08)70276-X.

[178] The OpenFOAM Foundation Ltd, *OpenFOAM*, 2021. [Online]. Available: http://www.openfoam.org.

[179] M. J. Nicholl, H. Rajaram, R. J. Glass, and R. Detwiler, "Saturated flow in a single fracture: evaluation of the Reynolds Equation in measured aperture fields," *Water Res. Res.*, vol. 35, pp. 3361–3373, 1999. DOI: 10.1029/1999WR900241.

[180] W. J. Layton, F. Schieweck, and I. Yotov, "Coupling fluid flow with porous media flow," *SIAM J. Numer. Anal.*, vol. 40, pp. 2195–2218, 2002. DOI: 10.1137/S0036142901392766.

[181] W. Jäger and A. Mikelić, "On the interface boundary condition of Beavers, Joseph, and Saffman," *SIAM J. Applied Mathematics*, vol. 60, pp. 1111–1127, 2000. DOI: 10.1137/S003613999833678X.

[182] M. H. Holmes, *Introduction to Perturbation Methods*, 2nd ed., ser. Texts in Applied Mathematics. New York, NY: Springer Science+Business Media, 2013, vol. 20. DOI: 10.1007/978-1-4614-5477-9.

[183] B. Tavakol, G. Froehlicher, H. A. Stone, and D. P. Holmes, "Extended lubrication theory: Improved estimates of flow in channels with variable geometry," *Proc. R. Soc. A*, vol. 473, p. 20 170 234, 2017. DOI: 10.1098/rspa.2017.0234.

[184] S. Salimzadeh, A. Paluszny, and R. W. Zimmerman, "Three-dimensional poroelastic effects during hydraulic fracturing in permeable rocks," *Int. J. Solids Struct.*, vol. 108, pp. 153–163, 2017. DOI: 10.1016/j.ijsolstr.2016.12.008.

[185] N. Tilton, D. Martinand, E. Serre, and R. M. Lueptow, "Incorporating Darcy's law for pure solvent flow through porous tubes: Asymptotic solution and numerical simulations," *AIChE J.*, vol. 58, pp. 2030–2044, 2012. DOI: 10.1002/aic.13823.

[186] J. G. Herterich, D. Vella, R. W. Field, N. P. Hankins, and I. M. Griffiths, "Tailoring wall permeabilities for enhanced filtration," *Phys. Fluids*, vol. 27, p. 053 102, 2015. DOI: 10.1063/1.4919658.

[187] A. H. Al-Yaarubi, C. C. Pain, C. A. Grattoni, and R. W. Zimmerman, "Navier-Stokes simulations of fluid flow through a rock fracture," in *Dynamics of Fluids and Transport in Fractured Rock*, ser. Geophysical Monograph Series, B. Faybishenko, P. A. Witherspoon, and J. Gale, Eds., vol. 162, Washington, DC: American Geophysical Union, 2013, pp. 55–64. DOI: 10.1029/162GM07.

[188] Z. F. Tian, C. Xu, and P. A. Dowd, "Numerical simulation of flows in a channel with impermeable and permeable walls using finite volume methods," in *Flow and Transport in Subsurface Environment*, ser. Springer Transactions in Civil and Environmental Engineering, N. Narayanan, B. Mohanadhas, and V. Mangottiri, Eds., Singapore: Springer, 2018, pp. 119–140. DOI: 10.1007/978-981-10-8773-8{_}4.

[189] P. J. Roache, *Verification and Validation in Computational Science and Engineering*. Socorro, New Mexico: Hermosa Publishers, 1998.

[190] D. Lu and I. C. Christov, "Physics-informed neural networks for understanding shear migration of particles in viscous flow," *preprint*, arXiv:2111.04684, 2021.

[191] J. J. Stickel and R. L. Powell, "Fluid mechanics and rheology of dense suspensions," *Ann. Rev. Fluid Mech.*, vol. 37, pp. 129–149, 2005. DOI: 10.1146/annurev.fluid.36.050802.122132.

[192] D. Merhi, E. Lemaire, G. Bossis, and F. Moukalled, "Particle migration in a concentrated suspension flowing between rotating parallel plates: Investigation of diffusion flux coefficients," *J. Rheol.*, vol. 49, pp. 1429–1448, 2005. DOI: 10.1122/1.2079247.

[193] J. M. Bricker and J. E. Butler, "Oscillatory shear of suspensions of noncolloidal particles," *J. Rheol.*, vol. 50, pp. 711–728, 2006. DOI: 10.1122/1.2234366.

[194] S. L. Brunton and J. N. Kutz, *Data-Driven Science and Engineering*. Cambridge, UK: Cambridge University Press, 2019. DOI: 10.1017/9781108380690.

[195] S. L. Brunton, B. R. Noack, and P. Koumoutsakos, "Machine Learning for Fluid Mechanics," *Annu. Rev. Fluid Mech.*, vol. 52, pp. 477–508, 2020. DOI: 10.1146/annurev-fluid-010719-060214.

[196] M. P. Brenner, J. D. Eldredge, and J. B. Freund, "Perspective on machine learning for advancing fluid mechanics," *Phys. Rev. Fluids*, vol. 4, p. 100 501, 2019. DOI: 10.1103/PhysRevFluids.4.100501.

[197] G. E. Karniadakis, I. G. Kevrekidis, L. Lu, P. Perdikaris, S. Wang, and L. Yang, "Physics-informed machine learning," *Nat. Rev. Phys.*, vol. 3, pp. 422–440, 2021. DOI: 10.1038/s42254-021-00314-5.

[198] X. I. A. Yang, S. Zafar, J.-X. Wang, and H. Xiao, "Predictive large-eddy-simulation wall modeling via physics-informed neural networks," *Phys. Rev. Fluids*, vol. 4, p. 034 602, 2019. DOI: 10.1103/PhysRevFluids.4.034602.

[199] Z. Mao, A. D. Jagtap, and G. E. Karniadakis, "Physics-informed neural networks for high-speed flows," *Comput. Meth. Appl. Mech. Engng*, vol. 360, p. 112 789, 2020. DOI: 10.1016/j.cma.2019.112789.

[200] Q. He and A. M. Tartakovsky, "Physics-Informed Neural Network Method for Forward and Backward Advection-Dispersion Equations," *Water Res. Res.*, vol. 57, e2020WR029479, 2021. DOI: 10.1029/2020WR029479.

[201] X. Jin, S. Cai, H. Li, and G. E. Karniadakis, "NSFnets (Navier-Stokes flow nets): Physics-informed neural networks for the incompressible Navier-Stokes equations," *J. Comput. Phys.*, vol. 426, p. 109 951, 2021. DOI: 10.1016/j.jcp.2020.109951.

[202] B. Reyes, A. A. Howard, P. Perdikaris, and A. M. Tartakovsky, "Learning unknown physics of non-Newtonian fluids," *Phys. Rev. Fluids*, vol. 6, p. 073 301, 2021. DOI: 10.1103/PhysRevFluids.6.073301.

[203] M. Raissi, A. Yazdani, and G. E. Karniadakis, "Hidden fluid mechanics: Learning velocity and pressure fields from flow visualizations," *Science*, vol. 367, pp. 1026–1030, 2020. DOI: 10.1126/science.aaw4741.

[204] E. Haghighat, M. Raissi, A. Moure, H. Gomez, and R. Juanes, "A physics-informed deep learning framework for inversion and surrogate modeling in solid mechanics," *Comput. Meth. Appl. Mech. Engng*, vol. 379, p. 113 741, 2021. DOI: 10.1016/j.cma.2021.113741.

[205] W. Li, M. Z. Bazant, and J. Zhu, "A physics-guided neural network framework for elastic plates: Comparison of governing equations-based and energy-based approaches," *Comput. Meth. Appl. Mech. Engng*, vol. 383, p. 113 933, 2021. DOI: 10.1016/j.cma.2021.113933.

[206] Y. Chen, L. Lu, G. E. Karniadakis, and L. Dal Negro, "Physics-informed neural networks for inverse problems in nano-optics and metamaterials," *Optics Express*, vol. 28, p. 11 618, 2020. DOI: 10.1364/OE.384875.

[207] S. Cai, Z. Wang, S. Wang, P. Perdikaris, and G. E. Karniadakis, "Physics-Informed Neural Networks for Heat Transfer Problems," *ASME J. Heat Transfer*, vol. 143, p. 060 801, 2021. DOI: 10.1115/1.4050542.

[208] A. G. Baydin, B. A. Pearlmutter, A. A. Radul, and J. M. Siskind, "Automatic Differentiation in Machine Learning: a Survey," *J. Mach. Learning Res.*, vol. 18, pp. 1–43, 2018. [Online]. Available: http://jmlr.org/papers/v18/17-468.html.

[209] X. Meng and G. E. Karniadakis, "A composite neural network that learns from multi-fidelity data: Application to function approximation and inverse PDE problems," *J. Comput. Phys.*, vol. 401, p. 109 020, 2020. DOI: 10.1016/j.jcp.2019.109020.

[210] S. Wang, X. Yu, and P. Perdikaris, "When and why PINNs fail to train: A neural tangent kernel perspective," *J. Comput. Phys.*, p. 110 768, 2021. DOI: 10.1016/j.jcp.2021.110768.

[211] M. Abadi, A. Agarwal, P. Barham, *et al.*, *TensorFlow: Large-Scale Machine Learning on Heterogeneous Systems*, 2015. [Online]. Available: https://www.tensorflow.org/.

[212] D. P. Kingma and J. Ba, "Adam: A Method for Stochastic Optimization," in *3rd International Conference on Learning Representations (ICLR)*, Y. Bengio and Y. LeCun, Eds., San Diego, CA, May 2015. [Online]. Available: http://arxiv.org/abs/1412.6980.

[213] I. M. Krieger and T. J. Dougherty, "A Mechanism for Non-Newtonian Flow in Suspensions of Rigid Spheres," *Trans. Soc. Rheol.*, vol. 3, pp. 137–152, 1959. DOI: 10.1122/1.548848.

[214] I. M. Krieger, "Rheology of monodisperse latices," *Adv. Colloid Interface Sci.*, vol. 3, pp. 111–136, 1972. DOI: 10.1016/0001-8686(72)80001-0.

[215] M. M. Denn and J. F. Morris, "Rheology of non-Brownian suspensions," *Ann. Rev. Chem. Biomolec. Eng.*, vol. 5, pp. 203–228, 2014. DOI: 10.1146/annurev-chembioeng-060713-040221.

[216] C. J. Koh, P. Hookham, and L. G. Leal, "An experimental investigation of concentrated suspension flows in a rectangular channel," *J. Fluid Mech.*, vol. 266, pp. 1–32, 1994. DOI: 10.1017/S0022112094000911.

[217] S. C. Jana, B. Kapoor, and A. Acrivos, "Apparent wall slip velocity coefficients in concentrated suspensions of noncolloidal particles," *J. Rheol.*, vol. 39, pp. 1123–1132, 1995. DOI: 10.1122/1.550631.

[218] D. M. Kalyon, "Apparent slip and viscoplasticity of concentrated suspensions," *J. Rheol.*, vol. 49, pp. 621–640, 2005. DOI: 10.1122/1.1879043.

[219] M. Frank, D. Anderson, E. R. Weeks, and J. Morris, "Particle migration in pressure-driven flow of a Brownian suspension," *J. Fluid Mech.*, vol. 493, pp. 363–378, 2003. DOI: 10.1017/S0022112003006001.

[220] C. G. de Kruif, E. M. F. van Iersel, A. Vrij, and W. B. Russel, "Hard sphere colloidal dispersions: Viscosity as a function of shear rate and volume fraction," *J. Chem. Phys.*, vol. 83, pp. 4717–4725, 1985. DOI: 10.1063/1.448997.

[221] A. Alwosheel, S. van Cranenburgh, and C. G. Chorus, "Is your dataset big enough? Sample size requirements when using artificial neural networks for discrete choice analysis," *J. Choice Model.*, vol. 28, pp. 167–182, 2018. DOI: 10.1016/j.jocm.2018.07.002.

[222] H. Tang, W. Grivas, D. Homentcovschi, J. Geer, and T. Singler, "Stability considerations associated with the meniscoid particle band at advancing interfaces in Hele-Shaw suspension flows," *Phys. Rev. Lett.*, vol. 85, pp. 2112–2115, 2000. DOI: 10.1103/PhysRevLett.85.2112.

[223] J. Gostick, M. Aghighi, J. Hinebaugh, *et al.*, "OpenPNM: A pore network modeling package," *Comput. Sci. Eng.*, vol. 18, no. 4, pp. 60–74, 2016. DOI: 10.1109/MCSE.2016.49.

[224] D. T. Birdsell, H. Rajaram, D. Dempsey, and H. S. Viswanathan, "Hydraulic fracturing fluid migration in the subsurface: A review and expanded modeling results," *Water Res. Res.*, vol. 51, pp. 7159–7188, 2015. DOI: 10.1002/2015WR017810.

VITA

Education

Ph.D. in Mechanical Engineering

Purdue University, West Lafayette, Indiana, USA — Dec. 2021

M.S. in Engineering Thermophysics

Xi'an Jiaotong University, Xi'an China — May 2016

B.E. in Oil and Gas Storage and Transportation Engineering

China University of Petroleum, Beijing, China — Jun. 2013

Work Experience

Software Engineer Intern, Amazon, Irvine, California, USA — May 2021 – Jul. 2021

Publications resulting from this thesis

- Daihui Lu, Federico Municchi, and Ivan C. Christov, "The hydraulic conductivity of a shaped fracture with permeable walls," *Mech. Res. Commun.*, vol. 111, 103650, 2021.
- Daihui Lu, Federico Municchi, and Ivan C. Christov, "Computational Analysis of Interfacial Dynamics in Angled Hele-Shaw Cells: Instability Regimes," *Transp. Porous Med.*, vol. 131, pp. 907–934, 2020.

Conference presentations resulting from this thesis

- Daihui Lu and Ivan C. Christov, Physics-Informed Neural Networks for Shear-Induced Particle Migration, IMA Workshop on the Mathematical Foundation and Applications of Deep Learning (virtual), 2021.
- Daihui Lu, Federico Municchi, and Ivan C. Christov, The hydraulic conductivity of shaped fractures with permeable walls, InterPore (virtual), 2020.

- Daihui Lu, Ivan C. Christov, The hydraulic conductivity of shaped fractures with permeable walls, The 72nd Annual Meeting of the APS DFD, Seattle, Washington, USA, 2019.

- Daihui Lu, Federico Municchi, and Ivan C. Christov, Theory and computation of interfacial instabilities in shaped fractures, Midwestern University Fluid Mechanics Retreat, Rochester, Indiana, USA, 2019.

- Daihui Lu, Federico Municchi, and Ivan C. Christov, Computational analysis of interfacial instabilities in Hele-Shaw cells with small gap gradient, The 71st Annual Meeting of the APS DFD, Atlanta, Georgia, USA, 2018.

- Daihui Lu and Ivan C. Christov, Computational Analysis of Interfacial Instabilities in Tapered Hele-Shaw Cells, The 18th U.S. National Congress on Theoretical and Applied Mechanics, Chicago, Illinois, USA, 2018.